

## Development of high-resolution ex vivo single-photon and positron emission tomography

Nguyen, M.P.

**DOI**

[10.4233/uuid:106952cc-6ac9-4c5c-9b2b-e0d07b3bd8df](https://doi.org/10.4233/uuid:106952cc-6ac9-4c5c-9b2b-e0d07b3bd8df)

**Publication date**

2021

**Document Version**

Final published version

**Citation (APA)**

Nguyen, M. P. (2021). *Development of high-resolution ex vivo single-photon and positron emission tomography*. [Dissertation (TU Delft), Delft University of Technology]. <https://doi.org/10.4233/uuid:106952cc-6ac9-4c5c-9b2b-e0d07b3bd8df>

**Important note**

To cite this publication, please use the final published version (if applicable).  
Please check the document version above.

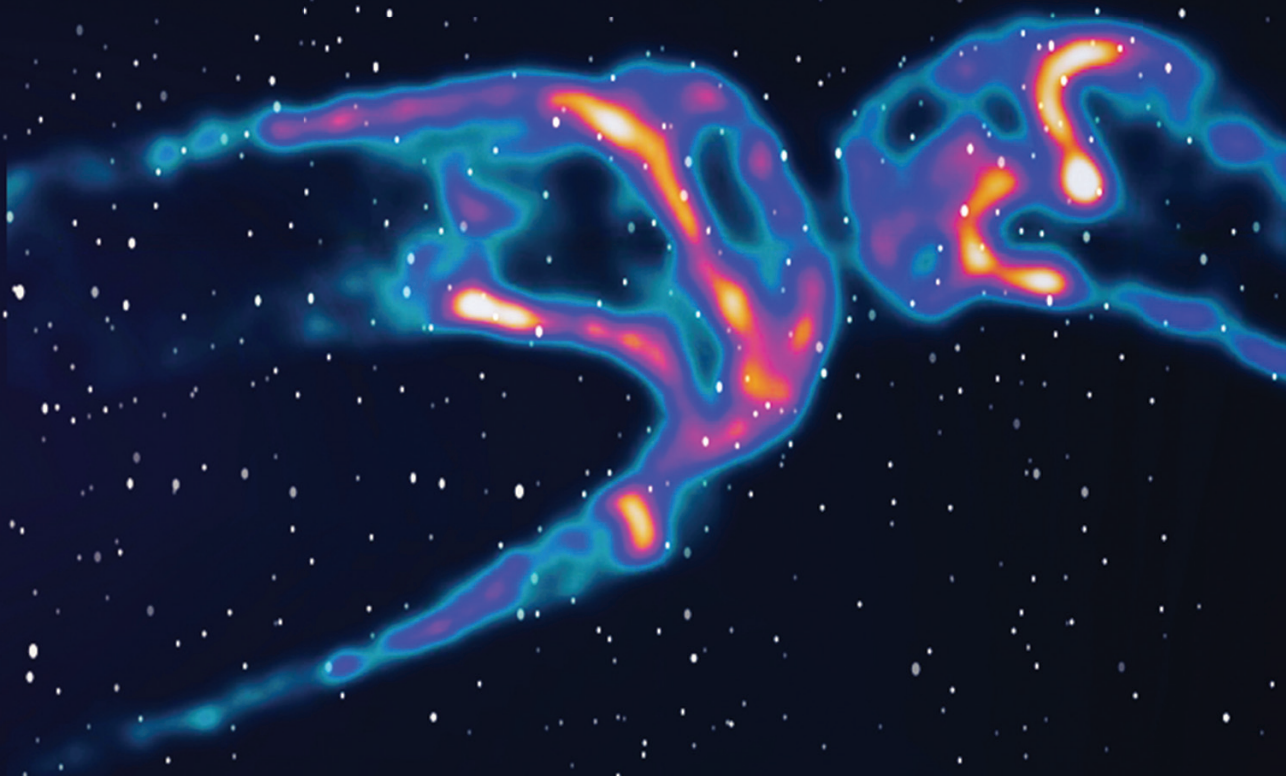
**Copyright**

Other than for strictly personal use, it is not permitted to download, forward or distribute the text or part of it, without the consent of the author(s) and/or copyright holder(s), unless the work is under an open content license such as Creative Commons.

**Takedown policy**

Please contact us and provide details if you believe this document breaches copyrights.  
We will remove access to the work immediately and investigate your claim.

Development of high-resolution  
*ex vivo* single-photon and positron  
emission tomography



Minh Phuong Nguyen



# **Development of high-resolution *ex vivo* single-photon and positron emission tomography**

## **Proefschrift**

ter verkrijging van de graad van doctor  
aan de Technische Universiteit Delft,  
op gezag van de Rector Magnificus Prof. dr. ir. T.H.J.J. van der Hagen,  
voorzitter van het College voor Promoties,  
in het openbaar te verdedigen  
op 23 juni 2021 om 17:30 uur

door

**Minh Phuong NGUYEN**

Master of Science in Electrical Engineering,  
Ulsan National Institute of Science and Technology, Zuid-Korea,  
geboren te Hai Phong, Vietnam.

Dit proefschrift is goedgekeurd door de promotor.

Samenstelling promotiecommissie:

Rector Magnificus	voorzitter
Prof.dr. F.J. Beekman	Technische Universiteit Delft, <i>promotor</i>
Dr.ir. M.C. Goorden	Technische Universiteit Delft, <i>copromotor</i>

*Onafhankelijke leden:*

Dr. J. Nonnekens	Erasmus Medisch Centrum
Prof.dr. F.A. Verburg	Erasmus Medisch Centrum
Prof.dr. S.D. Metzler	University of Pennsylvania, USA
Prof.dr. V. Sossi	The University of British Columbia, Canada
Prof.dr.ir. H.H. Weinans	Technische Universiteit Delft/ Universitair Medisch Centrum Utrecht
Prof.dr. P. Dorenbos	Technische Universiteit Delft, <i>reservelid</i>

The research described in this thesis was performed in the section Biomedical Imaging, of the department of Radiation Science and Technology, at the faculty of Applied Sciences, Delft University of Technology, the Netherlands.



**Keywords:** *ex vivo*, SPECT, PET, pinhole, small animal, molecular imaging, collimator, system matrix, Monte Carlo simulation

**Printed by:** ProefschriftMaken, [www.proefschriftmaken.nl](http://www.proefschriftmaken.nl)

**Cover:** Foreground: image of a mouse knee with  $^{99m}\text{Tc}$ -MDP SPECT  
Background: [www.shutterstock.com](http://www.shutterstock.com), image ID: 1717839370

ISBN: 978-94-6423-317-9

An electronic version of this dissertation is available at  
<http://repository.tudelft.nl/>.

# Contents

<b>Summary</b>	<b>v</b>
<b>Samenvatting</b>	<b>vii</b>
<b>1 General introduction</b>	<b>1</b>
1.1 Nuclear molecular imaging. . . . .	1
1.2 Pinhole collimation. . . . .	3
1.3 Pinhole microSPECT and microPET . . . . .	5
1.4 Pushing resolution with <i>ex vivo</i> imaging . . . . .	6
1.5 Optimising system modelling for image reconstruction. . . . .	7
1.6 Research aims and thesis outline . . . . .	9
<b>2 Evaluation of pinhole collimator materials for micron-resolution <i>ex vivo</i> SPECT</b>	<b>11</b>
2.1 Introduction . . . . .	12
2.2 Methods . . . . .	14
2.2.1 EXIRAD-3D system with multi-pinhole collimator . . . . .	14
2.2.2 Monte Carlo simulations . . . . .	14
2.2.3 Determination of pinhole diameters to obtain equal sensitivities . .	16
2.2.4 PSF comparison for single pinholes. . . . .	17
2.2.5 Multi-pinhole reconstruction. . . . .	17
2.3 Results . . . . .	21
2.3.1 Pinhole diameters to obtain equal sensitivities for different collimator materials . . . . .	21
2.3.2 PSF comparison . . . . .	21
2.3.3 Multi-pinhole reconstruction. . . . .	22
2.4 Discussion . . . . .	24
2.5 Conclusion. . . . .	29
<b>3 EXIRAD-3D: Fast automated three-dimensional autoradiography</b>	<b>31</b>
3.1 Introduction . . . . .	32
3.2 Methods . . . . .	34
3.2.1 System and collimator description . . . . .	34
3.2.2 Image reconstruction and processing. . . . .	34
3.2.3 Experiments . . . . .	35
3.3 Results . . . . .	37
3.3.1 Phantom studies . . . . .	37
3.3.2 Mouse knee joint scan . . . . .	38
3.3.3 Mouse thyroid scan . . . . .	39
3.3.4 Mouse kidney scan. . . . .	40

3.4	Discussion . . . . .	40
3.5	Conclusion . . . . .	42
<b>4</b>	<b>Efficient Monte-Carlo based system modelling for preclinical pinhole SPECT</b>	<b>43</b>
4.1	Introduction . . . . .	44
4.2	Methods . . . . .	46
4.2.1	Studied systems and multi-pinhole collimators . . . . .	46
4.2.2	Monte Carlo simulations . . . . .	46
4.2.3	Monte-Carlo based system modelling . . . . .	47
4.2.4	Studied scans. . . . .	50
4.2.5	Image reconstruction and evaluation . . . . .	53
4.2.6	Comparison with traditional and ray-tracing methods . . . . .	54
4.3	Results . . . . .	56
4.3.1	Validation of accelerated point-source simulation . . . . .	56
4.3.2	Experimental $^{99m}\text{Tc}$ and $^{111}\text{In}$ phantom scans. . . . .	56
4.3.3	Experimental $^{123}\text{I}$ mouse thyroid scan . . . . .	58
4.3.4	Simulated $^{67}\text{Ga}$ scan: combining multiple photopeaks . . . . .	59
4.3.5	Simulated $^{90}\text{Y}$ scan: utilising a wide continuous energy spectrum . . . . .	60
4.4	Discussion . . . . .	60
4.5	Conclusion . . . . .	64
<b>5</b>	<b>EXIRAD-HE: Multi-pinhole high-resolution <i>ex vivo</i> imaging of high-energy isotopes</b>	<b>67</b>
5.1	Introduction . . . . .	68
5.2	Methods . . . . .	69
5.2.1	Considerations in collimator design and optimisation . . . . .	69
5.2.2	Analytical model. . . . .	71
5.2.3	Monte Carlo simulations . . . . .	73
5.2.4	Collimator optimisation and evaluation procedure . . . . .	75
5.2.5	Image reconstruction. . . . .	77
5.3	Results . . . . .	79
5.3.1	Collimator optimisation . . . . .	79
5.3.2	Evaluation with digital Derenzo phantoms . . . . .	81
5.3.3	Evaluation with digital mouse tissue phantoms. . . . .	82
5.4	Discussion . . . . .	83
5.5	Conclusion . . . . .	84
<b>6</b>	<b>Thesis conclusion</b>	<b>87</b>
	<b>Bibliography</b>	<b>91</b>
	<b>Acknowledgments</b>	<b>107</b>
	<b>Curriculum Vitæ</b>	<b>109</b>
	<b>List of Publications</b>	<b>111</b>

# Summary

Molecular imaging aims for the visualisation, characterisation, and quantification of biological processes in humans and other living systems at the molecular and cellular level. For today's patient care, molecular imaging allows for (early) detection and characterisation of disease, efficient planning and assessment of treatments, and contributes to improved patient care in ten-thousand clinics across the globe. In clinical molecular imaging, planar scintigraphy, single-photon emission computed tomography (SPECT), and positron emission tomography (PET) are among the most commonly used modalities. This thesis focuses on preclinical SPECT and PET, which are applied to image small animals such as mice and rats in basic and translational research.

SPECT and PET are both performed by administering a tiny amount of radioactive tracer into the subject and imaging the radioactivity distribution in the target locations. Imaging systems mainly consist of (1) one or more so-called gamma-cameras or a gamma-detection ring which measure gamma photons resulting directly from the radioactivity decay or from positron-electron annihilations, (2) a physical collimator in case of SPECT or collimated PET, or electronic collimation in case of coincidence PET, which both provide information on the direction that detected gamma photons come from, and (3) reconstruction software to obtain an image from the measured data.

The use of multi-pinhole collimation helps to achieve ultra-high-resolution preclinical SPECT and can also be applied to achieve sub-mm resolution preclinical PET with many unique capabilities. Because of the small size of animals, with this type of collimator, the activity distribution can be significantly magnified on the detector. In this way, the image resolution can be many times better than the detector's resolution, which is typically limited in conventional gamma-cameras to about 3.5 mm. *In vivo* resolution depends on the size of the subject (e.g. a mouse) because this is the factor limiting how close pinholes can be positioned relative to the activity distribution in order to achieve a high magnification and good sensitivity. A higher resolution than what can be achieved *in vivo* is still desirable. *Ex vivo* scanning of small tissue samples is a straightforward way to increase the resolution.

This thesis aims to develop and validate new ultra-high-resolution *ex vivo* three-dimensional (3D) imaging modules to use with existing preclinical SPECT and PET systems (in this work developed for the U-SPECT and VECTor, MILabs B.V.) for a wide range of energies, by means of dedicated multi-pinhole collimators and by utilising accurate system modelling for high-resolution image reconstruction. Two modules were developed: EXIRAD-3D for imaging with relatively low and medium energies (27-245 keV), and EXIRAD-HE for imaging with high energies (364-603 keV).

First, the choice of collimator material was studied for EXIRAD-3D via Monte Carlo simulations. While the material assumed was either lead, tungsten, gold, or depleted

uranium, the system sensitivity was fixed by adjusting the pinhole diameter. Then, using full system simulations, we evaluated Derenzo resolution phantom scans obtained with the different collimators to see which material resulted in the optimal image. Results showed that, compared to using lead, using materials with higher stopping power yielded images with better image contrast-to-noise ratio with improvements ranging from 1.9% to 36.6% for the studied isotopes. Visual assessment on the reconstructed images suggested that tungsten is generally a good choice for the EXIRAD-3D collimator for a wide range of SPECT isotopes such as  $^{125}\text{I}$  (27 keV),  $^{201}\text{Tl}$  (71 keV), and  $^{99m}\text{Tc}$  (140 keV). To also enable optimal imaging of isotopes with higher energy gamma photons such as  $^{111}\text{In}$  (171 keV and 245 keV), using pinhole inserts made of gold can be beneficial.

An EXIRAD-3D collimator made of a tungsten alloy was then evaluated with various experimental scans with phantoms and mouse tissues. The phantom scans with  $^{99m}\text{Tc}$  demonstrated a 120  $\mu\text{m}$  spatial image resolution and good image uniformity. Tiny details were visualised in a [ $^{99m}\text{Tc}$ ]MDP mouse knee joint scan, a [ $^{123}\text{I}$ ]NaI mouse thyroid scan, and a [ $^{99m}\text{Tc}$ ]DMSA mouse kidney scan, with a significantly better level of detail than what can be achieved in preclinical *in vivo* SPECT.

Further improvement of EXIRAD-3D in terms of system modelling for image reconstruction was done. A Fast Monte-Carlo based (FMC-based) method was introduced that addressed some challenges with the available system modelling methods used for EXIRAD-3D (traditional method and ray-tracing method). The results showed that FMC is an efficient, accurate, and versatile system modelling tool for EXIRAD-3D and other pinhole SPECT systems when the isotopes have low or medium energies ( $\leq 285$  keV). It is more generalised than the traditional method when changing isotopes or acquisition window settings, and more computationally efficient than the ray-tracing method for ultra-high-resolution systems like EXIRAD-3D. FMC also has the advantage of easily combining energies in a single matrix which saves time in both system modelling and image reconstruction.

Additionally, new collimators for ex-vivo use called EXIRAD-HE were developed and optimised by means of Monte Carlo simulations, for the scanning of high-energy (HE) isotopes such as PET isotopes that result in 511 keV photons, and therapeutic isotopes (alpha and beta emitters such as  $^{131}\text{I}$  (364 keV) or  $^{213}\text{Bi}$  (440 keV)) that co-emit high-energy gammas. Two multi-pinhole collimators were designed for 511 keV at system sensitivities of 0.30% and 0.60%, and these were also tested for other high energies. Simulated spatial resolutions were obtained of 0.35 mm, 0.6 mm, 0.5 mm, 0.6 mm, and 0.5 mm when imaging  $^{131}\text{I}$ ,  $^{213}\text{Bi}$ ,  $^{18}\text{F}$ ,  $^{64}\text{Cu}$ , and  $^{124}\text{I}$ , respectively.

The EXIRAD technique presented in this thesis offers resolutions far better than what can be achieved with *in vivo* preclinical SPECT and PET, while saving tremendous amounts of work compared to obtaining 3D data from a set of 2D autoradiographs. Therefore, this technique can be a very good choice in a subset of pharmaceutical and biological studies, in particular as an option on a U-SPECT/CT or a VECTor/CT imaging system that facilitates longitudinal studies on the same animal as well, and provides a direct link between *in vivo* and *ex vivo* datasets.

# Samenvatting

Moleculaire beeldvorming is gericht op de visualisatie, karakterisatie en kwantificatie van biologische processen in mensen en andere levende systemen op moleculair en cellulair niveau. In de huidige patiëntenzorg wordt moleculaire beeldvorming toegepast voor (vroeg) detectie en karakterisering van ziekten, efficiënte planning en beoordeling van behandelingen, en draagt bij aan verbeterde patiëntenzorg in tienduizenden klinieken over de hele wereld. Bij klinische moleculaire beeldvorming behoren planaire scintigrafie, 'single-photon' emissie tomografie (SPECT) en positron emissie tomografie (PET) tot de meest gebruikte beeldvormingsmodaliteiten. De focus van dit proefschrift ligt op preklinische SPECT en PET, technieken die worden toegepast voor het afbeelden van kleine dieren zoals muizen en ratten in fundamenteel en translationeel onderzoek.

SPECT en PET worden uitgevoerd door een kleine hoeveelheid radioactieve tracer aan het subject toe te dienen en dan de verdeling van de radioactiviteit in het gebied waarin men geïnteresseerd is in beeld te brengen. De hoofdbestanddelen van de scanners zijn (1) één of meer zogenaamde gamma-cameras of een gamma-camera-ring voor detectie van gammafotonen die ofwel het direct produkt zijn van radioactief verval, of van positron-elektron-annihilaties, (2) een fysieke collimator -in het geval van SPECT of gecollimeerde PET- of elektronische collimatie -in het geval van coïncidentie PET-, in beide gevallen om informatie te verkrijgen over de richting waar gedetecteerde fotonen vandaan komen, en (3) reconstructiesoftware om een afbeelding te verkrijgen uit de gemeten data.

Het gebruik van een multi-pinhole collimator helpt om SPECT met ultrahoge resolutie te bereiken en kan ook worden toegepast om PET met een resolutie van minder dan een millimeter te bewerkstelligen met vele unieke mogelijkheden. Vanwege de kleine afmetingen van dieren, kan met dit type collimator de activiteitsverdeling met aanzienlijke vergroting op de detector worden afgebeeld. *In vivo* resolutie is afhankelijk van de grootte van het subject (bijvoorbeeld een muis), omdat dit de factor is die beperkt hoe dicht de pinholes bij de activiteitverdeling geplaatst kunnen worden om een sterke vergroting en goede gevoeligheid te bereiken. Een hogere resolutie dan momenteel *in vivo* kan worden bereikt is nog steeds wenselijk. Het *ex vivo* scannen van kleine weefselmonsters is een voor de hand liggende manier om de resolutie te verhogen.

Dit proefschrift heeft tot doel nieuwe ultrahoge resolutie *ex vivo* 3D-beeldvormingsmodules te ontwikkelen en te valideren voor gebruik in bestaande preklinische SPECT- en PET-systemen (in dit werk ontwikkeld voor de U-SPECT en VECTor, MILabs B.V.) voor een breed bereik van energieën, door middel van speciale multi-pinhole collimatoren en het gebruik van nauwkeurige systeemmodellering voor beeldreconstructie met hoge resolutie. Er werden twee modules ontwikkeld: EXIRAD-3D voor beeldvorming met relatief lage en gemiddelde fotonenergieën (27-245 keV), en EXIRAD-HE voor beeldvorming met hoge fotonenergieën (364-603 keV).

Eerst werd de materiaalkeuze voor de EXIRAD-3D collimator bestudeerd via Monte-Carlo-simulaties. Collimators gemaakt van lood, wolfram, goud of verarmd uranium werden een gelijke systeemgevoeligheid gegeven door de diameter van de pinholes aan

te passen. Voor die verschillende collimatoren hebben we met behulp van complete scannersimulaties Derenzo-resolutie fantoomscans geëvalueerd om te zien welk materiaal resulteerde in het beste beeld. De resultaten toonden aan dat het gebruik van materialen met een hoger verzwakkingsvermogen dan lood de beeldcontrast-ruisverhouding verbeterde van 1.9% tot 36.6% voor de bestudeerde isotopen. Visuele beoordeling van de gereconstrueerde beelden suggereerde dat wolfram over het algemeen een goede keuze is voor de EXIRAD-3D-collimator voor een breed scala aan SPECT-isotopen zoals  $^{125}\text{I}$  (27 keV),  $^{201}\text{Tl}$  (71 keV), en  $^{99m}\text{Tc}$  (140 keV). Voor isotopen met relatief hoge energie, zoals  $^{111}\text{In}$  (171 keV en 245 keV), kan het gebruik van pinhole-inzetstukken van goud gunstig zijn.

Een EXIRAD-3D-collimator gemaakt van een wolframlegering werd geëvalueerd door middel van verschillende experimentele scans met fantomen en muisweefsels. De fantoomscans met  $^{99m}\text{Tc}$  toonden een ruimtelijke beeldresolutie van 120  $\mu\text{m}$  en een goede beelduniformiteit aan. Kleine details waren zichtbaar in een [ $^{99m}\text{Tc}$ ]MDP muis kniege-wrichtscan, een [ $^{123}\text{I}$ ]NaI muis schildklierscan en een [ $^{99m}\text{Tc}$ ]DMSA muis nierscan, met een significant beter detailniveau dan mogelijk in preklinische *in vivo* SPECT.

De systeemmodellering voor beeldreconstructie van EXIRAD-3D werd ook verbeterd. Er werd een Fast Monte-Carlo-gebaseerde (FMC-gebaseerde) methode geïntroduceerd die een aantal voordelen had boven de beschikbare systeemmodelleringmethoden voor EXIRAD-3D ('traditionele methode' en 'ray-tracing-methode'). De resultaten toonden aan dat FMC een efficiënte, nauwkeurige en veelzijdige tool voor systeemmodellering is voor EXIRAD-3D en andere pinhole SPECT-systemen voor isotopen met lage of medium energie ( $\leq 285$  keV). FMC is meer algemeen dan de traditionele methode bij het wijzigen van isotoop- of acquisitieinstellingen, en rekenkundig efficiënter dan de ray-tracing-methode voor systemen met ultrahoge resolutie zoals EXIRAD-3D. FMC heeft ook het voordeel dat het gemakkelijk energieën kan combineren in een enkele systeemmatrix, wat tijd bespaart bij zowel systeemmodellering als beeldreconstructie.

Ook werd door middel van Monte-Carlo-simulaties een nieuwe collimator voor *ex vivo* gebruik, EXIRAD-HE genaamd, ontwikkeld en geoptimaliseerd voor het scannen van hoogenergetische isotopen zoals PET-isotopen, die resulteren in 511 keV-fotonen, en belangrijke theranostische isotopen (alpha of beta emitters zoals  $^{131}\text{I}$  (364 keV) of  $^{213}\text{Bi}$  (440 keV)) die gelijktijdig hoogenergetische gamma's uitzenden. Twee multi-pinhole collimatoren werden ontworpen voor 511 keV bij twee systeemgevoeligheden van 0.30% en 0.60%, en ook getest voor andere relatief hoge energieën. Deze collimatoren bereikten een gesimuleerde plaatsresolutie van 0.35 mm, 0.6 mm, 0.5 mm, 0.6 mm en 0.5 mm bij het afbeelden van respectievelijk  $^{131}\text{I}$ ,  $^{213}\text{Bi}$ ,  $^{18}\text{F}$ ,  $^{64}\text{Cu}$  en  $^{124}\text{I}$ .

De EXIRAD-techniek die in dit proefschrift wordt gepresenteerd, biedt veel betere resoluties dan wat kan worden bereikt met *in vivo* preklinische SPECT en PET scanners, terwijl het enorme hoeveelheden werk bespaart in vergelijking met het verkrijgen van 3D-beelden uit een set 2D-autoradiogrammen. Daarom kan deze techniek een zeer goede keuze zijn in een subgroep van farmaceutische en biologische onderzoeken, in het bijzonder als optie op een U-SPECT/CT- of een VECTOR/CT-beeldvormingssysteem dat longitudinale studies op hetzelfde dier mogelijk maakt, en een direct verband tussen *in vivo* en *ex vivo* datasets kan opleveren.

# Chapter 1

## General introduction

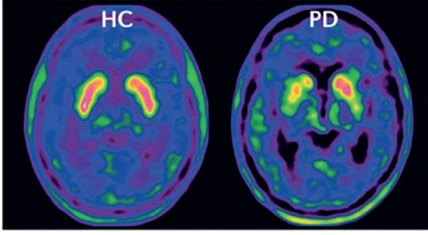
### 1.1 Nuclear molecular imaging

Molecular imaging refers to the visualisation, characterisation, and quantification of biological processes in humans and other living systems at the molecular and cellular level [1]. While other medical imaging techniques such as X-ray radiography, computed tomography (CT), magnetic resonance imaging (MRI) and ultrasound imaging are mainly used to reveal the physical structure of the body, molecular imaging offers information about how it is functioning. Current clinical applications of molecular imaging deal with e.g. cancer, neurological and psychiatric disorders, cardiovascular disease, infection and inflammation, gene therapy, and stem cell therapy [2, 3]. These applications greatly contribute to improved patient care in many clinics around the world. In clinical molecular imaging, nuclear imaging techniques - planar radioisotope imaging, single-photon emission computed tomography (SPECT), and positron emission tomography (PET) - are among the most commonly used modalities. Figure 1.1 shows some examples of SPECT and PET in imaging patients.

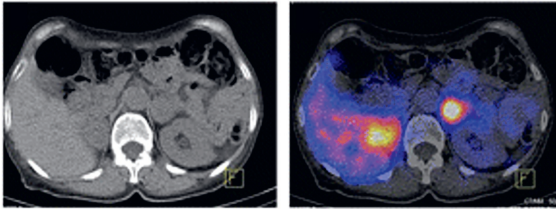
Next to clinical use, molecular imaging is also applied in preclinical research on small animals. Mice and rats are commonly used in these animal studies because of their high similarity with the human homolog, easy accessibility, and short reproductive cycles. Besides, the availability of many mature genetic manipulation techniques nowadays allows researchers to develop more clinically relevant animal models of human disease. For example, preclinical imaging of the dopaminergic system has been performed successfully in mouse and rat models of Parkinson's disease - a progressive nervous system disorder that affects human movement. These researches provide valuable results to support the interpretation of clinical studies performed in patients with this disease [4–6].

The scope of this thesis is preclinical SPECT and PET. To perform SPECT or PET imaging, an amount of radioactive “tracer” is administered (e.g. via injection) into the subject (Figure 1.2). After a specific amount of time, the tracer accumulates at one or multiple target locations that are intended to be imaged. Gamma ( $\gamma$ ) photons resulting directly from the tracer in the case of SPECT or from positron-electron annihilations in the case of PET are detected by so-called gamma-cameras, also known as detectors. The detectors cover sufficient angles around the subject, and information from all of those angles is used to compute a three-dimensional (3D) image of the activity distribution in a process called image reconstruction, which is discussed later in this chapter.

(a) Parkinson's disease



(b) Tumour: pheochromocytoma



(c) Alzheimer's disease

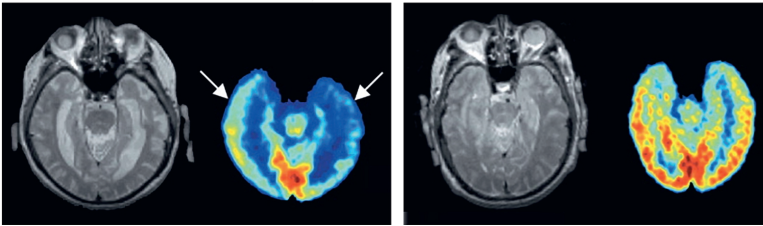


Figure 1.1: Examples of SPECT and PET imaging for diagnostic purposes in patients. (a)  $^{18}\text{F}$ -DOPA-PET images showing a healthy brain (HC; left), and marked asymmetric uptake in a patient with early-stage Parkinson's disease (PD; right). (b)  $^{99\text{m}}\text{Tc}$ -MIBG SPECT/CT images showing hot spots and enlargement of adrenal gland, indicating pheochromocytoma. (c)  $^{18}\text{F}$ -FDG-PET/MRI images of an subject with Alzheimer's disease (left) and a normal-control subject (right). The figures are adapted and reprinted with permission from [7–9].

Unlike SPECT, which images single gamma photon emitters (Figure 1.2(a)), PET usually employs near-simultaneous detection of the annihilation photon pairs (Figure 1.2(b)); when the photon pair is detected, the two detected positions define a line on which the annihilation likely took place. This technique is referred to as coincidence PET. It is also possible to image the annihilation photons from PET tracers in the same way as is done in SPECT by using a physical collimator to obtain information on the direction that the detected photons came from. In this case, the collimator is positioned between the object and the detector. It is made of a dense material with high photon-stopping power (e.g. tungsten, lead) and designed in such a way that only photons from certain directions can pass through it to reach the detector. For this purpose, holes are made in the collimator, and their shapes and arrangement define the type of collimator such as parallel-hole, cone-beam, fan-beam, slit-slat, or pinhole collimator.

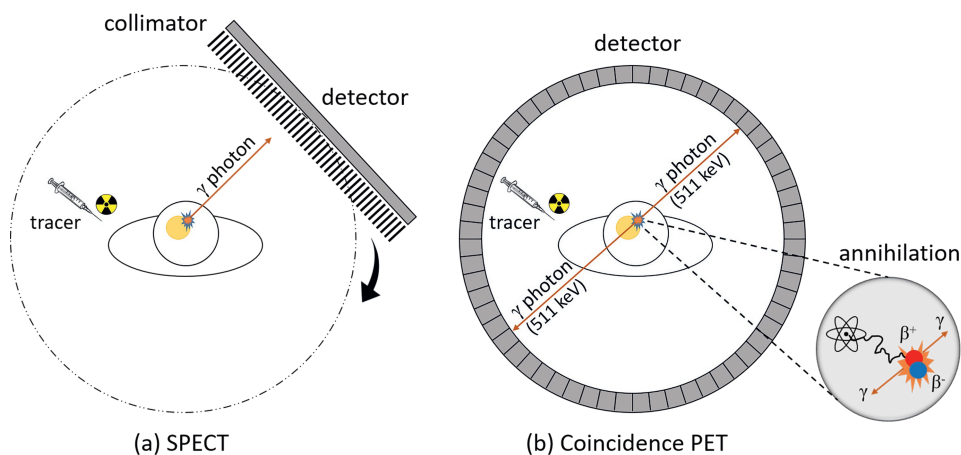


Figure 1.2: Working principle of (a) SPECT and (b) Coincidence PET.

The design of clinical SPECT and PET scanners cannot be directly applied to small animals because their achievable resolutions are just not sufficient; therefore, these modalities have been adapted significantly for preclinical imaging. One of the common adaptations in preclinical SPECT, which can also be utilised to image PET isotopes, is the use of multi-pinhole technologies, as will be discussed further in the next sections.

## 1.2 Pinhole collimation

The most widely used collimator types in SPECT systems use either parallel holes or pinholes. The pinhole collimator has a unique advantage over the parallel-hole collimator, particularly when imaging small objects. With a parallel-hole collimator, photons travel through the collimator in the direction approximately perpendicular to the detector, which results in a projection on the detector of the same size as the object (Figure 1.3). In this case, the best image resolution that can be achieved is the detector's spatial resolution, which is usually limited (e.g. 3.5 mm in conventional gamma detectors). On the other hand, with a pinhole collimator, the object can be magnified through the pinhole, creating a large projection image if the distance from the object to the pinhole is chosen to be shorter than the distance from the pinhole to the detector (Figure 1.3). In this way, the image resolution can be significantly better than the detector resolution. For example, using a single-pinhole collimator, a resolution of 200  $\mu\text{m}$  was achieved in two-dimensional (2D) *in vivo* mouse thyroid imaging with  $^{125}\text{I}$ , while the detector used had an average intrinsic resolution of 3.1 mm [10].

Nowadays, collimators for 3D radioisotope imaging (SPECT and PET) usually contain multiple pinholes to improve sampling, system sensitivity (defined as the fraction of the number of detected photons over the total number of photon emissions), and several other

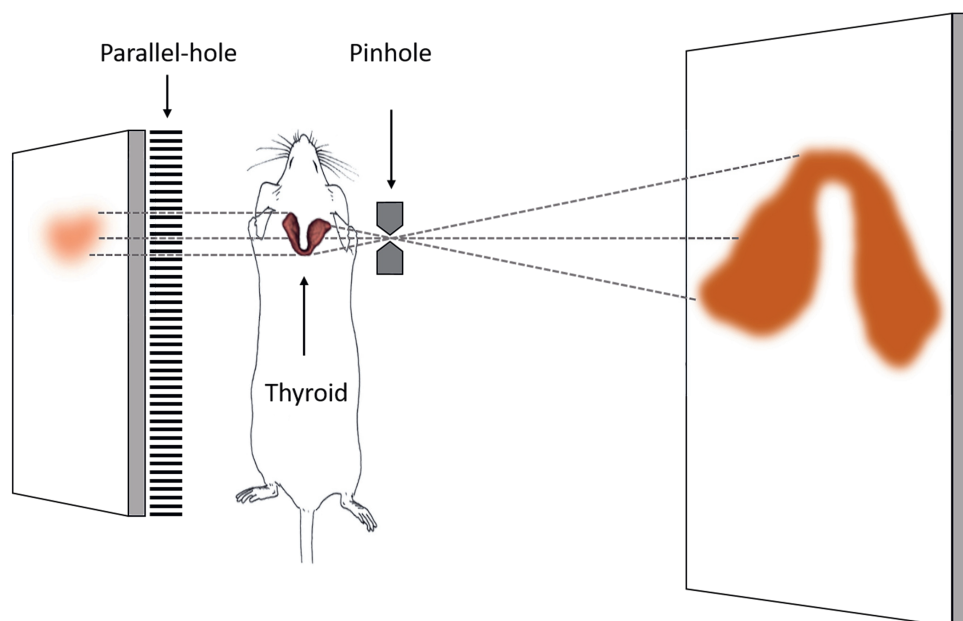


Figure 1.3: Illustration of imaging a mouse thyroid with parallel-hole and pinhole collimation.

system properties. A higher sensitivity of the scanner is desirable to reduce scan time and required tracer activity. The pinholes are either rotated or firmly placed around the subject in such a way that the geometry provides sufficient angular sampling to form 3D images.

When designing a multi-pinhole collimator, a large number of parameters needs to be taken into account, such as the pinhole diameter and its opening angle, the number of pinholes, the pinholes' arrangement, the collimator material, the distance from pinholes' centres to the object and to the detector, and the amount of pinhole projection overlapping. These parameters form a huge set of possible collimator configurations. To evaluate a configuration, the achievable resolution and sensitivity serve as the two major measures. Generally, there is a trade-off between resolution and sensitivity; for example, decreasing the pinhole's diameter improves the image resolution, however, at the expense of reducing the sensitivity. In a typical collimator design procedure, resolution (or sensitivity) is fixed at a desirable value, and the collimator's parameters are adjusted to give the best sensitivity (or resolution). Note that the ultimate scanner performance can depend on many other parameters (such as the volume that can be imaged), and also on the imaging task.

Collimator optimisation can be based on analytical models of pinhole collimators, e.g. [11–15], which is efficient in terms of computational speed. However, it should be noted that analytical optimisation does not always guarantee an optimal solution because not all collimator parameters and physics processes in the real imaging systems are captured in the models. For instance, with the analytical models, photon scattering is excluded, which would sometimes have a significant effect in imaging, and complex collimator geometries

are often simplified, inducing certain approximations. Therefore, analytical optimisation could be used in an initial design step, and then an accurate simulator such as a Monte Carlo simulator could serve as the tool for the final optimisation. Besides, collimator optimisation is ideally based on complete systems simulations (including image reconstruction) instead of looking only at individual measures such as sensitivity or system resolution. After all, experimental characterisation is necessary to assess the real-world performance of the imaging system.

### 1.3 Pinhole microSPECT and microPET

A majority of high-resolution preclinical SPECT imaging systems (microSPECT) is equipped with multi-pinhole collimators [13, 16–27], offering *in vivo* 3D image resolutions down to 250  $\mu\text{m}$ . These multi-pinhole systems are diversified over a wide range of characteristics, e.g. knife-edge versus channel-edge pinhole, round versus square pinhole, stand-alone system versus integrated add-ons on existing clinical scanners, and moving versus stationary collimator and detector.

A typical example of microSPECT is the U-SPECT system commercialised by MILabs B.V., Utrecht, the Netherlands [17, 21]. It consists of a cylindrical multi-pinhole collimator surrounded by three large NaI(Tl) detectors configured in a stationary triangular setup (Figure 1.4) - both the collimator and the detectors do not move during the scan. This configuration has advantages, compared to a non-stationary collimator-detector setup, in system calibration, maintenance, and dynamical imaging possibilities [28–31].

The U-SPECT collimators are exchangeable with a set of multi-pinhole collimator tubes for a wide variety of imaging applications. In these collimators, all pinholes focus on a central field-of-view (CFOV) such that the activity distribution inside the CFOV can be visualised without the movement of any system's component. To image a larger volume than the CFOV, the subject is translated to multiple positions inside the cylindrical collimator using a high-precision three-degree-of-freedom robotic stage, and detected photons from all of those positions are used together to form a 3D image [32].

Today, sub-millimetre imaging of PET isotopes (microPET) is possible with VECTOR, a system that is also commercialised by MILabs B.V. VECTOR applies a novel clustered multi-pinhole collimator [33, 34]. Due to the thick collimator wall and a smart arrangement of narrow pinholes in this collimator, high-energy photons are effectively collimated without sacrificing the size of the CFOV. Compared to traditional coincidence microPET systems (which are based on the near-simultaneous detection of annihilation photons to infer the positron emission location), VECTOR effectively suppresses some image degrading effects. These effects include limited detector resolution, non-collinearity of annihilation photons, and random coincidences, which would be significant in high-resolution imaging. Additionally, VECTOR has the advantage of being able to simultaneously image SPECT and PET isotopes, performing multi-isotope PET [35] by making use of prompt gammas, and imaging important high-energy isotopes such as  $^{131}\text{I}$ ,  $^{213}\text{Bi}$ , and  $^{209}\text{At}$  [34–41]. VECTOR also has the ability to perform positron-range free imaging [35].

Many advances in U-SPECT and VECTOR systems have been continuously developed over the years in both collimator and detector design and software optimisation, with close collaboration between MILabs B.V., the University Medical Center Utrecht, and Delft University of Technology, pushing both resolution and sensitivity of the systems.

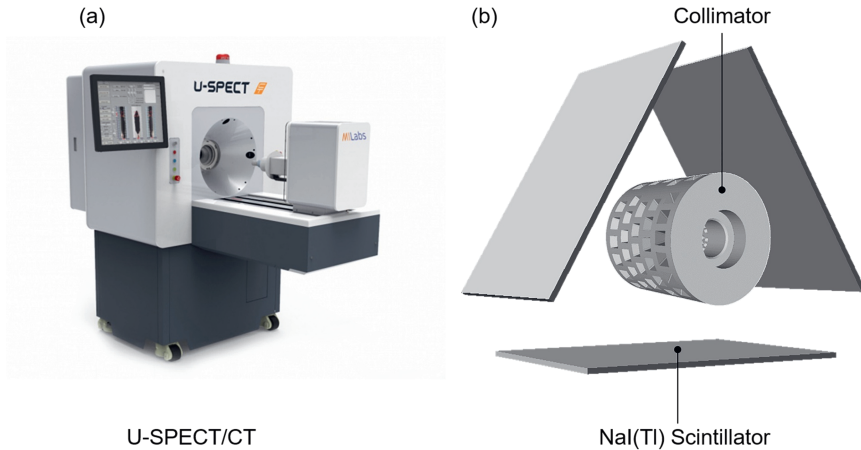


Figure 1.4: (a) Image of the U-SPECT/CT system (MILabs B.V.). (b) A multi-pinhole collimator and three large NaI(Tl) scintillation detectors configured in a stationary triangular setup.

## 1.4 Pushing resolution with *ex vivo* imaging

High-resolution nuclear imaging is desirable to resolve small details in the target object. A straightforward approach to increase image resolution with pinhole SPECT/PET is to image a smaller object, in which case the pinholes can be placed closer to the object to increase the magnification factor, instead of having an impractically large detector placed further from the pinholes. That is the reason why pinhole SPECT/PET is more often applied to small animals like mice than to humans. Currently, the best achievable resolutions of *in vivo* pinhole SPECT and PET are 250  $\mu\text{m}$  and <600  $\mu\text{m}$ , respectively [27, 42], and it is hard to push the resolution further with *in vivo* imaging due to the limited size of the animal.

To date, when a higher resolution than what is offered by *in vivo* SPECT/PET is required, 2D autoradiography is implemented [43–46]. In this technique, the radioactive tissue is sliced, and each obtained thin layer is scanned to form a 2D image. As presented in Figure 1.5, autoradiography can reach resolutions from <150  $\mu\text{m}$  to several  $\mu\text{m}$  [47], which is significantly better than that reached in *in vivo* SPECT/PET. However, traditional autoradiography requires complex sample preparation and manipulation. Besides, constructing a 3D image from the obtained 2D slices with this technique is still a difficult task because this process is error-prone and potentially causes distortion and other artefacts in the obtained image volume.

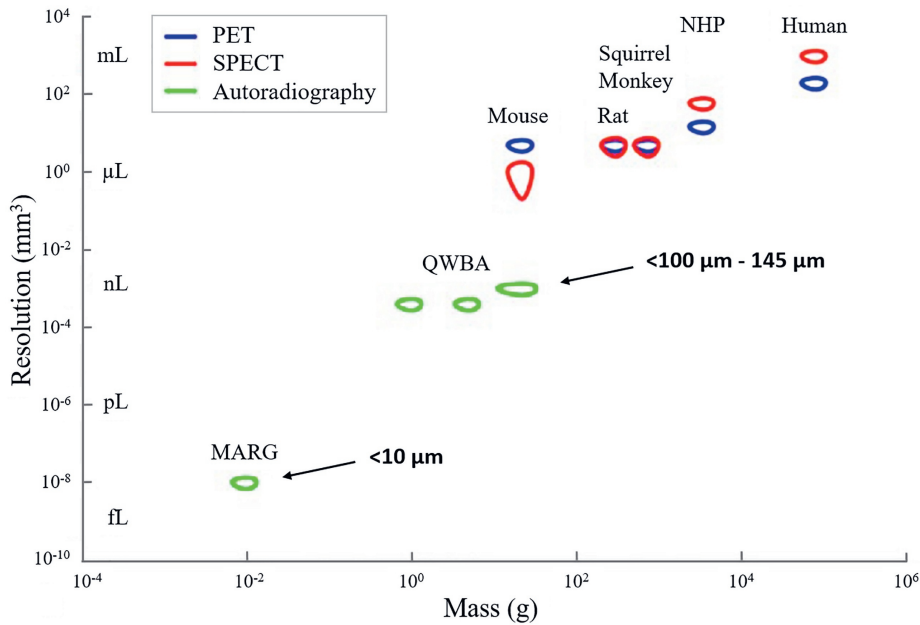


Figure 1.5: The resolution that can be obtained with common nuclear molecular imaging techniques. MARG: Microautoradiography. QWBA: Quantitative Whole-Body Autoradiography. NHP: Non-human Primates. This figure is adapted and reprinted with permission from [47].

Given the disadvantages mentioned above, it may be useful to have *ex vivo* SPECT/PET scanners that exploit the principle of large pinhole magnification. By imaging a small tissue sample such as a mouse brain, a mouse thyroid, or tumour tissue, the pinholes can be placed even closer to the object than when scanning a mouse, which results in increased magnification. This approach can provide higher resolutions than *in vivo* imaging while still intrinsically producing fully 3D images. This is nowadays enabled due to advances in pinhole SPECT/PET, such as the ability to precisely engineer tiny pinholes made of a high stopping power material, or better-optimised software for accurately generating images for such ultra-high-resolution *ex vivo* scanners. *Ex vivo* SPECT/PET, however, does not enable a resolution as high as typical traditional 2D autoradiography. Still, it will be especially valuable when combined with its *in vivo* counterparts in a way that only requires a little more effort, to provide a direct link between the *ex vivo* and *in vivo* datasets.

## 1.5 Optimising system modelling for image reconstruction

Image reconstruction in SPECT/PET is the process to obtain a 3D image representing the activity distribution from a set of 2D projections acquired by the detectors. Image reconstruction algorithms are classified into two main categories: analytical methods and iterative methods [48]. The analytical methods are fast but relatively inaccurate

because they exclude some aspects in the imaging process, such as distance-dependent resolution and sensitivity, photon scatter, noise in the projection data, and are only suitable for a limited number of system geometries. On the other hand, iterative methods are more time-consuming but have better noise properties and can utilise accurate models of photon transport physics. They are suitable for highly complex system geometries like multi-pinhole collimators. A standard iterative image reconstruction method is Maximum Likelihood Expectation Maximisation (MLEM) [49, 50] with one of the most popular accelerated versions known as Ordered Subsets Expectation Maximization (OSEM) [51]. In OSEM, the projection data needs to be divided into “balanced” subsets, and in each iteration, only a subset of projection data is used, which is much faster while producing an almost as good image, compared to using the full projection data as in MLEM.

The reconstruction algorithms in U-SPECT and VECTOR are based on improved versions of OSEM: For a better subset balance, pixel-based OSEM (POSEM) [52] was developed in which projection data is divided into subsets of detector pixels distributed over the projections instead of subsets consisting of sets of complete projection images. Further acceleration in reconstructing low-activity regions is achieved with similarity-regulated OSEM (SROSEM) [53], in which the number of subsets for updating a voxel depends on how similar the reconstruction algorithm would update the estimated activity in that voxel with different subsets. Most recently, a combined dual-matrix dual-voxel (DM-DV) approach was implemented [42] to further speed up the reconstruction while maintaining image quality by having two matrices for forward projection and backprojection, different in the amount of low-frequency information and the voxel sizes in the matrices.

The prerequisite for image reconstruction is a process called system modelling to calculate a system matrix for a specific imaging situation. The system matrix consists of point spread functions (PSFs) that contain the probabilities that photons coming from a certain voxel location in the object are recorded in a certain pixel in the detector. In U-SPECT and VECTOR systems, two methods have been used to obtain the system matrix. The first one, known as “traditional” method, is based on model-based interpolation from a set of measured PSFs to calculate all necessary PSFs for the matrix [54]. The second one, known as “ray-tracing” method, accurately calculates the photon transport through the system for all voxel-pixel combinations and saves them in an efficient way [36]. The traditional method is suitable for low- and medium-energy isotopes such as  $^{125}\text{I}$  (27 keV),  $^{201}\text{Tl}$  (71 keV),  $^{99\text{m}}\text{Tc}$  (140 keV), and  $^{111}\text{In}$  (171 and 245 keV), while the ray-tracing method is mostly used for high-energy isotopes such as  $^{131}\text{I}$  (364 keV),  $^{213}\text{Bi}$  (440 keV), and PET isotopes (511 keV).

For ultra-high-resolution *ex vivo* SPECT/PET, system modelling can be optimised further to address the following challenges with the traditional and ray-tracing matrices. With the traditional matrix, the size of the radioactive point source used in measuring the initial set of PSFs should be smaller than the matrix voxel size. It is challenging to fabricate such a tiny point source still containing a sufficiently high activity for acquiring almost noiseless PSFs. With the ray-tracing matrix, a huge number of photon paths needs to be calculated for a high-resolution system like EXIRAD-3D, which would result in an impractically long computation time. Besides, many important isotopes, such as  $^{111}\text{In}$ ,  $^{67}\text{Ga}$ , and  $^{90}\text{Y}$ ,

emit a complex energy spectrum with, e.g. multiple photopeaks or continuous spectra. Optimally reconstructing data from these isotopes usually requires multiple ray-tracing matrices for multiple energy windows, which increases the computational complexity in both system modelling and image reconstruction. Therefore, it is of interest to develop a new system modelling method that is accurate and efficient for ultra-high-resolution *ex vivo* SPECT/PET and also easily applicable to different energies and isotopes.

## 1.6 Research aims and thesis outline

This thesis aims to develop and validate new ultra-high-resolution *ex vivo* 3D imaging modules to use with existing preclinical SPECT and PET systems (in this work developed for the U-SPECT and VECTor, MILabs B.V.) for a wide range of energies, by means of dedicated multi-pinhole collimators and by utilising accurate system modelling for high-resolution image reconstruction.

**Chapter 2** evaluates different materials for an ultra-high-resolution *ex vivo* SPECT collimator (EXIRAD-3D) used in U-SPECT and VECTor with low- and medium-energy isotopes (e.g. 27-245 keV). From an existing design of this collimator (MILabs B.V.), different materials were evaluated, by fixing the system sensitivity and determining which material offers the highest image resolution. This study is important because it provides knowledge on which material is both effective, practical, and economical in this application. The collimators with different materials are assessed based on full image reconstructions with Monte Carlo simulations which are validated by comparison to experimental data. **Chapter 3** presents the description of a commercialised version of the EXIRAD-3D, and its experimental performance characterisation with phantom scans and mouse knee joint, thyroid, and kidney scans. **Chapter 4** introduces a Fast Monte-Carlo based system modelling method that is accurate and efficient for EXIRAD-3D and overcomes the challenges with the current traditional and ray-tracing matrix generation methods. This method allows an easy adaptation and combination of matrix energies, and it is also straightforward to apply to other multi-pinhole imaging systems. The results are evaluated with both experimental and simulated scans with various radioisotopes. **Chapter 5** optimises and evaluates a new EXIRAD option (EXIRAD-HE) for *ex vivo* imaging of a wide range of high-energy isotopes (e.g. 364-603 keV), using Monte Carlo simulations of several image quality phantoms as well as digital mouse tissue phantoms. **Chapter 6** summarises the findings in this thesis with some more discussion on the results and recommendations for possible further researches in this area.



## Chapter 2

## 2

# Evaluation of pinhole collimator materials for micron-resolution *ex vivo* SPECT

---

This chapter is adapted from:

**Minh Phuong Nguyen**, Marlies C. Goorden, Chris Kamphuis, and Freek J. Beekman. Evaluation of pinhole collimator materials for micron-resolution *ex vivo* SPECT. *Physics in Medicine & Biology* 64.10: 105017, 2019.

*Pinhole collimation is widely recognized for offering superior resolution-sensitivity trade-off in SPECT imaging of small subjects. The newly developed EXIRAD-3D autoradiography technique (MILabs B.V.) based on a highly focusing multi-pinhole collimator achieves micron-resolution SPECT for cryo-cooled tissue samples. For such high resolutions, the choice of pinhole material may have a significant impact on images. Therefore, this chapter aims to compare the performance of EXIRAD-3D with lead, tungsten, gold, and depleted uranium pinhole collimators designed such that they achieve equal sensitivities. Performance in terms of resolution is characterized for several radioisotopes, namely  $^{111}\text{In}$  (171 keV and 245 keV),  $^{99\text{m}}\text{Tc}$  (140 keV),  $^{201}\text{Tl}$  (71 keV), and  $^{125}\text{I}$  (27 keV). Using Monte Carlo simulation, point spread functions were generated and their profiles as well as their full-width-at-half-maximum and full-width-at-tenth-maximum were determined and evaluated for different materials and isotopes. Additionally, simulated reconstructions of a Derenzo resolution phantom, validated with experimental data, were judged by assessment of the resolvable rods as well as a contrast-to-noise ratio (CNR) analysis. Our results indicate that using materials with higher photon-stopping power yields images with better CNR for the studied isotopes with improvements ranging from 1.9% to 36.6%. Visual assessment on the reconstructed images suggests that for EXIRAD-3D, the tungsten collimator is generally a good choice for a wide range of SPECT isotopes. For relatively high energy-isotopes such as  $^{111}\text{In}$ , using gold inserts can be beneficial.*

## 2.1 Introduction

The pinhole has enabled ultra-high-resolution 3D radionuclide imaging in small animals [55]. Since the use of pinholes in the earliest gamma cameras [56–58], imaging systems with pinhole collimators have significantly evolved over the years pushing the imaging performance limits. A majority of preclinical SPECT systems is now equipped with multi-pinhole collimators leading to sub-millimetre resolution [13, 16, 17, 19–25, 59, 60], even down to 0.25 mm [27]. Sub-millimetre resolution has also been achieved in imaging of PET isotopes and simultaneous imaging of PET and SPECT isotopes using clustered pinholes [34, 61]. Moreover, several multi-pinhole clinical SPECT systems are available on the market [62] or being developed [63–69]. Generally, the trade-off between resolution and sensitivity (i.e., the fraction of emitted gamma photons that are recorded by the detectors) of a pinhole collimator can be enhanced when the field-of-view is decreased. That is because the smaller the volume to be imaged, the closer the pinholes can be placed to the radioactivity which increases sensitivity and leads to larger pinhole magnification factors which can enhance resolution.

On this line of development, MILabs B.V. has introduced EXIRAD-3D for SPECT scanning of cryo-cooled tissue samples, also called automated 3D autoradiography, which avoids time-consuming and error-prone steps present in traditional autoradiography. In traditional autoradiography, the tissue sample needs to be cryo-cooled, then sliced into thin sections, and scanned for hours or days with digital 2D films or phosphor screen readers. The obtained 2D images are subsequently registered to form a 3D volume representing the radioactivity distribution within the sample. This process potentially causes distortion in the 3D volume. With EXIRAD-3D, the whole tissue sample is cryo-cooled in a specially

designed sample holder to avoid tracer leaking and tissue deformation, and scanned to form a 3D image. This novel technique is available on recent U-SPECT/CT and VECTor<sup>4,5&6</sup>/CT systems, which are the successors of the systems described in [21, 34]. It uses a dedicated focusing multi-pinhole collimator made of tungsten alloy mounted within three large-field-of-view gamma-cameras with NaI(Tl) crystals in a stationary set-up. This collimator has a small bore size that allows high-resolution *ex vivo* scanning, but due to its small size, it is not suited for *in vivo* imaging. Due to the close pinhole-to-subject distance, EXIRAD-3D has a very high pinhole magnification and therefore can produce better than 140  $\mu\text{m}$  spatial resolution (or 2.7 nL) <sup>99m</sup>Tc-SPECT images, which gets into the resolution range of traditional autoradiography (from 0.01 pL to several nL, [47]). Optimising the collimator could further improve the resolution-sensitivity trade-off for such systems.

Collimator and system geometry optimisation in general is complex as there is a high number of degrees of freedom, such as aperture diameter, pinhole placement, pinhole opening angle, pinhole orientation, number of pinholes, pinhole-detector distance, or pinhole material. Here we focus on the role of the material used. Aside from the commonly used lead and tungsten, gold and depleted uranium have been used for pinhole collimators [10, 16, 17, 21, 60, 70–73]. Using materials with high stopping power is often preferred because it results in narrower point spread functions (PSFs) as photon penetration and scattering in the pinhole edges are reduced which can be expected to lead to better resolutions [74]. However, it would not be fair to judge the performance of pinhole materials only by their photon attenuation coefficient because the photons that are stopped by the material may contain information about their emission location that can still be useful in image reconstruction. One can instead compare resolution at equal sensitivities which can be accomplished by tuning the pinhole diameter for different materials. It was demonstrated in [75] that with equal sensitivities, the PSF full-width-at-half-maximum (FWHM) increased from lead, tungsten, gold, to uranium, while the PSF full-width-at-tenth-maximum (FWTM) decreased. However, the resolutions of final reconstructed images were almost independent of the material used for the SPECT systems investigated in that work. This implies that good system modelling for image reconstruction can at least partly compensate for pinhole edge penetration and scattering, and the evaluation of pinhole materials should be based on final reconstructed images. For a higher resolution system as EXIRAD-3D, it is not a priori clear if the findings from [75] still hold as the performance of such a system can be more sensitive to the collimator material used.

This work aims to compare EXIRAD-3D pinhole collimators made of different materials at equal system sensitivities. Four collimator materials (lead, tungsten, gold, and depleted uranium) were investigated for several radioisotopes, namely <sup>111</sup>In (171 keV and 245 keV), <sup>99m</sup>Tc (140 keV), <sup>201</sup>Tl (71 keV), and <sup>125</sup>I (27 keV). For each isotope, Monte Carlo simulation (MCS) of a full multi-pinhole collimator was performed to tune the pinhole diameters such that all collimators investigated obtained equal sensitivity. We then compared PSFs and reconstructed Derenzo resolution phantom images for different materials and isotopes.

## 2.2 Methods

### 2.2.1 EXIRAD-3D system with multi-pinhole collimator

2

For EXIRAD-3D imaging, the U-SPECT/CT or VECTor/CT system is equipped with a focusing multi-pinhole collimator mounted within three large-field-of-view gamma-cameras having 3.5 mm intrinsic spatial resolution and 10% FWHM energy resolution at 140 keV. Each gamma-camera is equipped with a 9.5 mm thick NaI(Tl) crystal having a usable area of 497.4\*410.6 mm<sup>2</sup> and read out by 55 photomultiplier tubes (PMTs). The collimator's core is cylindrical with an inner bore diameter of 10.5 mm and a wall thickness of 7.5 mm (Figure 2.1(a,b)) made of a tungsten alloy containing 92.5% tungsten, 5.25% nickel, and 2.25% iron. It has a total of 87 round knife-edge pinholes with pinhole centres at a radius of 12.5 mm from the z-axis (see Figure 2.1 for axes definition). The pinhole axes converge at a single point at the collimator centre, and they are distributed into five rings with the tilt angles indicated in Figure 2.1(a). There is also an 8-degree angular shift around the z-axis between adjacent rings. All pinholes have the same aperture diameter of 0.15 mm, and an opening angle of 26 degrees. The core is surrounded by an lead shielding tube with trapezium-shaped holes to prevent overlapping between pinhole projections (Figure 2.1(c)).

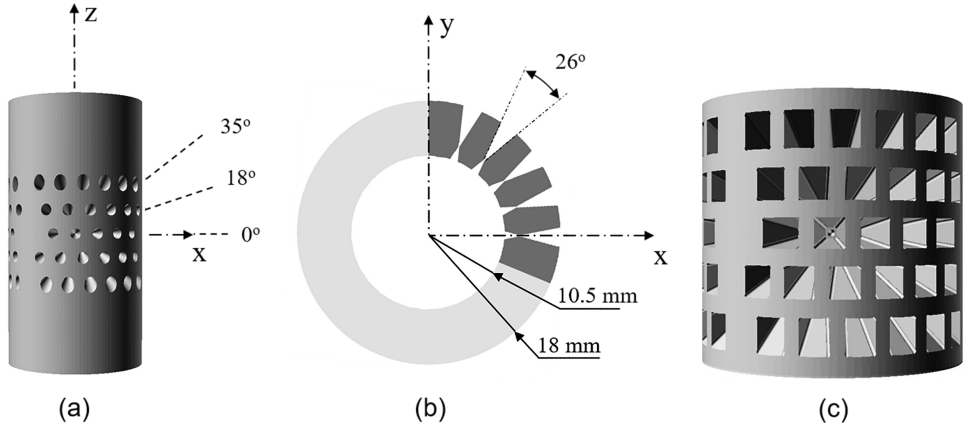


Figure 2.1: (a) The core of the dedicated focusing multi-pinhole collimator for EXIRAD-3D. (b) A cross-section in the xy-plane showing the pinholes that project on one of the three detectors. Rotating this group of pinholes  $\pm 120^\circ$  around the z-axis results in the pinholes projecting on the other two detectors. (c) The shielding with trapezium-shaped holes that surrounds the collimator's core.

### 2.2.2 Monte Carlo simulations

To simulate photon transport in the collimator and detector, we used the well-validated Monte Carlo simulation (MCS) software Geant4 Application for Tomographic Emission (GATE) [76–79]. GATE version 8.0 was used with Geant4 version 10 on a CentOS 6.6 cluster with 250 processors running simultaneously. Modelled physics processes include

photoelectric effect, Compton scattering, and Rayleigh scattering for gamma photons, as well as ionisation, bremsstrahlung, and multiple scatter for electrons. To simulate the triangular detector geometry, a set of three NaI-scintillators was created natively in GATE using three  $497.4 \times 410.6 \times 9.5 \text{ mm}^3$  rectangular boxes. The first scintillator was placed perpendicularly to the y-axis and centred at (0 mm, -210 mm, 0 mm), and the other two were created by rotating the first one by  $\pm 120$  degrees around the z-axis. Other details of the detectors such as exact light guide geometry and PMTs were not explicitly simulated in GATE but captured in the detector resolution (explained in Equation (2.1)). The collimator was mostly based on a computer-aided design (CAD) of the real commercialised collimator to keep precise pinholes and shielding's geometries, while we adjusted pinhole diameter and collimator material for this study. Since the role of material is most important on the pinhole edges and a lead shielding would perform as well as a shielding made of tungsten, gold, or uranium, we assumed that the whole collimator contains a single material without assigning a different material (lead) to the shielding. An STL file of the collimator exported from the CAD program was inserted into GATE. This STL file format is only supported in GATE for version 8.0 and higher. We made sure the STL meshes well resembled the continuous model by using a large number of triangles, especially at the pinhole apertures. On average, each collimator is composed of 170900 triangular faces, and each pinhole aperture is formed by 40 aperture blades. A reasonable 12-minute time was required to render an STL collimator. The STL files were prepared in Netfabb (Autodesk, Inc., San Rafael, California) to remove unexpected gaps, non-manifold edges/vertices, and intersecting triangles before importing it into GATE. GATE outputs the interaction time, total deposited energy, and energy-weighted average interaction location in the scintillators for each gamma photon. Photon interaction locations were sampled with a pixel grid of  $1.072 \times 1.072 \text{ mm}^2$  (pixel size of the experimentally used detector). A digital detector mask was applied to mask areas where no direct photons from the object are expected to be detected as is also done in the reconstruction software of the real system [54].

The full isotopes' emission spectrum and activity decay, retrieved from [80], were considered for each studied isotope. In addition, we randomised the interaction energy and position for each event using Gaussian probability distributions to simulate the detector's energy resolution and spatial resolution. Energy dependence of these resolutions was taken into account as summarised in Table 2.1. As these resolutions were only determined experimentally for a few energy values (indicated in bold in the table), the rest of them was calculated using models from literature. For the detector's energy resolution we used [76]:

$$R_{\text{energy}} = \sqrt{2.35^2 \frac{1.1}{LE\bar{p}\bar{\epsilon}} + R_i^2}, \quad (2.1)$$

where  $L$ ,  $E$ ,  $\bar{p}$ ,  $\bar{\epsilon}$ , and  $R_i$  are light yield, deposited energy, light collection efficiency (i.e., the fraction of scintillation photons that arrive at the PMTs' photocathodes), quantum efficiency of the PMTs, and intrinsic resolution of the detector in FWHM, respectively. Here we set for the NaI(Tl) detector a light yield of 38 photons/keV, a quantum efficiency of 30%, and 6% FWHM intrinsic energy resolution. These values were retrieved from [81–83]. Then, with the measured detector's energy resolution at 140 keV of 10% FWHM, the light

collection efficiency was calculated to be 59.5%. The detector's spatial resolution was measured for our system to be 3.5 mm FWHM at 140 keV, and scaled by the reciprocal of the square root of the photon's energy, as was also done in other studies [13, 84]:

$$R_{spatial} = 3.5 \sqrt{140/E}, \quad (2.2)$$

where  $E$  is deposited energy in keV. Note that even though the detector's spatial resolution is in the mm range, system resolution can be significantly better due to the high pinhole magnification [85], and reconstructed resolution can be even better than the system resolution when accurate photon transport and detector blurring are modelled in image reconstruction. Table 2.1 also presents some of the isotopes' properties and the photopeak windows for acquisition. For  $^{111}\text{In}$ , which has two prominent photopeaks, data from both photopeaks are acquired simultaneously.

Table 2.1: MCS settings for different isotopes. For spatial resolution and energy resolution of the detector, numbers in bold denote experimentally determined values, and the rest is calculated using Equations (2.1) and (2.2).

Isotope	Peak energies (keV)	Half-life	Detector's spatial resolution (mm)	Detector's energy resolution (%)	Photopeak windows
$^{111}\text{In}$	245	2.8 d	2.6	8.5	20% at 245 keV
	171		3.2	9.4	20% at 171 keV
$^{99m}\text{Tc}$	140	6.0 h	<b>3.5</b>	<b>10</b>	20% at 140 keV
$^{201}\text{Tl}$	71	3.0 d	4.9	12.7	40% at 71 keV
$^{125}\text{I}$	27	59.4 d	8.0	<b>25</b>	60% at 27 keV

### 2.2.3 Determination of pinhole diameters to obtain equal sensitivities

For each isotope, the pinhole aperture diameter was adjusted to obtain equal sensitivity for different materials. To this end, we simulated projections of a uniform activity distribution with the size of the central field-of-view (CFOV) - a cylinder with a diameter and a length of 4 mm that can be observed simultaneously by all pinholes - and sensitivity was calculated as the number of detected counts within the photopeak window over the simulated number of emissions ( $5.5 \cdot 10^9$ ). This way, we obtained the average sensitivity over the CFOV. For each isotope used, we always fixed the pinhole diameter for the tungsten collimator to 150  $\mu\text{m}$  (diameter of the pinholes in the real collimator) and varied the pinhole diameter with a step size of 2  $\mu\text{m}$  for other materials to achieve (nearly) equal sensitivity. Characteristics of the four investigated materials are provided in Table 2.2 at the energies corresponding to the primary emission of the considered radioisotopes, namely  $^{125}\text{I}$ ,  $^{201}\text{Tl}$ ,  $^{99m}\text{Tc}$ , and  $^{111}\text{In}$ . Note that here we only simulated pure materials. In actual collimator manufacturing, alloys of these materials are often used. The influence of this is discussed further at the end of this chapter.

Table 2.2: Densities and attenuation coefficients of the studied materials at the considered energies. The values were obtained from NIST [86, 87].

Materials	Density (g cm <sup>-3</sup> )	Linear attenuation coefficient $\mu$ (mm <sup>-1</sup> )				
		27 keV ( <sup>125</sup> I)	71 keV ( <sup>201</sup> Tl)	140 keV ( <sup>99m</sup> Tc)	171 keV ( <sup>111</sup> In)	245 keV ( <sup>111</sup> In)
U	18.95	102.567	8.754	5.800	3.604	1.550
Au	19.32	69.730	5.688	4.260	2.560	1.114
W	19.30	57.577	20.482	3.621	2.200	0.952
Pb	11.53	45.077	3.703	2.751	1.655	0.708

## 2.2.4 PSF comparison for single pinholes

By comparing the PSFs obtained with different collimator materials at equal system sensitivities, we analysed the magnitude of the pinhole penetration and scatter components in the pinhole projections. To this end we considered the PSF projecting from a point source at the collimator's centre through a pinhole oriented perpendicular to one of the detector planes. The number of emitted gamma rays was set to  $4 \cdot 10^{11}$ . Only for this comparison, the PSFs were sampled to a smaller grid of  $0.2 \cdot 0.2$  mm<sup>2</sup> on the gamma detector, instead of the customarily used pixel size of  $1.072 \cdot 1.072$  mm<sup>2</sup> when we make projections. We compared the 2D PSFs and their profiles, as well as FWHMs and FWTMs. To calculate a PSF's FWHM (or FWTM), we fit the PSF to a 2D Gaussian shape using the Levenberg–Marquardt algorithm [88, 89], and drew a contour on the fitted PSF that represents the isoline at the intensity equal to one half (or one-tenth) of its maximum using the Marching Squares algorithm [90]. Then, the average diameter of the contour was taken and projected back to the image domain by dividing it by the pinhole magnification factor to obtain the FWHM (or FWTM).

## 2.2.5 Multi-pinhole reconstruction

### Phantom scan simulation

A Derenzo phantom having six sectors of hollow cylindrical rods with varying diameters that contained a radioactive solution inside was simulated (Figure 2.2). In each sector, the distance between centres of two adjacent rods was twice the rod diameter. The phantom was created natively in GATE, so it had no discretisation.

For each radioisotope, a realistic activity concentration that can be attained in animal experiments was simulated on the phantom: 26.3 MBq/ml, 212 MBq/ml, 8.8 MBq/ml, and 185 MBq/ml for <sup>111</sup>In, <sup>99m</sup>Tc, <sup>201</sup>Tl, and <sup>125</sup>I, respectively. The activity concentrations for <sup>99m</sup>Tc and <sup>125</sup>I were derived from real experimental scans of a mouse knee joint and a mouse thyroid on our EXIRAD-3D system. In the knee joint scan, 300 MBq <sup>99m</sup>Tc-methylene diphosphonate was injected into a mouse and bone tissue containing 6 MBq activity was imaged. In the thyroid scan, 39 MBq <sup>125</sup>I-Na was injected into a mouse and thyroid tissue

containing 1.6 MBq activity was imaged. The activities on the tissues were measured in a dose calibrator (VDC-304, Veenstra Instruments, the Netherlands). Knowing the total activity in the tissue sample and the activity distribution on the corresponding SPECT image, the activity concentration (MBq/ml) for each image voxel was calculated. Then, the average activity concentration over the knee joint or the thyroid was used for simulations in this work. Note that in this study the animal was sacrificed and its tissue was cryo-cooled shortly after activity injection. In this case, radiation-induced biological effects do not play a role. The activity concentrations for the other isotopes were obtained from biodistribution studies from literature [91, 92] which were for *in vivo* scans.

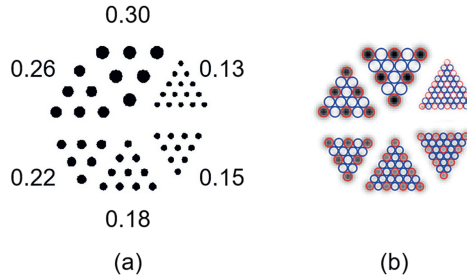


Figure 2.2: (a) The Derenzo phantom used to evaluate image resolution. Listed rod sizes are in mm. The rods have equal lengths of 2 mm leading to a total volume of 3.2  $\mu\text{l}$ . (b) The mask for calculating contrast-to-noise ratio that was used to evaluate reconstructed images as explained at the end of Section 2.2.5. Red circles represent activity-containing regions while blue circles are drawn on the background. Each region spans a depth of 0.8 mm around the phantom's central plane.

A total scan time of 16 hours was simulated assuming an overnight scan, and activity decay was taken into account for each isotope. The scanning focus method [32] in which the phantom is scanned at multiple bed positions and images are reconstructed from all projection data of the different bed positions was used to improve sampling. A total of nine bed-positions on a plane perpendicular to the collimator axis were simulated in GATE with equal scan time for each position.

We also simulated realistic background radiations that could be significant in these phantom scans as the activity contained in the small-volume phantom (3.2  $\mu\text{l}$ ) was rather low. To this end, the count rate from the background radiation within the photopeak window for each isotope in Table 2.1 was measured with a U-SPECT/CT system at MILabs B.V., Utrecht, the Netherlands to be 175 cps, 60 cps, 100 cps, and 45 cps for  $^{111}\text{In}$  (both photopeak windows),  $^{99m}\text{Tc}$ ,  $^{201}\text{Tl}$ , and  $^{125}\text{I}$ , respectively. Then with the assumption that the background counts are uniformly distributed over the detector pixels, the average number of background counts on each detector pixel over the scan time per bed position was calculated, and its Poisson realisation was added to the projection at that pixel.

For each simulated scan, the photons that deposit energy in the two side windows adjacent to the photopeak, each having a width of 25% of the photopeak window's width, were also recorded for the purpose of scatter correction. Background counts were also added to the side window projections in the same way as for the photopeak window. Here, the

number of counts from background radiation within a side window was assumed to be 25% of the number of counts from background radiation within the corresponding photopeak window.

### System matrix generation

Accurate modelling of the system matrix is necessary for high-quality reconstructed images. The matrix, consisting of PSFs corresponding to all voxels in the field of view, represents the probabilities that a photon emitted from a voxel is recorded at a detector pixel. In this study, we based the matrix generation method on the one that is experimentally used and described in [54]. In this method, a limited number of PSFs is measured, and then a full matrix is obtained by model-based interpolation. This approach currently performs well in reconstructing the EXIRAD-3D experimental scan data [93]. We used the MCS described in Section 2.2.2 to simulate the point source measurements mimicking what is done in the experimental procedure.

For each matrix generation, a total of 435 point source positions was simulated with GATE. They were placed on a 1 mm grid near the collimator's centre and a 2 mm grid further away from the centre (Figure 2.3). We assumed that for  $^{99m}\text{Tc}$  the point source contained an activity of 46 MBq and was scanned for 15 seconds at each position, as in the common experimental procedure. For the other isotopes, the same number of emitted photons was assumed from the point source. This way the simulation took three days.

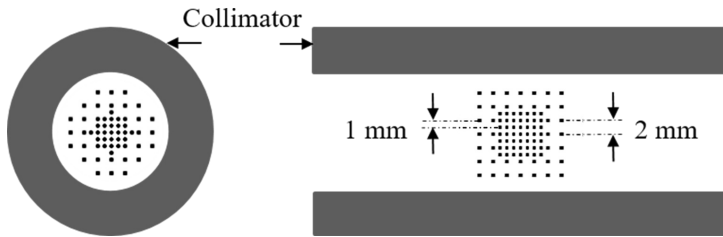


Figure 2.3: Point source positions placed inside a sketch of the collimator, indicated by solid points.

The number of point source positions is just 1/200,000 of the required number of image voxels in the system matrix for a 0.05 mm voxel size. The model-based interpolation procedure is based on transforming a nearby PSF using some estimated parameters (PSF's flux, width, and centre location) and is explained in detail in [54]. For multi-pinhole collimation, it is not necessary to store all voxel-pixel combinations in the system matrix because only the photons that go through the pinholes or pass the pinhole's edge have considerable probabilities to be detected. Therefore, the PSF parts having negligible intensities are not saved such that  $C\%$  of the area under the PSF is excluded.  $C\%$  was set to 4%, except for  $^{125}\text{I}$  ( $C\% = 10\%$ ) to keep reasonable matrix sizes on disk. Reducing the matrix size also helps to speed up image reconstruction.

The shielding with trapezium-shaped holes surrounding the collimator makes sure that each

pinhole projects in a separate segment on the gamma camera and a precise segmentation of the detector area into these separate segments needs to be known for an accurate system matrix [54]. To obtain this, we simulated a high-count projection of a uniformly filled cylindrical activity volume (radius 10 mm, length 16 mm) that just fits inside the collimator and was assumed to emit  $10^{11}$  gamma photons. This number of photons was not as high as in the real experiment to avoid long computation times, but it was sufficient to derive a proper segmentation. This step was done only once for all simulated collimators because the pinhole position and shielding tube did not change.

### Image reconstruction and evaluation

Reconstructions were performed using the similarity-regulated ordered-subset expectation maximisation (SROSEM) algorithm [53]. The maximum number of subsets was set to 128, and all images were reconstructed on an isotropic 0.05-mm-voxel grid. Scatter and background radiation were corrected using the triple-energy window method [94]. The reconstructed images were post-filtered using a 3D Gaussian filter with FWHM in the range of 0.06 – 0.30 mm with a step size of 0.01 mm. The optimal number of iterations and filter size were defined to be those that maximised the average contrast-to-noise ratio (CNR, calculation explained below). The image reconstruction was validated by comparing an experimental result with a simulation result of the same scan which was a resolution phantom scan with an equivalent activity of 800 MBq/ml  $^{99m}\text{Tc}$  using the tungsten collimator. The evaluation of collimator materials was based on the CNRs as well as visual assessment over the reconstructed rod shapes and minimally resolvable rod sizes on the Derenzo phantom.

CNR was calculated in the same way as in [37]. To this end, regions of interest (ROIs) were used as shown in Figure 2.2(b). Red circles indicate the regions with activity and blue circles indicate the background regions. Each region spans a depth of 0.8 mm (16 slices) around the phantom's centre. We defined the contrast of each of the six rod-sectors as:

$$C_s = \frac{\overline{I}_s - \overline{B}_s}{\overline{I}_s}, \quad (2.3)$$

where  $\overline{I}_s$  is the mean intensity over the activity regions of sector  $s$  ( $I_s$ ) and  $\overline{B}_s$  is the mean intensity over the background regions of sector  $s$  ( $B_s$ ). CNR of each sector was defined as  $C_s/N_s$  where:

$$N_s = \frac{\sqrt{\sigma_{I_{s,p}}^2 + \sigma_{B_{s,p}}^2}}{\overline{I}_s}, \quad (2.4)$$

serving as a measure of variability between ROIs. There,  $\sigma_{I_{s,p}}$  and  $\sigma_{B_{s,p}}$  are standard deviations over  $I_s$  and  $B_s$ , respectively, calculated over all sectors  $s$  and a subset of planes  $p$ , given by  $\{1, 4, 7, 10, 13, 16\}$  to reduce inter-ROI covariance, and  $\overline{I}_s$  is mean intensity over

all ROIs in sector  $s$ . Then the average of the CNRs over the sectors with visible rods was taken for the image quality assessment.

## 2.3 Results

2

### 2.3.1 Pinhole diameters to obtain equal sensitivities for different collimator materials

Table 2.3: The pinhole diameters for different materials that were adjusted to achieve equal sensitivity over the CFOV for each radioisotope. The corresponding system sensitivities are also listed.

Isotope	System sensitivity (over the CFOV)	$d_{ph}$ -U (mm)	$d_{ph}$ -Au (mm)	$d_{ph}$ -W (mm) (fixed)	$d_{ph}$ -Pb (mm)
$^{111}\text{In}$	0.108%	0.232	0.184	0.150	0.054
$^{99m}\text{Tc}$	0.090%	0.174	0.160	0.150	0.126
$^{201}\text{Tl}$	0.044%	0.144	0.130	0.150	0.102
$^{125}\text{I}$	0.050%	0.154	0.152	0.150	0.148

In Table 2.3, pinhole diameters that result in an almost equal sensitivity over the CFOV for different materials and different isotopes are provided. For all cases, the remaining sensitivity differences due to the fact that pinhole diameter was changed in discrete 2  $\mu\text{m}$  steps were small, less than  $10^{-4}\%$ . As expected, Table 2.3 indicates that to obtain “equal” sensitivities, when using a material with higher photon-absorption power larger pinholes are required. Note that 71 keV ( $^{201}\text{Tl}$ ) is close to the K-edge of tungsten where its attenuation coefficient increases suddenly; therefore, it is reasonable that for  $^{201}\text{Tl}$  the tungsten pinholes have larger aperture diameter than the pinholes made of other materials.

### 2.3.2 PSF comparison

The 2D PSFs through a pinhole projecting perpendicular to the detector with diameter as summarised in Table 2.3 are shown in Figure 2.4 while profiles are provided in Figure 2.5. For  $^{111}\text{In}$ , a difference between PSFs for the various collimator materials is visually distinguishable: the PSF is slightly wider when using a material with lower attenuation coefficient. This visual distinction is hard to make for other isotopes having lower energy than  $^{111}\text{In}$ .

Given that the number of photons emitted from the point source is always fixed to be  $4 \cdot 10^{11}$ , the unequal maximal values of the PSFs between different isotopes as indicated in the color bar in Figure 2.4 are due to the fact that the percentage of emitted photons that ends up depositing energy within the photopeak window depends on the energy distribution of the isotope’s emission spectrum. These numbers are also affected by the level of detector’s spatial blurring, which is energy dependent.

The PSFs’ profiles in Figure 2.5 are plotted as a function of the distance from the PSF

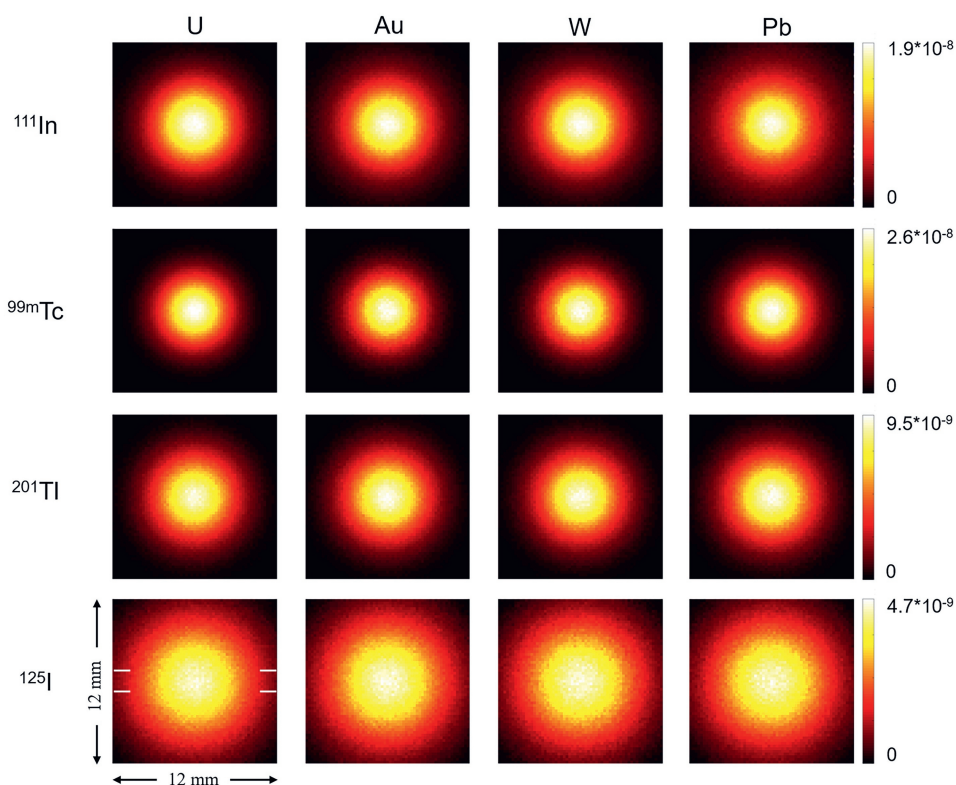


Figure 2.4: 2D PSFs projecting from a point source placed at the collimator's centre through a pinhole oriented perpendicular to one of the detector planes. The PSFs are displayed for different isotopes and pinhole materials, with the pinhole diameters set such that all collimators have equal sensitivity for each isotope (see Table 2.3). The colourmap presents the count density, which represents the number of detected counts on each pixel within the photopeak over the total number of photon emissions.

centre on a semi-logscale, and the corresponding FWHM and FWTM are presented in Figure 2.6. Almost identical profiles and FWHM/FWTM are observed for the different pinhole materials for the low-energy  $^{125}\text{I}$ . A distinction between materials is observable for  $^{201}\text{Tl}$  and  $^{99\text{m}}\text{Tc}$  and more prominent for  $^{111}\text{In}$ . Generally, under the condition of equal sensitivity, the use of materials with higher stopping power yields PSFs with narrower tail and lower values for the FWHM and FWTM.

### 2.3.3 Multi-pinhole reconstruction

A validation of the simulations performed in this work is provided in Figure 2.7. Here tungsten pinholes with an aperture diameter of 0.15 mm were assumed, and the resolution phantom was filled with  $^{99\text{m}}\text{Tc}$ . With an activity concentration of 800 MBq/ml, the minimally visible rods on the phantom have a diameter of 0.15 mm, which is in agreement

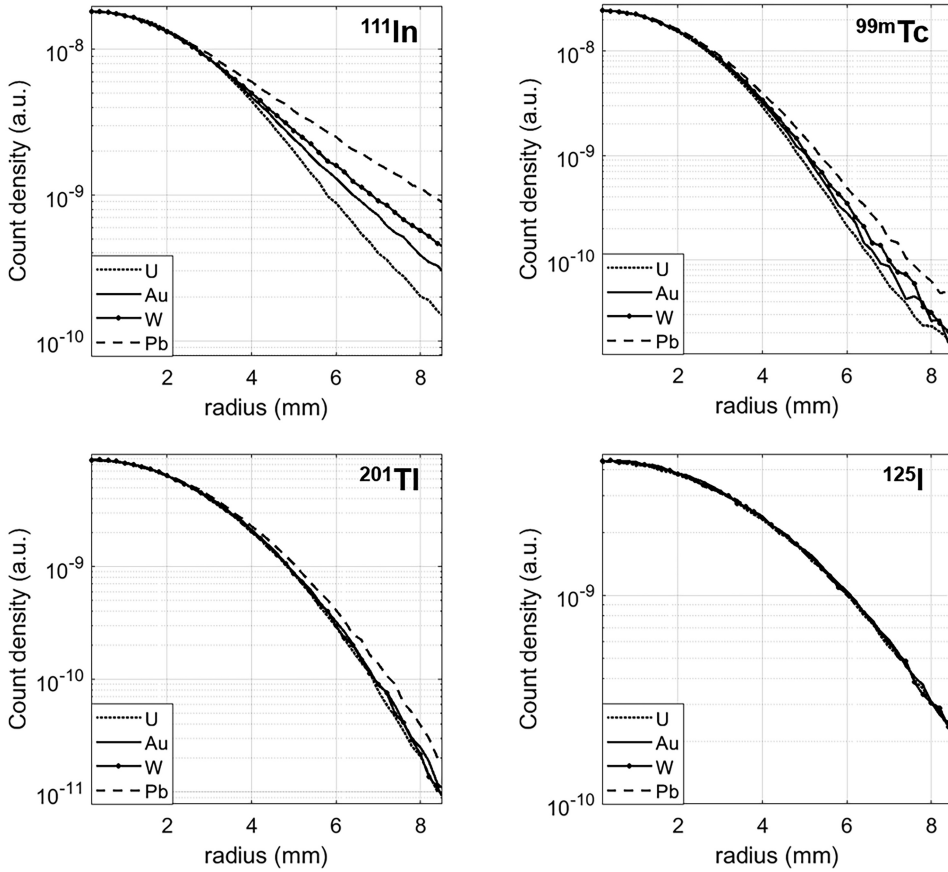


Figure 2.5: PSFs' profiles drawn as indicated on the lower-left PSF in Figure 2.4.

with the experiment in which the phantom was filled with the same amount of activity and scanned in the real tungsten-alloy collimator. Note that the phantom used in the experiment has slightly different rod sectors from the one used in the simulation because it is of interest to check in the simulation the 0.13-mm rods that were not included in the experimental phantom. Figure 2.7 also provides an impression of the achievable resolution with EXIRAD-3D for  $^{99m}\text{Tc}$  for various activity concentrations.

Figures 2.8 to 2.11 show images of the resolution phantom for realistic biological activity concentrations for  $^{111}\text{In}$ ,  $^{99m}\text{Tc}$ ,  $^{201}\text{Tl}$ , and  $^{125}\text{I}$ , respectively. Images are displayed at several iterations, and the square boxes indicate the images with the highest average CNR averaged over the visible rods. Note that the range of the optimal number of iterations varies across isotopes used (across Figures 2.8 to 2.11) and thus different iteration number ranges are shown for different isotopes. The smallest rods that can be resolved have a size of 0.15 mm for  $^{99m}\text{Tc}$ , 0.22 mm for  $^{111}\text{In}$  and  $^{125}\text{I}$ , and 0.26 mm for  $^{201}\text{Tl}$ . Visual assessment indicates

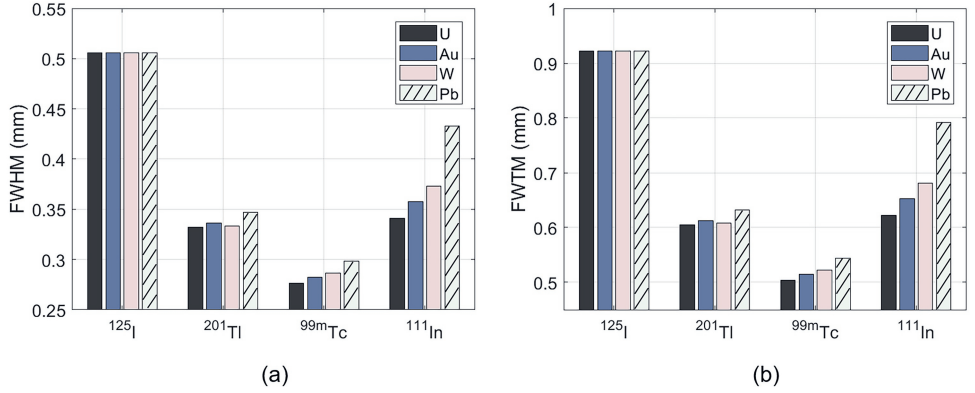


Figure 2.6: FWHM (a) and FWTM (b) of the PSFs in Figure 2.4 representing all studied materials and isotopes.

that uranium and gold perform slightly better than tungsten and lead by offering clearer images, specially for  $^{111}\text{In}$  (see the phantom's background in figure 8). For  $^{125}\text{I}$ , all simulated images appear visually similar, independent of material used.

Figure 2.12 summarises all the optimal average CNRs in Figures 2.8 to 2.11 along with CNR for each visible rod sector. Generally, the CNR is increasing when using a higher-stopping-power material. Compared to lead, the use of materials with higher attenuation coefficient improves the average CNR up to 36.6%, 4.6%, 7.2%, and 1.9% for  $^{111}\text{In}$ ,  $^{99\text{m}}\text{Tc}$ ,  $^{201}\text{Tl}$ , and  $^{125}\text{I}$ , respectively.

## 2.4 Discussion

We have compared the performance of EXIRAD-3D with various pinhole materials regarding resolution at equal system sensitivities. Four pinhole materials, namely lead, tungsten, gold, and depleted uranium, have been investigated for a wide range of photon energies (27 keV – 245 keV). The results show that the pinhole material has an influence on the image resolution when the pinhole diameter is adjusted to keep sensitivity unchanged. Using a material with higher photon stopping power improves image quality, especially for high photon energies. The pinhole material matters for this high-resolution system because with the small pinholes used, the proportion of the number of penetrative and scattered photons compared to the number of photons passing directly through the pinhole can be significant and the material's ability to attenuate photons becomes important. This proportion reduces with the higher-stopping-power material, and thus image quality can be improved. Besides, the chosen pinhole material matters more for the higher energy isotopes as in that case the relative contribution of the pinhole to the PSF is larger; with an average pinhole magnification factor of 19 which we calculated for this geometry (taking into account that the pinholes project onto flat detectors), the detector's contribution to the resolution is about 2.7, 1.6, 1.2, and 0.97 times that of the pinhole for  $^{125}\text{I}$ ,  $^{201}\text{Tl}$ ,  $^{99\text{m}}\text{Tc}$ ,

and  $^{111}\text{In}$ , respectively.

We performed a validation by simulating a scan with 800 MBq/ml  $^{99m}\text{Tc}$  that mimics an experimental scan and achieved comparable images. When assessing images obtained with different pinhole materials, biological activities were assumed because it is of interest to investigate the resolution achievable in realistic animal scans. Therefore,  $^{111}\text{In}$ ,  $^{99m}\text{Tc}$ ,  $^{201}\text{Tl}$ , and  $^{125}\text{I}$  with activity concentrations of 26.3 MBq/ml, 212 MBq/ml, 8.8 MBq/ml, and 185 MBq/ml, respectively, were put in the resolution phantom. With these activities, the smallest rods that the system could resolve have diameters of 0.15 mm for  $^{99m}\text{Tc}$ , 0.22 mm for  $^{111}\text{In}$  and  $^{125}\text{I}$ , and 0.26 mm for  $^{201}\text{Tl}$ . Compared to  $^{99m}\text{Tc}$ , high-energy  $^{111}\text{In}$  results in more undesirable penetration and scatter in the pinhole edges, while low-energy  $^{125}\text{I}$  has the disadvantage of worse detector's spatial and energy resolutions. The resolution obtained with  $^{201}\text{Tl}$  is also degraded as its activity on the phantom was rather low. The achievable image resolutions could be improved when scan time is increased by, for example, scanning over the weekend, which is practical for EXIRAD-3D when long-lived isotopes are used because the tissue sample is cryo-cooled and its shape can be kept unchanged for a long scan.

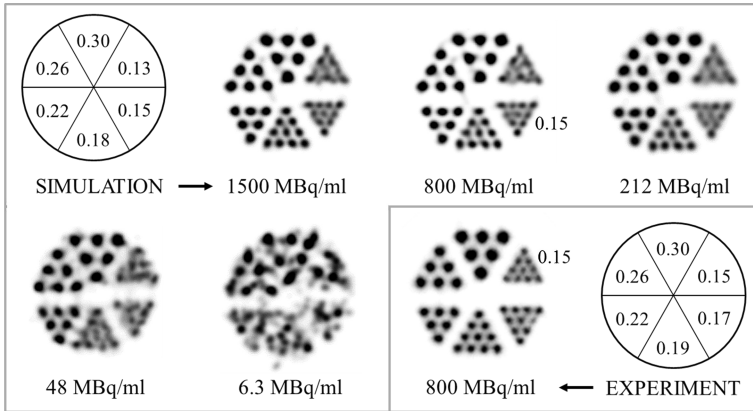


Figure 2.7: Simulated images for the scanner geometry with tungsten pinholes and several activity concentrations of  $^{99m}\text{Tc}$  in the Derenzo phantom compared to an experimental result. The rod diameters are provided in mm. Each image is shown at the optimal iteration and post-reconstruction filter size that maximises the average CNR over the visible rods. Slice thickness was 0.8 mm.

The MCSs in this work are expected to well resemble realistic scans as they considered all important physics processes in SPECT (photoelectric effect, Compton scattering, and Rayleigh scattering for gamma photons, and ionisation, bremsstrahlung, and multiple scattering for electrons) as well as the realistic isotopes' energy distributions, background radiation, and detector response. In this work, MCS was used to mimic most of the imaging procedures, except the matrix interpolation. In principle, a full MCS could also be used to make the matrix by simulating point sources at every voxel, but for this high-resolution system that would take a prohibitively long computation time. Instead, a limited set of point spread functions was simulated, and the rest was obtained by a well-validated interpolation method [54]. This enabled accurate evaluation of pinhole material in micron-resolution

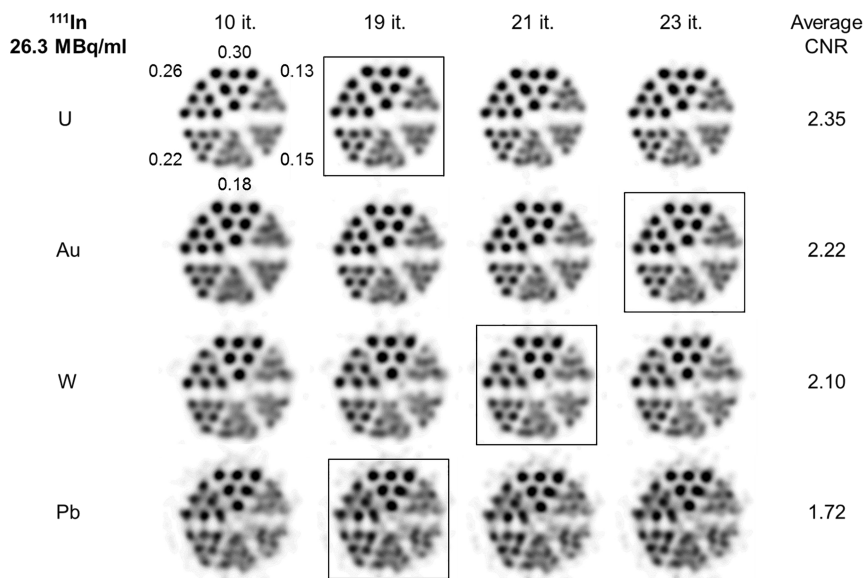


Figure 2.8: Reconstructed images of the Derenzo phantom filled with 26.3 MBq/ml  $^{111}\text{In}$ . For each material used, the image with the highest average CNR is enclosed in a square box and the corresponding CNR is given on the right. Slice thickness is 0.8 mm.

SPECT in a reasonable time.

When choosing the pinhole material, besides the photon attenuation characteristics, the feasibility of using that material should be considered. Depleted uranium is hard to manufacture and not commonly available. In addition, it releases toxic oxide and background radiation. This background radiation can be minimised using small depleted uranium inserts by minimising the amount of uranium needed [70]. We did not include background radiation from the depleted uranium inserts in the simulation because the exact sizes of the inserts were not determined in this work. Gold is expensive, but gold or platinum-gold alloy can be produced at a reasonable expense for small pinhole inserts [10, 21, 60, 71]. Pure tungsten is hard to be cast owing to its high melting point, so tungsten alloys are usually used for easier machining at the cost of slightly decreasing its photon attenuation ability. For example, while pure tungsten has an attenuation coefficient of  $0.952\text{ mm}^{-1}$  at 245 keV, the corresponding value for 92.5% W + 5.25% Ni + 2.25% Fe is  $0.861\text{ mm}^{-1}$  (NIST). According to our simulations (see Supplementary Data), for  $^{111}\text{In}$  imaging this results in only 2.9% reduction in the average SNR which meagrely affects the visual image quality. We expect that this difference is even smaller for lower energies or “purer” tungsten alloys. Lead performs notably worse than the other studied materials (Figure 2.8 and Figure 2.9). Considering those aspects, gold and tungsten are preferred as materials for the pinhole collimator in EXIRAD-3D.

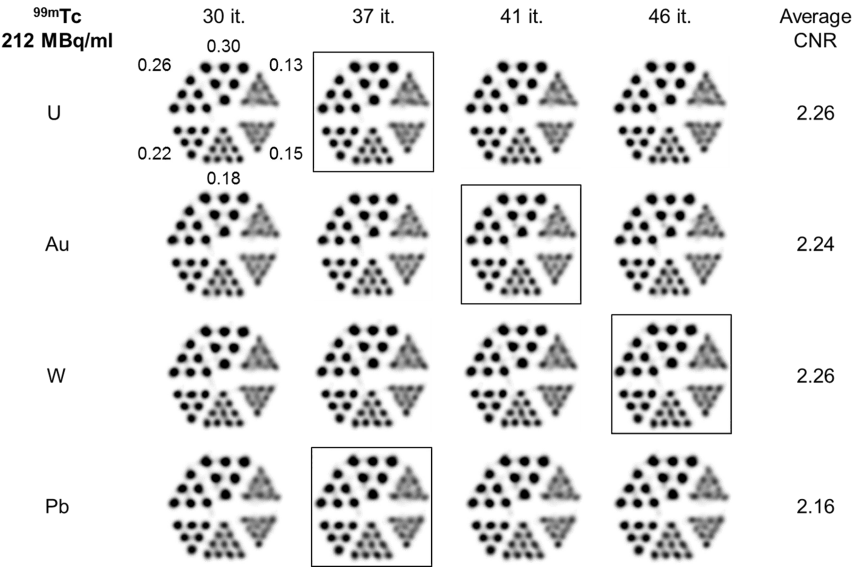


Figure 2.9: Reconstructed images of the Derenzo phantom filled with 212 MBq/ml <sup>99m</sup>Tc. For each material used, the image with the highest average CNR is enclosed in a square box and the corresponding CNR is given on the right. Slice thickness is 0.8 mm.

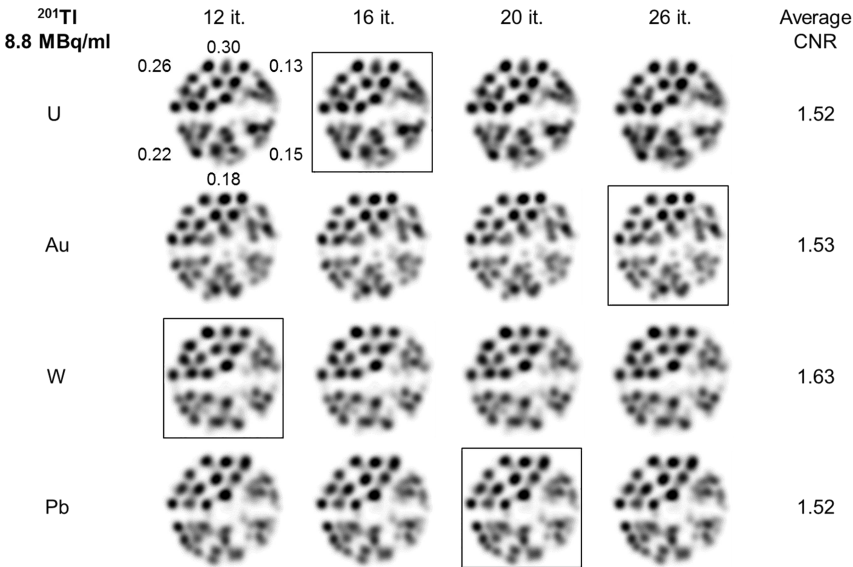


Figure 2.10: Reconstructed images of the Derenzo phantom filled with 8.8 MBq/ml <sup>201</sup>Tl. For each material used, the image with the highest average CNR is enclosed in a square box and the corresponding CNR is given on the right. Slice thickness is 0.8 mm.

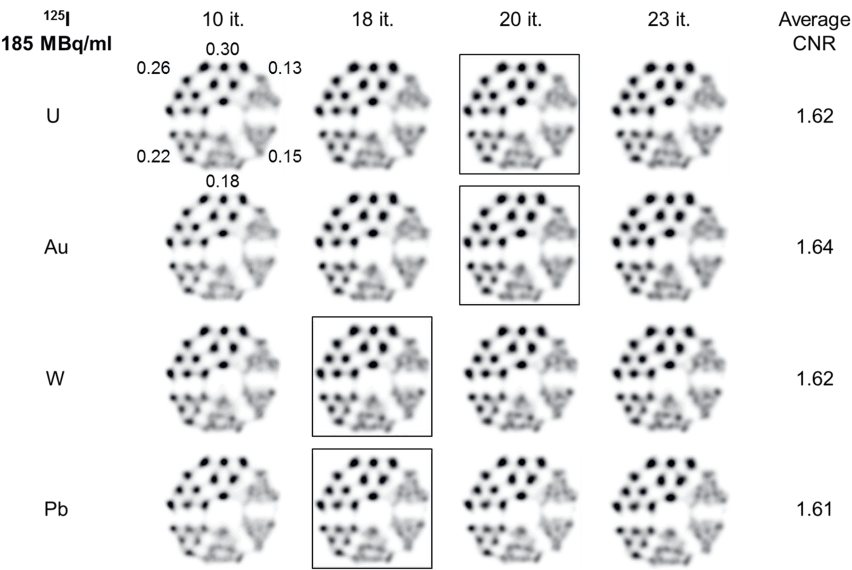


Figure 2.11: Reconstructed images of the Derenzo phantom filled with 185 MBq/ml  $^{125}\text{I}$ . For each material used, the image with the highest average CNR is enclosed in a square box and the corresponding CNR is given on the right. Slice thickness is 0.8 mm.

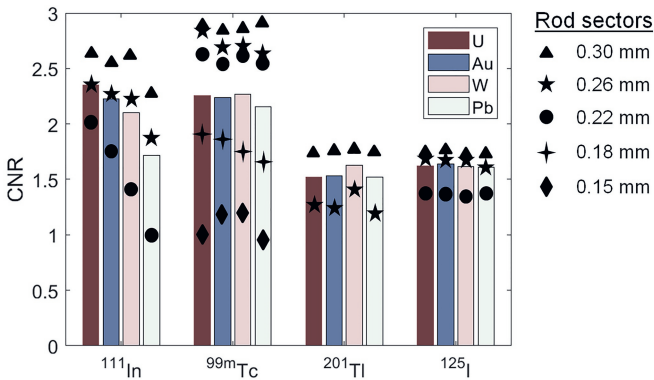


Figure 2.12: Average CNRs of the reconstructed images in Figures 2.8 to 2.11 are summarised with solid bars (for the image with highest average CNR). CNR of each sector with visible rods is also presented by the markers.

## 2.5 Conclusion

The influence of collimator material used in the micron-resolution SPECT system EXIRAD-3D has been studied by comparing resolutions that can be obtained when different pinhole materials are used while keeping sensitivity constant. Results indicate that using materials with higher stopping power yields images with better CNR for the studied isotopes with improvements ranging from 1.9% to 36.6%. Visual assessment of the reconstructed images suggests that for the EXIRAD-3D, the tungsten collimator is generally a good choice for a wide range of SPECT isotopes. For relatively high-energy isotopes such as  $^{111}\text{In}$ , using gold inserts can be beneficial.

## Acknowledgements

The authors would like to thank Ruud Ramakers and Sofia Koustoulidou (MILabs B.V.) for providing the data of the mouse knee joint scan, and the background radiation measurements.

## Appendix

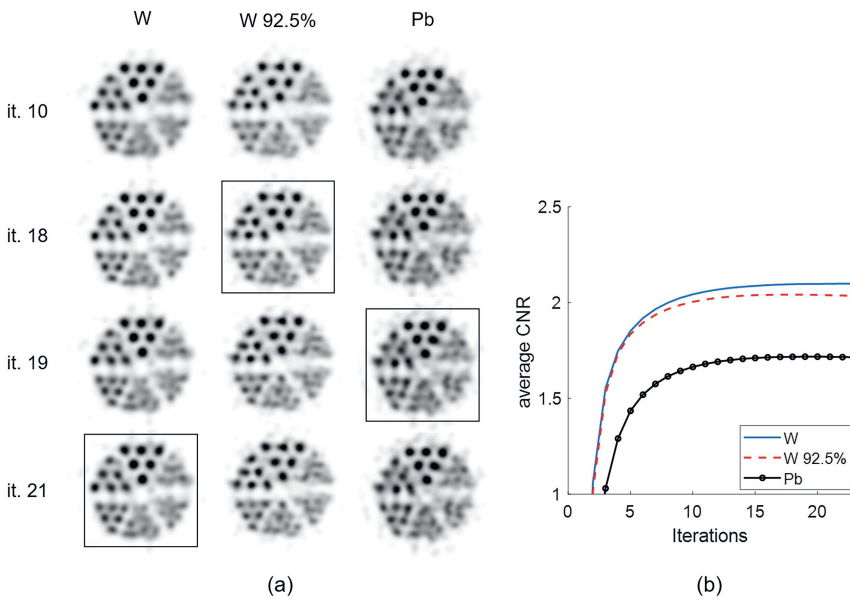


Figure 2.13: Comparison of pure tungsten and pure lead with a tungsten alloy (92.5% W + 5.25% Ni + 2.25% Fe) as the collimator material for  $^{111}\text{In}$  imaging. (a) Reconstructed images of the Derenzo phantom filled with 26.3 MBq/ml  $^{111}\text{In}$ . For each material used, the image with the highest average CNR is enclosed in a square box. Slice thickness is 0.8 mm. (b) The average CNRs plotted as a function of the number of iterations.



## Chapter 3

# EXIRAD-3D: Fast automated three-dimensional autoradiography

3

---

This chapter is adapted from:

**Minh Phuong Nguyen**, Ruud M. Ramakers, Chris Kamphuis, Sofia Koustoulidou, Marlies C. Goorden, and Freek J. Beekman. EXIRAD-3D: Fast automated three-dimensional autoradiography. *Nuclear Medicine and Biology* 86: 59-65, 2020.

Autoradiography is an established technique for high-resolution imaging of radiolabelled molecules in biological tissue slices. Unfortunately, creating a 3D image from a set of these 2D images is extremely time-consuming and error-prone. MicroSPECT systems provide such 3D images but have a low resolution. Here we present EXIRAD-3D, a fast automated method as an alternative for 3D autoradiography from coupes based on ultra-high resolution microSPECT technology. EXIRAD-3D uses a very small bore focusing multi-pinhole collimator mounted in a SPECT system with stationary detectors (U-SPECT/CT, Milabs B.V. The Netherlands) using a sample holder with integrated tissue cooling to avoid activity leaking or tissue deformation during the scan. The system performance was experimentally evaluated using various phantoms and tissue samples of animals *in vivo* injected with technetium-99m and iodine-123. The reconstructed spatial resolution obtained with a Derenzo hot rod phantom was 120  $\mu\text{m}$  (or 1.7 nl). The voxel values of a syringe phantom image appear to be uniform and scale linearly with activity. Uptake in tiny details of the mouse knee joint, thyroid, and kidney could be clearly visualized. EXIRAD-3D opens up the possibility for fast and quantitative 3D imaging of radiolabelled molecules at a resolution far better than *in vivo* microSPECT and saves tremendous amounts of work compared to obtaining 3D data from a set of 2D autoradiographs.

### 3.1 Introduction

Imaging of radiolabeled molecules in biological samples is key in pharmaceutical and biological research, e.g. to locally quantify drug distributions, to study metabolic pathways, or to localize enzymes and nucleic acids in cells. For resolutions below that of what can be achieved by *in vivo* PET and SPECT, these applications mainly rely on 2D autoradiography. Since its debut in the 1950s, autoradiography has gone through an extensive development process but is generally still based on the initial technique of tissue slicing [95, 96]. Recent progress and current practice of autoradiography can be inferred from several review articles [43, 46].

Traditional autoradiography has several limitations to be considered. It requires complex sample preparation and manipulation with sophisticated equipment and dedicated image analysis software. First, the tissue sample needs to be cryo-cooled, and sliced into thin sections using a cryo-microtome. Each section is then meticulously positioned on a phosphor imaging plate or a thin film pre-coated with a photographic emulsion, carefully tagged, and systematically arranged in light-tight and radioactivity-shielded boxes for imaging which typically lasts for days or sometimes even weeks [43]. The obtained 2D images can then be co-registered to form a 3D volume representing the radioactivity distribution within the sample – a process involving intensity correction, slice deformation and alignment by means of e.g. a principal-axes method, cross-correlation computation, and shape analysis [97–99]. The whole procedure is time-consuming and error-prone and potentially causes distortion and other artefacts in the obtained image volume, e.g. due to tears in the slices. Besides, since variability in the thickness of tissue sections and in the thickness of the detection media is often unavoidable, and because in common practice not all sections can be collected due to time limitations, labor and laboratory resources, 3D imaging with

traditional autoradiography is still limited. Additionally, due to the long processing time, traditional autoradiography often utilizes long-lived isotopes (e.g. tritium ( $^3\text{H}$ ), carbon-14 ( $^{14}\text{C}$ ), phosphorus-32 ( $^{32}\text{P}$ ), sulphur-35 ( $^{35}\text{S}$ ), and iodine-125 ( $^{125}\text{I}$ )) but is less suitable for relatively short-lived isotopes (e.g. iodine-123 ( $^{123}\text{I}$ ), technetium-99m ( $^{99\text{m}}\text{Tc}$ ), thallium-201 ( $^{201}\text{Tl}$ ), and indium-111 ( $^{111}\text{In}$ )). It is of interest to investigate if another imaging modality can -at least for a subset of the applications- address these shortcomings and at the same time, also produce high-resolution images.

Alternative techniques have been developed to produce autoradiographs. Beta and Micro-Imagers (commercialized by Biospace Lab, Paris, France), utilizing a parallel plate avalanche chamber or scintillator sheet together with an image intensifier tube and charge-coupled-device (CCD) camera [100], are capable of fast multi-tracer quantitative imaging of radioactivity in tissues at high resolution. CCD technology has also been employed by other groups, either by directly converting particle energy into electric charge or by using scintillators [101–105]. These instruments have the drawback that only relatively few sections can be analyzed at the same time, and they do not directly produce 3D images. Aside from CCDs, various other detector types have been studied and realized as alternatives for traditional autoradiographic films and phosphor imaging plates, such as direct gaseous counters (BeaQuant, Al4R, Nantes, France), pixel array detectors [106–108], complementary metal-oxide-semiconductors [109, 110], DEPFETs [111], silicon strip detectors [112], microchannel plates [113, 114], and position-sensitive avalanche photodiodes [115]. In general, the systems with these detector types are not ready for fully 3D imaging either.

SPECT systems can produce 3D images of many radionuclides. However highest spatial resolution achieved with an *in vivo* preclinical pinhole SPECT modality in mice is now 0.25 mm (or 15.6 nl) [27], and about 0.7 mm in rats. It is extremely hard to push the resolution further due to the animal size which limits the pinhole magnification factor.

Since in *ex vivo* scans of biological tissue, the scanned object is smaller than in *in vivo* scanning, SPECT may reach a much better resolution: the pinholes' centres can be placed much closer to the object to increase both sensitivity and pinhole magnification. At the same time, if the tissue sample is frozen and a relatively long-lived isotope is used, a scan longer than typical *in vivo* SPECT scan times can be performed to acquire many counts. These characteristics together translate into a better image resolution as shown by [116, 117]. This is the reason to investigate if *ex vivo* pinhole SPECT can operate in a resolutions range acceptable to replace at least some autoradiography applications.

For the reasons mentioned above, we developed an option for a SPECT system to enable fast automated 3D autoradiography. This was enabled by the development of a special narrow bore pinhole collimator combined with a cryo-cooled sample holder to keep the tissue frozen during scanning. Relative performance with different pinhole collimator materials has been studied for this system using simulations (Chapter 2 [118]). This work presents the description and experimental performance characterization of the EXIRAD-3D technology using various phantom scans and mouse knee joint, thyroid, and kidney scans.

## 3.2 Methods

### 3.2.1 System and collimator description

The EXIRAD-3D option uses a specially designed focusing multi-pinhole collimator which can be mounted on a U-SPECT/CT or a VECTor/CT imaging system (e.g. [21, 34], MILabs B.V., The Netherlands). The system used in the present paper is equipped with three large-field-of-view gamma-cameras with 9.5 mm thick continuous NaI(Tl) crystals, each read out by 55 photomultiplier tubes. These gamma cameras attain a 3.5 mm intrinsic spatial resolution and 10% energy resolution at an energy of 140 keV. The cylindrical EXIRAD collimator contains 87 round pinholes (pinhole diameter 0.15 mm) with an inner collimator diameter of 21 mm. It is surrounded by a lead shielding tube with trapezium-shaped holes to prevent overlapping between pinhole projections on the detector (Figure 3.1(a)). All pinhole axes converge at a single point in the collimator's centre and together observe a field of view (FOV) with an hourglass shape with a diameter of 21 mm and a length of 13 mm. Note that the FOV can easily be extended several times longitudinally by stepping the object through the collimator with the scanning focus method [119] in which all projection data of the different object's positions are used simultaneously in image reconstruction.

Next to the new collimator, a specialized aluminium sample holder equipped with a cryo-cooling unit (Figure 3.1(b)) was introduced to this system to keep tissue frozen in order to avoid activity leaking or tissue deformation during the scan. The cooling unit has a refillable chamber containing dry ice that maintains cryogenic temperature at the sample. Additionally, the robotic arm attached to the sample holder was improved for precise tissue placement inside the scanner during the scan and for accurate point source measurements for system calibration to guarantee the micro-scale image resolution.

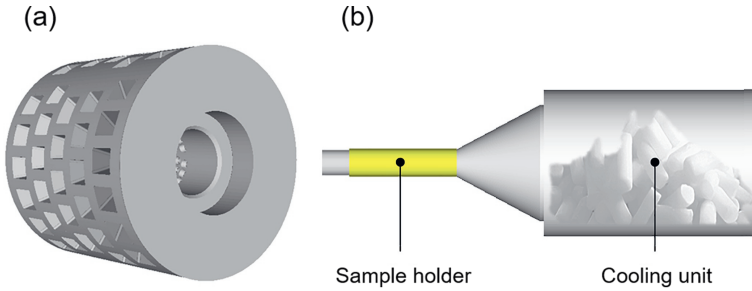


Figure 3.1: (a) The focusing multi-knife-edge-pinhole collimator surrounded by the shielding tube with trapezium-shaped holes. (b) The cylindrical sample holder equipped with a cooling unit containing dry ice.

### 3.2.2 Image reconstruction and processing

Calibration of EXIRAD-3D was done using a set of 435  $^{99m}\text{Tc}$  point source measurements, from which a full system matrix was generated using a model-based interpolation method

[54] which is commonly used to generate system matrices for all SPECT collimators used on the U-SPECT/CT systems. For these measurements, a tiny point source is desirable (ideally a point); however, it is challenging to contain a large amount of radioactivity in a small volume. For the high-resolution EXIRAD-3D, we fabricated a 100- $\mu\text{m}$ -diameter spherical point source, and were able to condense a 80 MBq activity of  $^{99m}\text{Tc}$  in this source.

List-mode projection data were acquired for all scans with a  $\pm 12.5\%$  photopeak window centred at either 140 keV for  $^{99m}\text{Tc}$  or 159 keV for  $^{123}\text{I}$ . A similarity-regulated ordered-subset expectation maximisation algorithm [53] with a maximum of 128 subsets was used for image reconstruction, except for the mouse knee joint scan where a pixel-based ordered-subset expectation maximisation algorithm [52] with four subsets was used. Images were reconstructed on a 0.05 mm voxel grid using 20 iterations. Scatter and background radiation were corrected for using a triple-energy window method [94]. To this end, two side windows having a width of 20% of the photopeak window's width were placed adjacent to the photopeak. Gaussian and/or median post-filtering was applied to the reconstructed images with the filter size optimized manually for each scan (indicated below). The images in the Results section were displayed with a slice thickness of 0.2 mm except for the mouse knee joint scan where the slice thickness was 0.05 mm.

### 3.2.3 Experiments

The performance of EXIRAD-3D was characterized by scanning a Derenzo phantom to measure the system's resolution, a syringe phantom to show the system's uniformity and linearity, and several mouse tissues to illustrate which anatomical detail can be seen. The mouse experiments were performed with C57BL/6 mice under protocols approved by the Animal Research Committee at UMC Utrecht and in accordance with the Dutch Law on Animal Experimentation. The dissected tissue was snap-frozen in liquid nitrogen (except for the mouse knee joint) and subsequently placed inside the aluminium holder filled with Tissue-Tek OCT compound (Sakura Finetek Europe, cat. no. 4583) and attached to the cooler to keep the tissue frozen for the whole scan duration. Activity levels prior to the scans were measured using a dose calibrator (VDC-304, Veenstra Instruments, the Netherlands).

#### Phantom studies

System sensitivity was measured with a  $^{99m}\text{Tc}$  point source placed at the collimator's centre to calculate the ratio of the count rate (cps) within the acquisition window and the point source's activity (MBq).

System resolution was evaluated by scanning a Derenzo phantom having hot rods arranged in six sectors with rod diameters of 0.17, 0.16, 0.15, 0.14, 0.13, and 0.12 mm and a length of 1.5 mm. In each sector of this phantom, the distance between the centres of two adjacent rods is twice the rods' diameter. The resolution was defined as the diameter of the smallest rods that can be visually distinguished in the reconstructed image. The Derenzo phantom was filled

with 4.06 MBq  $^{99m}\text{Tc}$ -pertechnetate and scanned for 3 hours. Images were reconstructed with 100% and 20% of the counts from the list-mode data to emulate the image resolution with the same scan time but with 100% and 20% of the initial radioactivity, respectively. A post-reconstruction 3D Gaussian filter having the full-width-at-half-maximum (FWHM) of 0.12 mm and 0.14 mm was applied on the 100%- and 20%-activity images, respectively.

The uniformity of the reconstructed images was assessed with a cylindrical phantom (inner diameter 8.5 mm, inner length 9.5 mm) filled with 38.6 MBq  $^{99m}\text{Tc}$ -pertechnetate and scanned for 3 hours. Images were reconstructed with 100%, 50%, and 20% of counts from the list-mode data to emulate the image uniformity with the same scan time but with 100%, 50%, and 20% of the initial radioactivity, respectively. A post-reconstruction 3D Gaussian filter having the FWHM of 0.6 mm was applied. To calculate the uniformity, nine regions of interest (ROIs), each formed by a circular disk with 3-mm radius and 0.3-mm thickness, were evenly placed on the image at 0.45-mm intervals. The uniformity was calculated as the ratio of the standard deviation between the ROIs' means to the average values from the ROIs, and represented as percentage.

Relative quantification was investigated with the same uniform phantom to see if the reconstructed image intensity changes linearly with activity.

### Mouse knee joint scan

A mouse was anaesthetized with isoflurane and injected intravenously via the tail vein with 550 MBq technetium-99m methylene diphosphonate ( $^{99m}\text{Tc}$ ]MDP). Five hours post-injection, the mouse was euthanized and one of its limbs was excised and measured to contain 6 MBq activity at the start of the scan. The acquisition lasted for 7 hours with 60-minute time frames, focusing on the knee joint. The reconstructed SPECT image was post-filtered with a 0.1-mm-FWHM 3D Gaussian kernel. The knee joint was subsequently scanned in the CT module with a 4  $\mu\text{m}$  resolution setting.

### Mouse thyroid scan

A second mouse was anaesthetized with isoflurane and injected intravenously via the tail vein with 10.25 MBq [ $^{123}\text{I}$ ]NaI. Four hours post-injection, the mouse was euthanized and a tissue volume containing the thyroid and a part of the trachea was excised and frozen as described above. The tissue was scanned for 11 hours with 15 minute time frames. A 0.15-mm-FWHM 3D Gaussian filter followed by a 3\*3\*3 median filter was applied to the reconstructed image.

### Mouse kidney scan

A third mouse was injected intravenously via the tail vein with 75 MBq technetium-99m dimercaptosuccinic acid ( $^{99m}\text{Tc}$ ]DMSA). Three hours post-injection, the mouse was euthanized and one of its kidneys was excised and frozen as described above. The kidney

was scanned for 11 hours with 15 minute time frames. A 0.28-mm-FWHM 3D Gaussian filter was applied to the reconstructed image.

### 3.3 Results

#### 3.3.1 Phantom studies

3

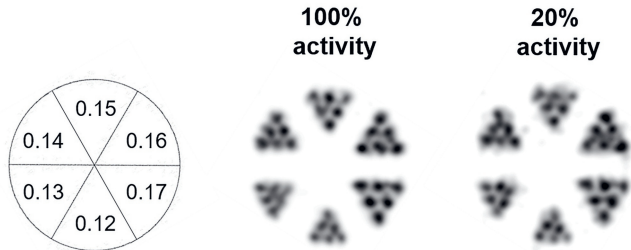


Figure 3.2: Derenzo phantom scan with 4.06 MBq  $^{99m}\text{Tc}$ -pertechnetate at the start and a scan time of 3 hours. The images were reconstructed with 100% and 20% of the counts to emulate scans with the same scan time but with 100% and 20% of the initial activity. The rod diameters are provided in mm. Slice thickness was 0.2 mm.

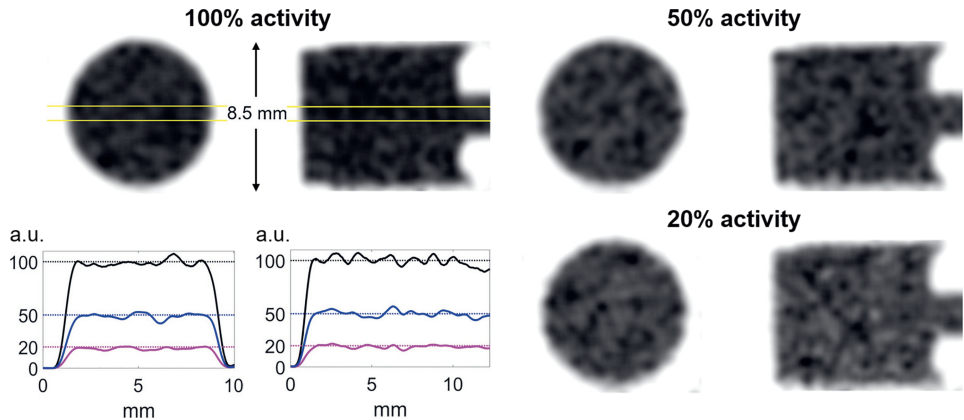


Figure 3.3: Uniform phantom scan with 38.6 MBq  $^{99m}\text{Tc}$ -pertechnetate at the start and a scan time of 3 hours. The images were reconstructed with 100%, 50%, and 20% of the counts to emulate scans with the same scan time but with 100%, 50%, and 20% of the initial activity. For each reconstructed image, two perpendicular slices with a thickness of 0.2 mm are shown with gray scales in which white represents zero activity and black represents the maximum activity. Line profiles are also drawn at the position indicated with yellow lines on each slice. Here, the profiles are scaled by the same factor such that the average intensity within the phantom on the image reconstructed with 100% counts is 100.

The system sensitivity for  $^{99m}\text{Tc}$  was determined to be 800 cps/MBq (or 0.08%) at the collimator's centre. Figure 3.2 shows an image of the Derenzo phantom reconstructed with two activity levels to test EXIRAD's spatial resolution. All rods in this phantom are discernable

on the reconstructed images for both 100% and 20% of the activity, demonstrating a spatial resolution  $<120$  microns (or 1.7 nl). This is about a ten times better volumetric resolution than that of state-of-the-art preclinical *in vivo* SPECT (250 microns, or 15.6 nl) [27].

Figure 3.3 presents 0.2 mm thick slices of the uniform phantom images reconstructed with three activity levels and line profiles extracted from these slices at the positions indicated with yellow lines. The uniformity was 1.31%, 2.33%, and 3.01% for 100%, 50%, and 20% activity, respectively. The line profiles show that the reconstructed image intensity changes linearly as the activity varies, which shows the relative quantification result with this scanner.

3

### 3.3.2 Mouse knee joint scan

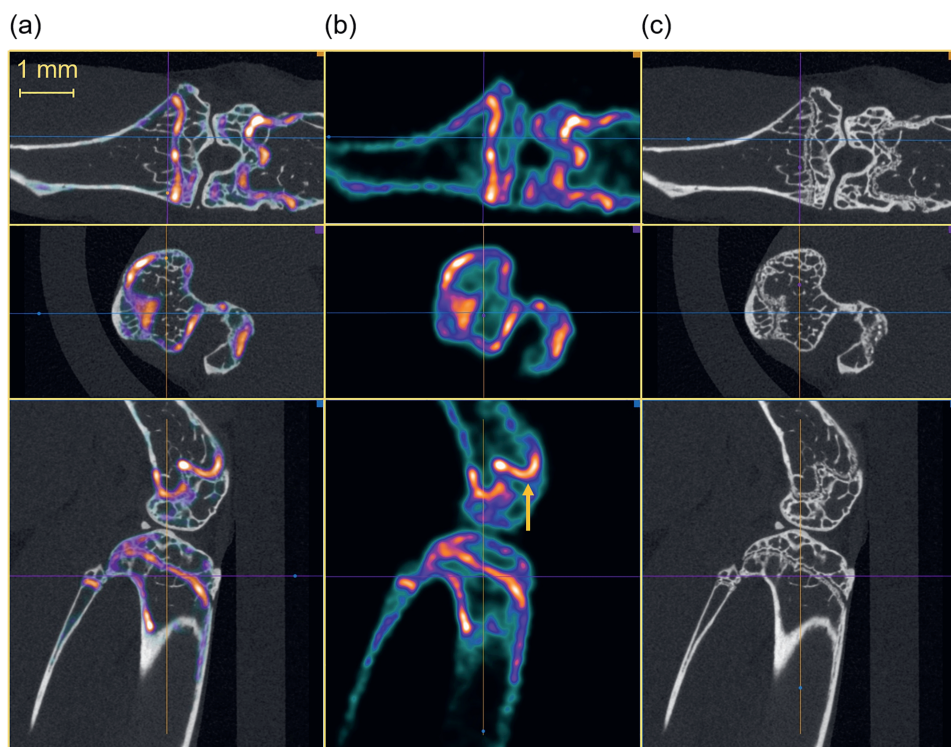


Figure 3.4: (a) EXIRAD-3D SPECT images of  $[^{99m}\text{Tc}]\text{MDP}$  distribution in a mouse knee joint fused with CT. (b) Only the  $[^{99m}\text{Tc}]\text{MDP}$  SPECT images. The knee joint was measured to contain 6 MBq activity at the start, and the scan lasted for 7 hours. Slice thickness was 0.05 mm. The arrow points at the activity distribution near the epicondylus lateralis of the knee joint. (c) Only the CT images obtained with the CT module on the same system and with a 4  $\mu\text{m}$  resolution setting.

$[^{99m}\text{Tc}]\text{MDP}$  labels sites of active bone turnover – the continuing process of bone resorption and formation taking place at a low physiological level. Figure 3.4 shows three cross-

sections of EXIRAD-3D SPECT and CT as well as the fused SPECT/CT through the mouse knee joint with [ $^{99m}\text{Tc}$ ]MDP. Tiny details of bone turnover on many structures in the knee joint are visualized on the SPECT image, and the fused SPECT/CT image shows an excellent correlation of the [ $^{99m}\text{Tc}$ ]MDP distribution to the anatomical microstructures on the CT image. Compared to *in vivo* bone knee scans with state-of-the-art 250-micron-resolution *in vivo* SPECT [27], much more detail was visible with EXIRAD-3D. For example, the tiny activity distribution near the epicondylus lateralis of the knee joint (see the arrow in Figure 3.4) is clearly visualized with EXIRAD-3D while it is much more blurred with *in vivo* SPECT.

### 3.3.3 Mouse thyroid scan

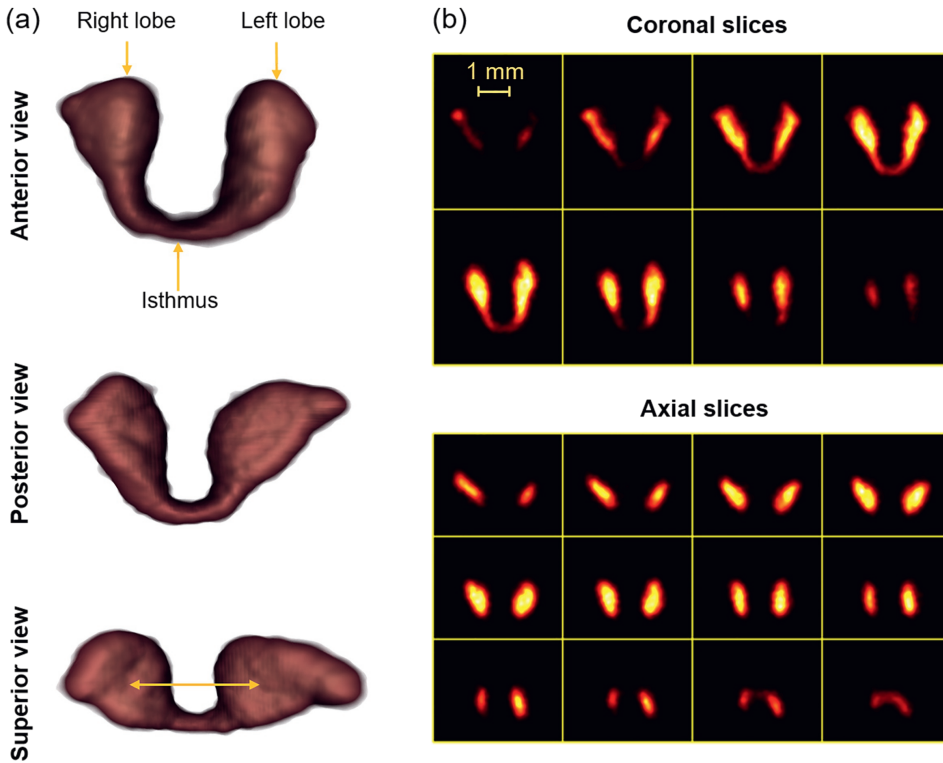


Figure 3.5: [ $^{123}\text{I}$ ]NaI scan of the mouse thyroid with 10.25 MBq activity injected intravenously and a scan time of 11 hours. (a) 3D anterior, posterior, and superior views of the reconstructed thyroid. (b) Selected coronal and axial slices through the thyroid. Slice thickness was 0.2 mm.

Figure 3.5(a) presents 3D views of the thyroid gland imaged using [ $^{123}\text{I}$ ]NaI, and Figure 3.5(b) shows coronal and axial slices through the thyroid. The two thyroid lobes are nicely visualized including the thin isthmus (also having iodine uptake) connecting the two lobes inferiorly and medially. As measured on the reconstructed image, each lobe is

approximately 2.5 mm long, 1.3 mm wide, and 0.6 mm deep, and the isthmus is about 0.3 mm thin. The indents seen on the medial aspect of the two lobes as indicated in Figure 3.5(a) (superior view) are corresponding to the thyroid part that wraps around the trachea near the base of the laryngeal cartilages. These anatomical details of the thyroid gland are in good agreement with the mouse atlas in [120].

### 3.3.4 Mouse kidney scan

3

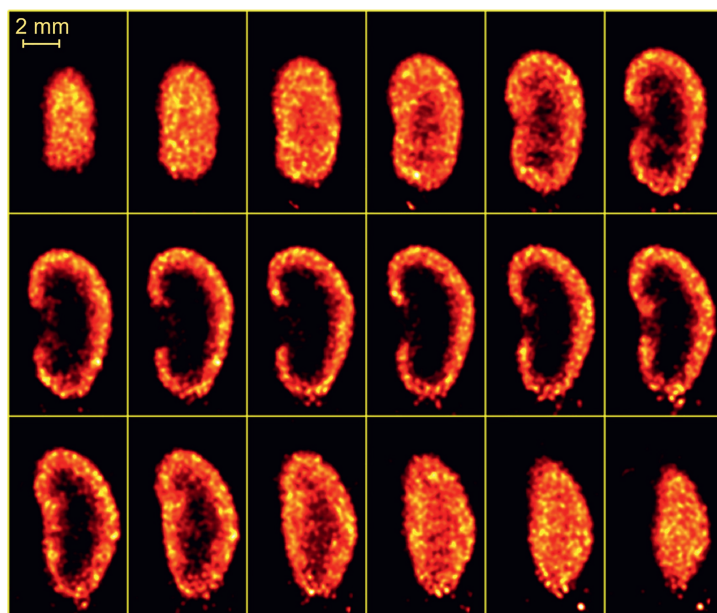


Figure 3.6:  $[^{99m}\text{Tc}]\text{DMSA}$  scan of the mouse kidney with 75 MBq activity injected intravenously and a scan time of 11 hours. Slice thickness was 0.2 mm.

Figure 3.6 shows slices through the  $[^{99m}\text{Tc}]\text{DMSA}$  kidney image obtained *ex vivo* using EXIRAD-3D. As anticipated, the  $[^{99m}\text{Tc}]\text{DMSA}$  tracer distribution is revealed in the renal cortex but not in the medullar cavity. Some structures on the renal cortex (higher-uptake areas), which are believed to be corresponding to the parts of nephrons, are also visualized. The small amount of activity seen outside the kidney at the bottom of the image is probably because of the tissue handling process in which activity on the tools may end up in the Tissue-Tek compound when placing the sample into the holder.

## 3.4 Discussion

We presented a fast automated three-dimensional autoradiography technique capable of imaging radiolabeled molecule distributions in tissue samples at a resolution of 120  $\mu\text{m}$ . This

technique is enabled using a specialized focusing multi-pinhole collimator mounted on a U-SPECT/CT system and a built-in cryo-cooling unit. Because of the close distance between the pinholes and the tissue volume and large pinhole magnification factors, high-resolution 3D images can be obtained. Furthermore, as described in the Methods section, EXIRAD-3D has some other significant adaptations compared to U-SPECT/CT which together translate into substantial improvement in image quality: (i) a novel specialized cryo-cooling unit to keep tissue frozen during the scan that has not been used in any prior preclinical SPECT system, (ii) a more precise robotic arm for accurate tissue and point source placement, and (iii) a considerable effort invested in system calibration to address the challenge posed by the small point source size.

With EXIRAD-3D, the imaging volume can be easily adjusted using a patented acquisition interface and a highly focused scan is accomplishable [119]. Since a more focused scan means that more counts can be acquired from the volume of interest in a given time that benefits the image quality, we recommend using EXIRAD-3D in the highest possible focusing mode. In other words, the selected scan volume should be set just large enough to cover the tissue sample. The system resolution can be possibly improved for higher-energy isotopes by employing pinhole inserts made of a material with higher photon-stopping power than tungsten such as gold or gold-platinum alloy, as previously studied in Chapter 2 [118]. In addition, extending the scan time could enhance the image quality even further, provided of course that the isotope's half-life is sufficiently long. This is practical as in such long scans, the tissue is kept frozen to immobilize the activity distribution, and thus scans can be done overnight without an operator present.

In this work, we have presented quantitative results showing that the reconstructed activity scales linearly with the real activity on the phantom. In order to obtain absolute quantification (i.e. the activity concentration in terms of MBq/ml) the method presented in [121] can be applied for *ex vivo* scans in the same way as for *in vivo* scans with our systems. In this case, the reconstructed image is simply scaled by a calibration coefficient defined as the ratio of the activity concentration to the voxel value in reconstructed images, which is obtained by scanning a point source with known activity of a studied isotope and then applying it to all scans done with that isotope and the same system settings.

Despite the listed limitations of traditional autoradiography, it is currently still common practice when a very high resolution at the cellular level is desired. Besides, traditional autoradiography can also image pure alpha- and beta-emitters while this is not an option with the current EXIRAD-3D that is only designed for imaging gamma-emitters. However, EXIRAD-3D (with 1.7 nl volumetric resolution) has reached the resolution range of autoradiography (from 0.01 pl to several nl, [47]), and it can, for a subset of these studies, be a good alternative for traditional autoradiography, in particular as an option on a U-SPECT/CT or a VECTor/CT imaging system that facilitates longitudinal studies on the same animal, and provides a direct link between *in vivo* and *ex vivo* datasets. The increase in resolution and user convenience are achieved with little additional effort instead of going through the complicated tissue sectioning process with completely different autoradiography laboratory equipment. With EXIRAD-3D, the only additions to the common *in vivo* workflow are dissection of the organs and snap-freezing them. The latter takes less than ten minutes for

e.g. the thyroid. The complexity of tissue dissection depends on the studied tissue, but it is much less labour intensive than performing traditional autoradiography in 3D.

## 3.5 Conclusion

This chapter characterized the performance of EXIRAD-3D as a new technique for autoradiography. Phantom scans demonstrated 120  $\mu\text{m}$  spatial resolution, and *ex vivo* mouse tissue scans visualized tiny details of the mouse knee joint, thyroid, and kidney. The acquired 3D autoradiographs can be perfectly overlaid with ultra-high resolution CT images and directly linked to the *in vivo* results obtained in a multi-modal acquisition with the same platform, e.g. after a longitudinal imaging study.

## Chapter 4

# Efficient Monte-Carlo based system modelling for image reconstruction in preclinical pinhole SPECT

4

---

This chapter is adapted from:

**Minh Phuong Nguyen**, Marlies C. Goorden, Ruud M. Ramakers, and Freek J. Beekman. Efficient Monte-Carlo based system modelling for image reconstruction in preclinical pinhole SPECT. *Physics in Medicine & Biology* (accepted, <https://doi.org/10.1088/1361-6560/ac0682>).

The use of multi-pinhole collimation has enabled ultra-high-resolution imaging of SPECT and PET tracers in small animals. Key for obtaining high-quality images is the use of statistical iterative image reconstruction with accurate energy-dependent photon transport modelling through collimator and detector. This can be incorporated in a system matrix that contains the probabilities that a photon emitted from a certain voxel is detected at a specific detector pixel. Here we introduce a Fast Monte-Carlo based (FMC-based) matrix generation method for pinhole imaging that is easy to apply to various radionuclides. The method is based on accelerated point-source simulations combined with model-based interpolation to straightforwardly change or combine photon energies of the radionuclide of interest. The proposed method was evaluated for a VECTor PET-SPECT system with (i) a HE-UHR-M collimator and (ii) an EXIRAD-3D 3D autoradiography collimator. Both experimental scans with  $^{99m}\text{Tc}$ ,  $^{111}\text{In}$ , and  $^{123}\text{I}$ , and simulated scans with  $^{67}\text{Ga}$  and  $^{90}\text{Y}$  were performed for evaluation. FMC was compared with two currently used approaches, one based on a set of point-source measurements with  $^{99m}\text{Tc}$  (dubbed traditional method), and the other based on an energy-dependent ray-tracing simulation (ray-tracing method). The reconstruction results show better image quality when using FMC-based matrices than when applying the traditional or ray-tracing matrices in various cases. FMC-based matrices generalise better than the traditional matrices when imaging radionuclides with energies deviating too much from the energy used in the calibration and are computationally more efficient for very-high-resolution imaging than the ray-tracing matrices. In addition, FMC has the advantage of easily combining energies in a single matrix which is relevant when imaging radionuclides with multiple photopeak energies (e.g.  $^{67}\text{Ga}$  and  $^{111}\text{In}$ ) or with a continuous energy spectrum (e.g.  $^{90}\text{Y}$ ). To conclude, FMC is an efficient, accurate, and versatile tool for creating system matrices for ultra-high-resolution pinhole SPECT.

## 4.1 Introduction

Statistical iterative image reconstruction is prominently used in SPECT and PET [122, 123]. To obtain high-quality images, accurate knowledge of the energy-dependent photon transport through the collimator and in the detector is required. This is usually captured in the point spread functions (PSF), the scanner's response to a point source. PSFs for all voxels in the field of view (FOV) together can be combined in the so-called system matrix, with matrix elements corresponding to the probability that a photon emitted from a certain voxel is detected in a certain detector pixel. For well representing these probabilities, the PSFs need to be noiseless.

Several methods to obtain the system matrix for pinhole SPECT are in use. They can be grouped into three main categories. The first approach is based on analytical modelling of the scanner with some pre-determined geometrical information obtained from a calibration measurement [124–126]. This method requires a very precise calibration, especially for high-resolution pinhole systems because such systems are susceptible to small parameter variations. The second approach to obtain the system matrix is by directly measuring the PSFs from a tiny radioactive source sequentially placed at many voxel locations. This approach provides accurate system matrices as the measurement accounts for all realistic

system geometries and physics processes within the scanner. Some researchers proposed to measure a point source at each of the voxels in the FOV [16, 20, 127]. However, with the dramatic resolution increase of recent pinhole SPECT systems, the massive number of required measurements often makes this approach infeasible. A practical way is to measure only a small number of PSFs, and then interpolate to estimate the missing PSFs [54, 128]. This is time-efficient and has been used in preclinical pinhole SPECT systems to produce both highly quantitative [121] and high-resolution images, currently with resolutions down to 0.12 mm (Chapter 3 [129]). The third approach is to perform Monte Carlo simulation (MCS) to obtain a full system matrix as proposed in [126, 130, 131]. This approach can accurately account for all kinds of physics processes, without the need for extensive measurements assuming that the geometry is exactly known. The drawback is that MCS is computationally demanding; therefore, it is time-consuming and may even be infeasible to obtain noiseless PSFs for very-high-resolution pinhole SPECT.

For pinhole scanners in our labs, U-SPECT [17, 21] and VECTOR [34], we usually start with a calibration measurement using a  $^{99m}\text{Tc}$  (140 keV) point source placed at a few hundred positions within the FOV to obtain a set of PSFs. Then, a system matrix is traditionally generated by a PSF fitting and an interpolation procedure as described in [54]. In this method, the measured point source ideally needs to be smaller than the image voxel, meaning that for very-high-resolution systems like EXIRAD-3D (voxel size 50  $\mu\text{m}$ ), it is challenging to fabricate such a tiny point source still containing a sufficiently high activity. Besides, such a matrix generated from  $^{99m}\text{Tc}$  point-source measurements describes photon transport at 140 keV emission energy. It can also be used to reconstruct other radionuclides emitting photons with energies in close proximity to 140 keV such as  $^{123}\text{I}$  (159 keV), but it is sub-optimal to be used in reconstructing radionuclides emitting photons with very different energies. In principle, one could envisage using a separate point-source calibration for each radionuclide, but this is costly and time-consuming if many radionuclides are to be used with the scanner. Additionally, for radionuclides that have a short half-life or radionuclides that are difficult to be produced with a sufficiently high activity condensed in the point source, it is very challenging to obtain noiseless PSFs in the calibration measurement.

In our labs, we also developed a ray-tracing matrix generation method that can easily adapt the matrix energy for different radionuclides. It uses the same  $^{99m}\text{Tc}$  point-source calibration for geometrical information and then calculates photon transport for every emission-to-detection path through the collimator and detector material. The input collimator can be modelled with either an analytical description or a voxelised volume. The latter is often used because it can represent complex collimator geometries. The ray-tracing matrix is specifically used for positron emitters and other high-energy radionuclides, and it can also be used for low-energy radionuclides. However, the ray-tracing calculation can be too computationally expensive for ultra-high-resolution systems with complex-geometry collimators such as EXIRAD-3D. It is because, for such a system, this calculation currently requires a voxelised volume to represent the collimator accurately, and both the collimator's voxel size and the reconstructed image's voxel size need to be very small, which increase the matrix generation time. Moreover, multiple ray-tracing matrices at different energies are required for optimal imaging of radionuclides that emit complex energy spectra, such as  $^{67}\text{Ga}$  with multiple photopeak energies or  $^{90}\text{Y}$  with a wide continuous energy spectrum.

This is time demanding both when generating the matrix and for image reconstruction.

Here we present an efficient and accurate FMC-based matrix generation method to address the challenges mentioned above. From the same calibration measurement used for existing matrix generation methods, a fast MCS (FMCS) was performed to obtain a set of PSFs for the targeted radionuclide, and the same interpolation method as in [54] was applied to generate a full system matrix. This way, realistic physics processes are included inside the matrix, and matrices for other radionuclides than the one used in the calibration measurement ( $^{99m}\text{Tc}$ ) can be easily generated. The FMC-based method can also combine information from multiple energies in a single matrix to save time in both matrix generation and image reconstruction. We validate the proposed FMC-based matrix with both experiments and simulation studies with  $^{99m}\text{Tc}$ ,  $^{111}\text{In}$ ,  $^{123}\text{I}$ ,  $^{67}\text{Ga}$ , and  $^{90}\text{Y}$ .

## 4

### 4.2 Methods

#### 4.2.1 Studied systems and multi-pinhole collimators

The studies in this work were performed on a VECTor imaging system, commercially available via MILabs B.V., Utrecht, the Netherlands. Two collimators were used, a HE-UHR-M collimator for simultaneous *in vivo* SPECT/PET imaging of mice with submillimeter resolutions down to 0.6 mm for  $^{18}\text{F}$  and 0.4 mm for  $^{99m}\text{Tc}$  [34, 42], and an EXIRAD-3D collimator for *ex vivo* SPECT imaging of tissue samples with a resolution of 120  $\mu\text{m}$  for  $^{99m}\text{Tc}$  [118, 129]. The system uses a triangular detector setup with three large-field-of-view gamma-cameras, each equipped with a 9.5 mm thick NaI(Tl) crystal and read out by 55 photomultiplier tubes.

The HE-UHR-M collimator uses clustered-pinhole technology [33, 34] that effectively collimates high-energy photons without compromising the collimator's FOV. It contains 162 pinholes with a diameter of 0.7 mm and narrow opening angles of 16-18° that are grouped in clusters of four. The pinholes are placed in such a way that pinhole projection overlapping on the detector is minimised, and there is no pinhole shielding applied outside the collimator.

The EXIRAD-3D collimator has a large pinhole magnification factor that enables high-resolution *ex vivo* imaging of small tissue samples such as a mouse kidney or a mouse thyroid. It contains 87 pinholes with a diameter of 0.15 mm and an opening angle of 26°. A trapezium-hole lead shielding tube is attached outside the collimator's core to prevent pinhole projection overlapping.

#### 4.2.2 Monte Carlo simulations

Monte Carlo simulations were used to generate sets of PSFs from which FMC-based system matrices were generated (see Section 4.2.3. They were also used for simulated scans in this work (Section 4.2.4) when corresponding experiments were not performed.

Geant4 Application for Tomographic Emission (GATE) [76, 77] version 8.0 was used on a CentOS 6.6 cluster with 250 processors for the MCS in this work. System geometries consisting of three NaI(Tl) scintillators and a multi-pinhole collimator were both pre-created as STL files in MATLAB R2018b (MathWorks, Natick, MA, USA) where any geometry calibration information arriving from the real system was already applied before importing it into GATE. This is much easier than applying the calibration information inside GATE. All the scanned phantoms in GATE were created using analytical shapes. Physics processes were defined using the “emstandard” physics list builder as explained in the GATE documentation. The radioactive sources ( $^{67}\text{Ga}$ ,  $^{99m}\text{Tc}$ ,  $^{111}\text{In}$ ,  $^{123}\text{I}$ ) were created with discrete energy spectra retrieved from [80]. This allows the simulation to include the full radionuclides’ emission energy spectra while still being time-efficient as the spectra were pre-defined. Only for  $^{90}\text{Y}$ , the “fastY90” source (officially released with GATE version 8.0) was used. This source generates photons directly from a pre-calculated bremsstrahlung kernel, rather than simulating the full electron transport of the emitted beta particle, to speed up the simulation. Furthermore, a threshold of 105 keV was set to exclude lower-energy bremsstrahlung photons that are often not used in  $^{90}\text{Y}$  imaging [132, 133]. The detector’s energy resolution and spatial resolution were modelled in the same way as in Chapter 2 [118].

### 4.2.3 Monte-Carlo based system modelling

The FMC-based system modelling started with a calibration step followed by an FMC-based point-source simulation to obtain an initial set of PSFs for the required radionuclide. Subsequently, a complete system matrix was generated with an interpolation process to fill in the matrix elements for the rest of the voxels within the FOV. Details of this procedure are explained below.

#### Calibration

A calibration step was necessary to determine the position and orientation of the collimator, and each detector in the real system as manufacturing inaccuracies could result in a geometry that is slightly different from the original design. This step was not necessary for simulated scans because the geometries in the simulation were exactly as designed. The calibration started with the measurement of a series of  $^{99m}\text{Tc}$  point-source responses with sources placed at multiple positions inside the collimator’s FOV (435 positions for EXIRAD-3D and 679 positions for HE-UHR-M). The number of positions was determined based on the setup in [54]. It depends on the ratio between the size of the collimator’s FOV and the matrix voxel size. The positions are distributed on a denser grid near the centre of the FOV than the locations further away from the centre, and in general, the grid’s unit size is about 10-40 times the voxel size. The number of point source positions could also be a bit smaller or larger than the stated value; however, it should not be too small to keep sufficient sampling in the FOV and not too large to prevent long calibration time. From the scan, a dataset was generated following the procedure in [54], with each entry containing the projection (PSF) location on the detector, and the corresponding pinhole and point-source

location. The same geometry fitting algorithm as in [36] was then performed to allow for the rigid transformation of the collimator and each detector to minimise the mean squared error between the measured and estimated PSF locations. Results of this fitting were 24 parameters describing the translation (3 parameters) and rotation (3 Euler angles) of the collimator and each of the three detectors. These parameters were subsequently used to transform the designed collimator and detectors and generate corresponding fitted STL files for the GATE simulation.

### Accelerated point-source simulation

4

This step is the key that allows for the accurate generation of PSFs for the radionuclide of interest based on MCS without additional measurements. In this simulation, an infinitely small point source was defined in GATE, with the same set of point-source positions as in the calibration measurement being used. The point source was assumed to be in water. A simple acceleration technique was applied for the point-source simulation by directing the photon emission from the point source to the pinholes in narrow beams instead of the default emission at all angles. This is a kind of forced detection – one of the variance reduction techniques in MCS. There exist several implementations of forced detection for pinhole SPECT [134, 135]. In our method, only the emission angle from the decay location at the point source is adjusted, and no alteration is applied at individual photon interaction points as in the other methods, meaning it is simple to implement in GATE at the macro level just by setting the span of the polar angle and the azimuthal angle of the emission distribution. Note that this acceleration technique was used for a point source, but it was not suitable for large sources and hence not used for the studied scans in Section 4.2.4.

In our acceleration technique, the photon beams were adapted for each point source and pinhole combination. Each beam formed a regular pyramid with an apex angle defined as (Figure 4.1, Equation (4.1)):

$$\alpha = 2 \arctan \left( \frac{r_{ph} c}{h} \right) \quad (4.1)$$

where  $r_{ph}$  is the pinhole diameter and  $h$  is the distance from the point source to the pinhole centre. The factor  $c$  was the same for all point-source positions and pinholes in a point-source simulation, but it can vary for different radionuclides. It was chosen manually (by checking PSF profiles) to be as small as possible to speed up the simulation while making sure that the beam always covers the entire pinhole and photon penetration and scattering inside the pinhole is not affected.

The pyramid's edges intersect with the detector's surface at four points defined by vectors  $\mathbf{x}$ ,  $\mathbf{y}$ ,  $\mathbf{z}$ ,  $\mathbf{t}$  from the point-source location (Figure 4.1). The solid angle subtended by the detector area seen by the photon beam composed of solid angles of two triangles [136] (Equation (4.2)):

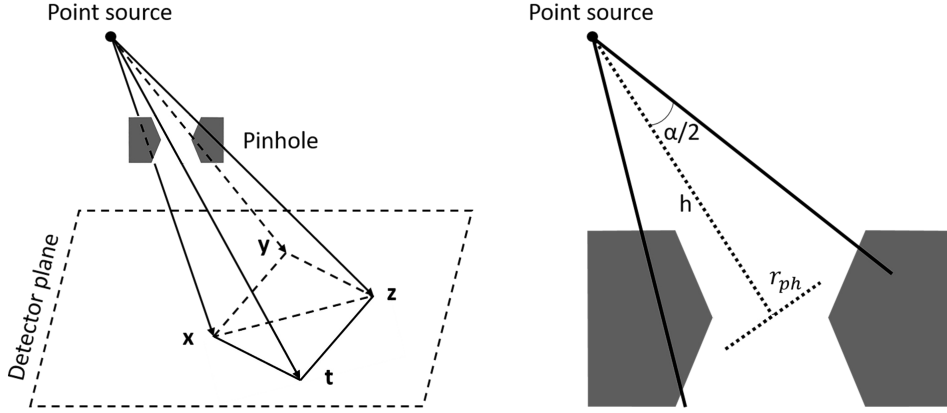


Figure 4.1: Accelerated point-source simulation by forced irradiation from the point source to each pinhole.

$$\Omega = 2 \arctan \left( \frac{\mathbf{x} \cdot (\mathbf{y} \times \mathbf{z})}{\|\mathbf{x}\| \|\mathbf{y}\| \|\mathbf{z}\| + (\mathbf{x} \cdot \mathbf{y}) \|\mathbf{z}\| + (\mathbf{x} \cdot \mathbf{z}) \|\mathbf{y}\| + (\mathbf{y} \cdot \mathbf{z}) \|\mathbf{x}\|} \right) + 2 \arctan \left( \frac{\mathbf{x} \cdot (\mathbf{z} \times \mathbf{t})}{\|\mathbf{x}\| \|\mathbf{z}\| \|\mathbf{t}\| + (\mathbf{x} \cdot \mathbf{z}) \|\mathbf{t}\| + (\mathbf{x} \cdot \mathbf{t}) \|\mathbf{z}\| + (\mathbf{z} \cdot \mathbf{t}) \|\mathbf{x}\|} \right). \quad (4.2)$$

The number of photon emissions in each beam was  $\Omega/4\pi$  times the total number of emissions in  $4\pi$ . This way, fewer photons needed to be traced, which ultimately resulted in a shorter simulation time. Only for the  $^{90}\text{Y}$  point-source simulation, the acceleration technique was not applied because with this radionuclide, the PSF tails were long and a large factor  $c$  was needed. As a result, the speedup factor is small, and there is a risk of having overlapping photon beams between different pinholes in a cluster.

### System matrix generation

The energy window applied in creating PSFs from the MCS outputs is exactly the same as the energy window applied in creating projection data from the scans Section 4.2.4. As a result, a single matrix is generated to reconstruct data from a specific energy window setting, no matter whether the projection data is from a single energy window or from multiple energy windows. The obtained PSFs from fast MCS were pre-processed to remove high-frequency noise by applying a Richardson-Lucy deconvolution followed by a Gaussian filter with the same kernel, as was also done in [54]. The kernel's FWHM was set to be 0.2 mm smaller than the detector's spatial resolution to avoid degrading the PSFs' resolution.

The above step created the PSFs for a small number of point-source positions, while the number of required matrix voxels was approximately  $2 \cdot 10^5$  and  $2.3 \cdot 10^3$  times more than that for EXIRAD-3D and HE-UHR-M, respectively. In order to obtain the full set of PSFs for

all voxels, the same interpolation method described in [54] was used. This process involved characterising the available PSFs using Gaussian modelling to calculate their location, flux, and width, followed by generalising these parameters over the object space using analytical models. Subsequently, the PSFs at the missing voxel location (not in the scan grid) was created by transforming the nearest available PSF on the detector using the parameters obtained above. As a result, a full system matrix was generated for each radionuclide and each energy window setting and stored on disk. For efficient storage, a cut-off  $C$  ( $>0$ ) was applied such that matrix elements that were  $>C\%$  of the maximum were saved.

#### 4.2.4 Studied scans

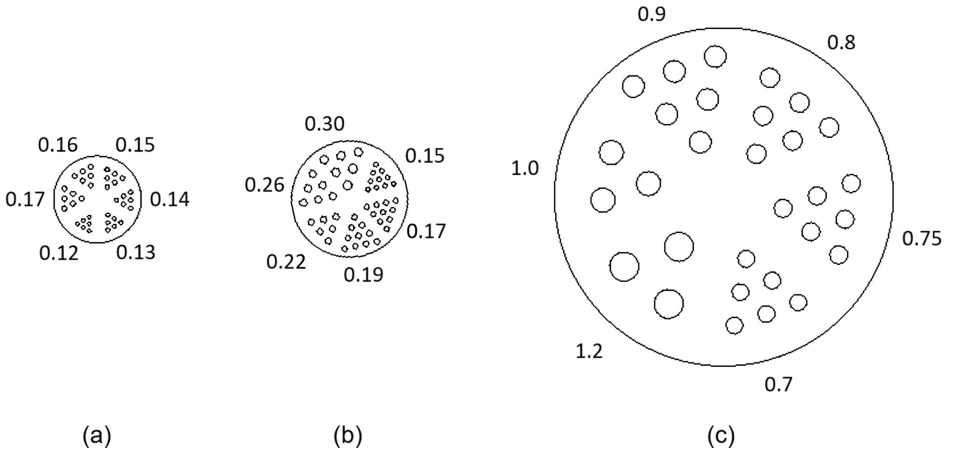


Figure 4.2: Derenzo phantoms with rod diameters indicated in mm. (a) Derenzo phantom 1 with 1.5-mm-long hot rods. (b) Derenzo phantom 2 with 2-mm-long hot rods. (c) Derenzo phantom 3 with 6-mm-long hot rods.

To evaluate the FMC-based matrix in various situations, complete scans have been performed experimentally or have been simulated using MCS. We used three Derenzo phantoms to assess image resolution, a cylindrical phantom to evaluate image uniformity, and a mouse thyroid scan to demonstrate a real tissue scan. Common SPECT radionuclides  $^{99m}\text{Tc}$ ,  $^{111}\text{In}$ , and  $^{123}\text{I}$  as well as two other important radionuclides,  $^{67}\text{Ga}$  and  $^{90}\text{Y}$ , were studied. The scans were performed with EXIRAD-3D, except for the  $^{90}\text{Y}$  scan, which was done with the HE-UHR-M collimator because the emission energies of  $^{90}\text{Y}$  were too high for imaging with EXIRAD-3D. The following sections describe the scans in detail.

#### Experimental $^{99m}\text{Tc}$ and $^{111}\text{In}$ Derenzo phantom scans

Derenzo phantom 1 having hot rods with diameters ranging from 0.12 – 0.17 mm and a length of 1.5 mm was filled with 4.06 MBq  $^{99m}\text{Tc}$ -pertechnetate and scanned for 3 h at nine bed positions. The rods were in a PMMA disk with a diameter of 8.5 mm and the same length as the rods. The photopeak window was set to 20% at 140 keV.

Derenzo phantom 2 having hot rods with diameters from 0.15 – 0.30 mm and a length of 2 mm was filled with 4.6 MBq  $^{111}\text{In}$  and scanned for 2 h at nine bed positions. The rods were in a PMMA disk with a diameter of 10 mm and the same length as the rods. The photopeak window was set to 20% at 171 keV. Although a 245 keV peak is prominent in the  $^{111}\text{In}$  acquisition energy spectrum, this photopeak was not used because it did not improve the image acquired at 171 keV with EXIRAD-3D.

### Experimental $^{99m}\text{Tc}$ cylindrical phantom scans

A cylindrical phantom with an inner diameter of 8.5 mm and an inner length of 9.5 mm was filled with 38.6 MBq  $^{99m}\text{Tc}$ -pertechnetate and scanned for 3 h at 128 beds positions. The phantom wall is 1.1 mm thick and made of PMMA. The photopeak window was set to 20% at 140 keV. The images were reconstructed with 100% and 50% of the counts randomly selected from the acquired list-mode data to assess the uniformity for different count levels.

4

### Experimental $^{123}\text{I}$ mouse thyroid scan

A C57BL/6 mouse was used for the thyroid scan, under a protocol approved by the Animal Research Committee at UMC Utrecht and in accordance with the Dutch Law on Animal Experimentation. The mouse was anaesthetised with isoflurane in air and injected intravenously via the tail vein with 10.25 MBq [ $^{123}\text{I}$ ]NaI. Four hours post-injection, the mouse was euthanised, and its thyroid was excised and snap-frozen in liquid nitrogen. The thyroid was then placed inside an aluminium holder filled with Tissue-Tek OCT compound (Sakura Finetek Europe, cat. no. 4583) and attached to a cooling unit to keep the tissue frozen throughout the scan. The tissue was scanned for 11 h at four bed positions. The photopeak window was set to 20% at 159 keV.

### Simulated $^{67}\text{Ga}$ scan: combining multiple photopeaks

$^{67}\text{Ga}$  SPECT is commonly used in detecting acute inflammation [137, 138] and various malignancies such as retroperitoneal fibrosis, lymphomas, cardiac sarcoidosis, and IgG4-related disease [139–142]. The  $^{67}\text{Ga}$  emission spectrum shows several prominent photopeaks (Figure 4.3), including 93 keV with 39.2% abundance, 184 keV with 21.2% abundance, and 300 keV with 16.8% abundance. Usually, the first two photopeaks are used in  $^{67}\text{Ga}$  SPECT either separately or jointly [143–145]. It is of interest to see the effect of combining these photopeaks in image reconstruction with a single FMC-based matrix that models both energy windows.

Derenzo phantom 1 with hot rods of diameters 0.12 – 0.17 mm was simulated. The rods were filled with 0.45 MBq  $^{67}\text{Ga}$  and scanned for 16 h with nine bed positions. No material was assumed in the environment surrounding the hot rods. The photopeak window was set to either 30% at 93 keV or 20% at 184 keV. Pre-/post-reconstruction combination of the data from separate energy windows was done as explained in Section 4.2.5.

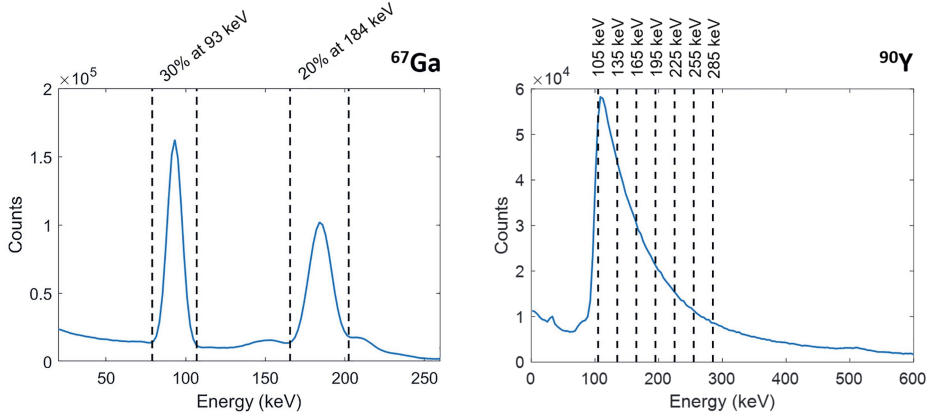


Figure 4.3: The acquisition energy spectra for  $^{67}\text{Ga}$  and  $^{90}\text{Y}$ , obtained from the Derenzo phantom scans for the central bed positions. The dashed lines define the selected energy windows for these scans.

### Simulated $^{90}\text{Y}$ scan: utilising a wide continuous energy spectrum

$^{90}\text{Y}$  is one of the most commonly used radionuclides for targeted radiotherapies and has been applied in innovative cancer treatments [146, 147]. Imaging of  $^{90}\text{Y}$  is needed for study and dosimetry to assess doses delivered to lesions and normal tissues. This can be done by either PET or bremsstrahlung SPECT. Although  $^{90}\text{Y}$  decay does not produce gammas, SPECT imaging has been done by utilising bremsstrahlung photons associated with beta emissions. Still, imaging is challenging due to the continuous energy spectrum of the bremsstrahlung photons (Figure 4.3), the low yield of bremsstrahlung photons in tissue, and the range from the beta decay location to the bremsstrahlung emission location. Because of difficulty in modelling the wide energy spectrum in the system matrix, only a relatively narrow energy window has been used [148]. It is desirable to include as many photons as possible by extending the energy window. Recently, several advanced methods have been applied to utilise photons acquired within a wider energy range, e.g. 105-285 keV or 0-2000 keV, that provide higher quality images than obtained when using a single narrow band [84, 132, 149]. This was done by having multiple sub-energy windows and energy-dependent matrices, and all of these matrices are used together in image reconstruction.

Here we approached this imaging situation in a different way. By using the FMC-based matrix, “continuous-energy” system modelling can be achieved in a single matrix. Each photon transport was modelled based on the photon energy which can lie anywhere within the selected wide acquisition window. This way, the acquisition window does not need to be separated into sub-bands, and the conventional reconstruction algorithm with a single matrix can be used, which reduces storage for the matrices and shortens reconstruction time.

Derenzo phantom 3 with hot rods of diameters 0.7 – 1.2 mm was simulated. The rods were filled with 105 MBq  $^{90}\text{Y}$  and scanned for 1.5 h with nine bed positions. The rods were in a

filled with 105 MBq  $^{90}\text{Y}$  and scanned for 1.5 h with nine bed positions. The rods were in a water environment - a cylinder with a diameter of 20 mm and a length of 10 mm - because the bremsstrahlung kernel of the “fastY90” source in GATE was pre-calculated in water. The energy window was set to 105-135 keV, 135-165 keV, 165-195 keV, 195-225 keV, 225-255 keV, or 255-285 keV. Pre-/post-reconstruction combination of the data from separate energy windows was done as explained in Section 4.2.5.

### 4.2.5 Image reconstruction and evaluation

Images were reconstructed using a similarity-regulated ordered-subset expectation maximisation algorithm [53]. The voxel size was set to 0.05 mm for EXIRAD-3D and to 0.4 mm for HE-UHR-M. A triple-energy window (TEW) method was applied to correct for the scatter and background radiation. To this end, two energy windows were placed on both sides of the acquisition window. The side window’s width was 20% ( $^{99m}\text{Tc}$ ,  $^{111}\text{In}$ ,  $^{123}\text{I}$ ), 25% ( $^{67}\text{Ga}$ ), or 5% ( $^{90}\text{Y}$ ) of the acquisition window’s width. For  $^{90}\text{Y}$ , the side window was relatively narrow to minimise the effect of the adjacent windows in the continuous energy spectrum. Attenuation correction can be performed for the presented scanners based on the method described in [121, 150]. However, for the scans with *ex vivo* and *in vivo* mouse collimators presented in this work, the object attenuation effect is small; therefore, attenuation correction was not performed.

The Derenzo phantom images were evaluated based on the contrast-to-noise ratio (CNR) calculated in the same way as in [37] and the system resolution defined as the diameter of the smallest discernible rod. The Derenzo images in the result section were displayed with the iteration number and the Gaussian post-filter size that maximised the CNR averaged over the rod sectors. All of the rod sectors were included in this calculation, except for the experimental  $^{111}\text{In}$  phantom scan, only the three smallest rod sectors were used because with all rod sectors, the obtained image was still too blurry. The cylindrical phantom was reconstructed with 20 iterations and a post-reconstruction 3D Gaussian filter having a FWHM of 0.6 mm was applied. Nine regions of interest (ROIs), each formed by a circular disk with 3-mm radius and 0.3-mm thickness, were evenly placed on the image at 0.45-mm intervals. The uniformity was calculated as the ratio of the standard deviation between the ROIs’ means to the average values of the ROIs, and represented as a percentage. The smaller this number is, the more uniform the reconstructed image is. The mouse thyroid images were reconstructed with 20 iterations followed by a 0.15-mm-FWHM 3D Gaussian filter and a 3\*3\*3 median filter. It was then assessed visually.

The  $^{90}\text{Y}$  beta-to-bremsstrahlung range was corrected in image reconstruction with a pre-calculated kernel which was applied in the forward projection step in reconstruction when using traditional or ray-tracing matrices. This is not required for the FMC-based matrix because this range was already modelled inside the matrix. The beta-to-bremsstrahlung range kernel was obtained from MCS of a  $^{90}\text{Y}$  point source in water.

For the scans where multiple energy windows were available ( $^{67}\text{Ga}$  and  $^{90}\text{Y}$ ), the data from these windows were combined in two approaches. In the first approach, projections

“pre-combined” image. In the second approach, reconstructed images from separate energy windows were summed to form a “post-combined” image.

#### 4.2.6 Comparison with traditional and ray-tracing methods

For all scans in this work, the FMC-based matrices were compared with the matrices generated with the “traditional” method [54] and the “ray-tracing” method [36] that have been commonly used for our nuclear scanners. The traditional matrices were created for 140 keV from a set of  $^{99m}\text{Tc}$  point-source measurements and used to reconstruct all radionuclides in this work; therefore, only one matrix is required for each collimator. Note that only for  $^{67}\text{Ga}$  and  $^{90}\text{Y}$ , all data was from simulation; therefore, the point-source “measurements” for the traditional matrices in these cases were also generated with Monte Carlo simulation. The ray-tracing matrices were created for the central energies of the selected energy windows; therefore, a new matrix was required when changing the radionuclide or energy window setting. For example, for the combined projection data from  $^{67}\text{Ga}$  (93 keV + 184 keV), the ray-tracing matrix was generated for 140 keV (about the mean of these two energies). For the combined projection data from  $^{90}\text{Y}$  (105-285 keV), the matrix was generated for 195 keV. The time necessary to generate matrices with different methods is summarised in Table 4.4.

Table 4.1: The cut-off used for each matrix in this work.

	EXIRAD-3D				HE-UHR-M
	$^{99m}\text{Tc}$	$^{123}\text{I}$	$^{111}\text{In}$	$^{67}\text{Ga}$	$^{90}\text{Y}$
Traditional	20%	20%	20%	0.1%	0.1%
Ray-tracing	4%	4%	4%	0.1%	0.1%
FMC-based	4%	4%	4%	0.1%	0.1%

Table 4.2: Energy-dependent attenuation coefficient ( $\text{mm}^{-1}$ ) in collimator material ( $\mu_c$ ) and in detector crystal ( $\mu_d$ ) that were used for generating ray-tracing matrices which are references to evaluate the FMC-based matrices.

EXIRAD-3D	93 keV	140 keV	159 keV	171 keV	184 keV		
$\mu_c$	9.165	3.242	2.362	1.974	1.656		
$\mu_d$	0.306	0.245	0.154	0.130	0.109		
HE-UHR-M	120 keV	150 keV	180 keV	195 keV	210 keV	240 keV	270 keV
$\mu_c$	5.132	2.914	1.861	1.538	1.293	0.957	0.744
$\mu_d$	0.258	0.175	0.115	0.094	0.082	0.061	0.047

The matrix cut-off (defined in Section 4.2.3) was set as in Table 4.1. For the simulated scans ( $^{67}\text{Ga}$  and  $^{90}\text{Y}$ ), the matrix cut-off was always 0.1%. For the experimental scans ( $^{99m}\text{Tc}$ ,  $^{123}\text{I}$ , and  $^{111}\text{In}$ ), the matrix cut-off was 20% for the traditional matrices and 4% for the other matrices. In principle, the smaller cut-off, the better; however, for the EXIRAD-3D experimental scans, the measured point source size ( $>100\text{ }\mu\text{m}$ ) was larger than the matrix voxel size ( $50\text{ }\mu\text{m}$ ), and we experimentally observed that a large cut-off compensated for

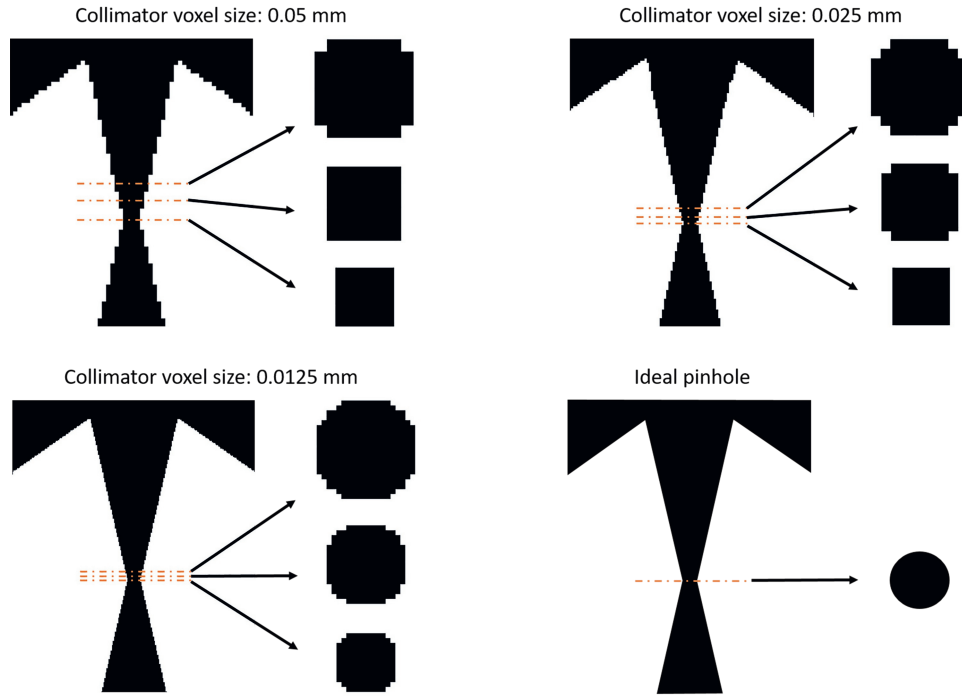


Figure 4.4: Zoom into a pinhole in the EXIRAD-3D collimator used for the ray-tracing matrices to illustrate the accuracy of the voxelised aperture. Black represents air and white represents collimator material. The pinhole diameter is 0.15 mm. The smallest collimator voxel size that was possible to be used in this paper is 0.025 mm.

the effect of a too large point source size. Ideally, the point source should be smaller than the matrix voxel; however, making a tinier point source than 100  $\mu\text{m}$  was difficult in our laboratory. Therefore, for the traditional matrices used in EXIRAD-3D experimental scans, we chose a matrix cut-off of 20% which resulted in higher-resolution images than a matrix cut-off of 4%, as shown in Figure 4.14 in the Appendix.

The ray-tracing code required energy-dependent attenuation coefficients of the collimator material ( $\mu_c$ ) and of the detector crystal ( $\mu_d$ ) (Table 4.2).  $\mu_c$  was obtained from [86, 87] and  $\mu_d$  was calculated from MCS in the same way as in [151]. The ray-tracing code also required a collimator file which was either an analytical description or a voxelised volume. Generating a matrix with the analytical collimator require less computation time than with the voxelised collimator. The analytical description was sufficiently accurate for HE-UHR-M, while the voxelised volume was needed for EXIRAD-3D to model complex shielding layer that are difficult to be described analytically. The voxel size of the voxelised collimator should be small enough to avoid the discretisation effect of the pinholes (0.15 mm in diameter for EXIRAD-3D), but too small collimator voxels significantly increase the ray-tracing time. For this EXIRAD-3D collimator, the finest voxel size that can be set was 0.025 mm which is still relatively coarse compared to the pinhole diameters (Figure 4.4),

but it was hard to reduce it further while keeping a feasible matrix calculation time.

## 4.3 Results

### 4.3.1 Validation of accelerated point-source simulation

Figure 4.5 compares the accelerated point-source simulation (fast MCS) with the full Monte Carlo simulation (MCS) of a  $^{99m}\text{Tc}$  point-source scan for EXIRAD-3D. The presented PSF corresponds to photons from a point source at the collimator's centre going through three different pinholes. Both the 2D PSFs and the 1D profiles indicate that the acceleration method for point-source simulation produces the same PSFs as the full simulation does. This is true for PSFs with other point source positions. The normalised root mean squared error between PSFs from MCS and fast MCS is about  $4.2 \times 10^{-4}$ . Meanwhile, the accelerated version takes significantly less computation time compared to the full simulation, as summarised in Table 4.3. In this table, the time for simulating a full set of PSFs for each of the studied FMC-based matrices in this work and the chosen factor  $c$  as described in Section 4.2.3 are reported. The timing was done on a Linux cluster with Intel(R) Xeon(R) CPUs E5-2620, and 250 cores were used in total.

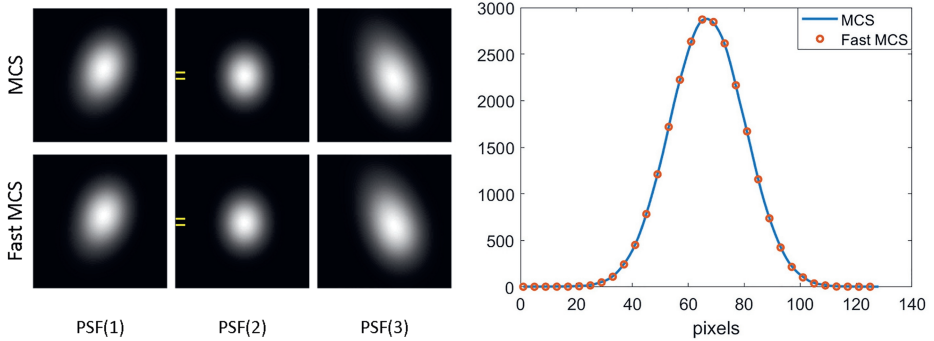


Figure 4.5: A comparison between full Monte Carlo simulation and accelerated simulation of a point-source scan with  $^{99m}\text{Tc}$  and the EXIRAD-3D collimator. (a) 2D PSF at three different locations on the detector. (b) 1D profiles through PSF(2) at the location indicated by yellow lines. For reference to the profiles from the traditional and ray-tracing methods, please see Figure 4.13 in the Appendix.

### 4.3.2 Experimental $^{99m}\text{Tc}$ and $^{111}\text{In}$ in phantom scans

Figure 4.6 presents the experimental results of the Derenzo phantom scans with  $^{99m}\text{Tc}$  and  $^{111}\text{In}$ . The traditional matrix yielded comparable image resolutions as the FMC-based matrix while showing a visually lower contrast between the hot rods and the background regions between the rods. This is probably because the point source used in the calibration scan was too large while ideally, the point source size should be smaller than the image voxel size, as illustrated in Figure 4.13 and Table 4.5 in the Appendix. The ray-tracing

Table 4.3: Chosen factor  $c$  (used in Equation (4.1)) and time required for point-source simulations, comparing MCS and fast MCS. The listed time included the GATE simulation time and the time to generate raw PSFs from the GATE output files. Note that the acceleration was not applied for  $^{90}\text{Y}$ , as previously explained in Section 4.2.3.

	EXIRAD-3D				HE-UHR-M
	$^{99m}\text{Tc}$	$^{123}\text{I}$	$^{111}\text{In}$	$^{67}\text{Ga}$	$^{90}\text{Y}$
$c$	3.0	3.0	5.0	5.0	N/A
MCS	34 h	34 h	42 h	22 h	59 h
Fast MCS	32 min	32 min	61 min	51 min	N/A

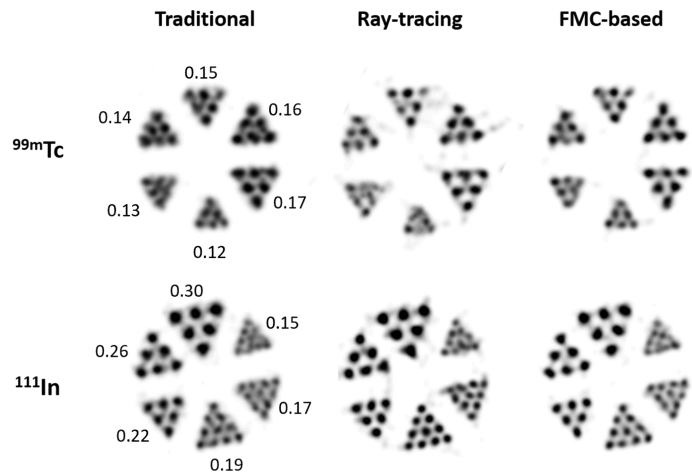


Figure 4.6: Experimental Derenzo phantom scans with  $^{99m}\text{Tc}$  and  $^{111}\text{In}$  with the EXIRAD-3D collimator to compare images resulting from the FMC-based matrices with those obtained with the reference matrices. The images were displayed with the iteration number and the filter size that maximise the CNR. Slice thicknesses were 0.2 mm and 0.8 mm for  $^{99m}\text{Tc}$  and  $^{111}\text{In}$ , respectively. Profiles through these images can be seen in Figure 4.16 in the Appendix.

matrix resulted in images with more background artefacts than the other matrices. We believe this is because the collimator voxel size of 0.025 mm was still not fine enough to represent the 0.15-mm diameter pinholes accurately (Figure 4.4). It was hard to reduce this collimator voxel size further while still keeping a practical matrix generation time. Generating the ray-tracing matrix for EXIRAD-3D took about 11-13 days (Table 4.4) on a Windows server with Intel® Xeon® CPU E5-2680 v3 (48 cores) and was thus already impractically long. For both scans, the FMC-based matrices achieved higher CNRs than the traditional and ray-tracing matrices (Figure 4.7). Table 4.4 also presents the time to generate matrices with different methods, showing that FMC-based method needed slightly more time than the traditional method and significantly less time than the ray-tracing method. Note that in case of  $^{90}\text{Y}$ , the ray-tracing method used an analytical description of the collimator instead of a voxelised volume; therefore, it was faster than the FMC method.

Table 4.4: The time required to generate matrices with FMC-based method, traditional method, and ray-tracing method. For the FMC-based matrices, the time already included the FMCS time (Table 4.3). The time to generate traditional matrices was the same for different radionuclides because these matrices only modelled photon transport at 140 keV.

	EXIRAD-3D				HE-UHR-M
	$^{99m}\text{Tc}$	$^{123}\text{I}$	$^{111}\text{In}$	$^{67}\text{Ga}$	$^{90}\text{Y}$
Traditional	2.8 h	2.8 h	2.8 h	2.8 h	23 min
Ray-tracing	11.7 d	12.1 d	13.0 d	12.1 d	1.6 d
FMC-based	3.3 h	3.4 h	4.2 h	6.3 h	2.5 d

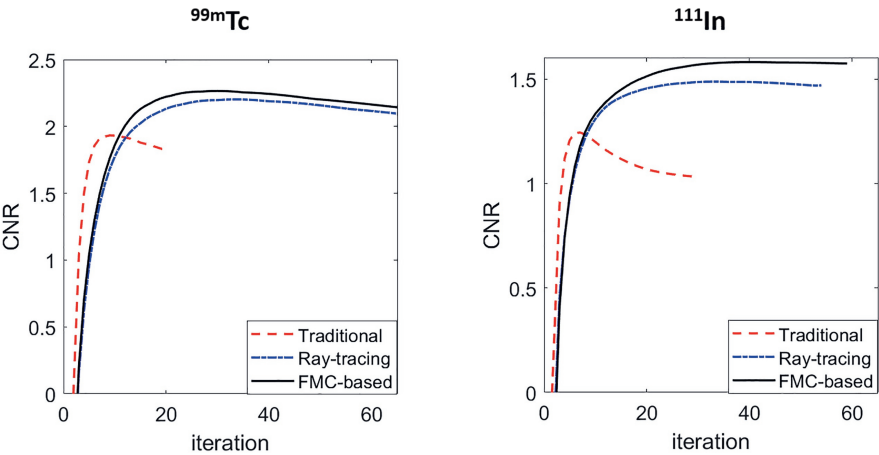


Figure 4.7: CNR comparison between the FMC-based matrices and the reference matrices for the experimental Derenzo phantom scans with  $^{99m}\text{Tc}$  and  $^{111}\text{In}$ . The traditional matrix used a  $>100\text{-}\mu\text{m}$  point source, while the FMC-based matrix used a  $0\text{-}\mu\text{m}$  point source.

Figure 4.8 presents the experimental results of the uniform phantom scan with  $^{99m}\text{Tc}$ . For each scan, an axial slice and a coronal slice were shown, and the calculated uniformity measures were provided. Note that a lower number for this measure means better image uniformity. With each matrix, we observed that the obtained uniformity converges quickly after only a few iterations (Figure 4.15 in the Appendix). In all of the cases presented, the FMC-based matrix yielded the most uniform image among all matrices tested.

### 4.3.3 Experimental $^{123}\text{I}$ mouse thyroid scan

Figure 4.9 shows images of the mouse thyroid reconstructed with the FMC-based matrix and the reference matrices. The images clearly visualised two thyroid lobes that are connected by a thin isthmus (see the coronal slices in Figure 4.9). The isthmus was seen because it also had iodine uptake and its width of about  $0.3\text{ mm}$  [120] can be well visualised due to the high resolution of EXIRAD-3D. Among the matrices used, the traditional matrix

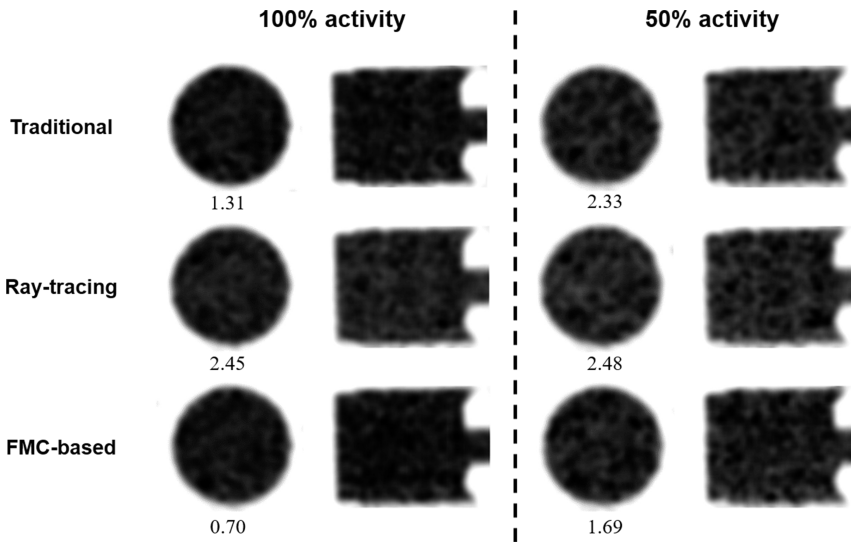


Figure 4.8: Experimental cylindrical phantom scan with  $^{99m}\text{Tc}$  to compare the FMC-based matrix with the reference matrices. The uniformity is listed under the image. The smaller this number, the better. Slice thickness was 0.2 mm.

resulted in a slightly more blurry image, especially when looking at the isthmus. The other matrices yielded visually almost similar images. Although there is no ground truth in this experiment to quantitatively compare the matrices' performance, we can conclude that the FMC-based matrix works with the real mouse tissue scan.

#### 4.3.4 Simulated $^{67}\text{Ga}$ scan: combining multiple photopeaks

Figure 4.10 compares the EXIRAD-3D  $^{67}\text{Ga}$  reconstructions with different matrices and several energy window settings. In all of the presented cases, the 93 keV photopeak produced images with clearer rods than the 184 keV photopeak. Post-reconstruction combining the images from separate energy windows did not show a clear advantage over only using the 93 keV photopeak. Pre-reconstruction combining the data and using a single matrix in reconstruction yielded the best image. The traditional matrix and ray-tracing matrix resulted in good images in the pre-combined case; however, with a little distortion in the 0.12-0.13 mm rod sectors. The FMC-based matrix performed better than the traditional and ray-tracing matrices by showing faithful shapes of the 0.13-mm rods, almost separating the rods in the 0.12-mm sector, and yielding the highest CNR (Figure 4.11). With this  $^{67}\text{Ga}$  scan, a resolution of 0.13 mm was achieved.

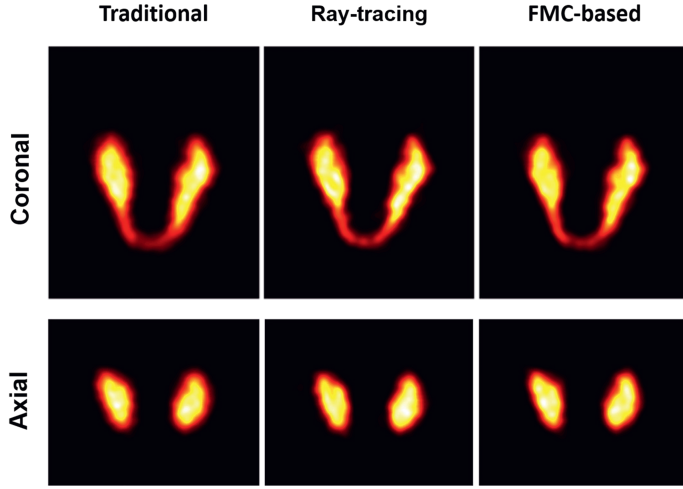


Figure 4.9: Experimental mouse thyroid scan with  $^{123}\text{I}$  to compare the FMC-based matrix with the reference matrices. Slice thickness was 0.2 mm.

#### 4.3.5 Simulated $^{90}\text{Y}$ scan: utilising a wide continuous energy spectrum

Figure 4.12 compares the HE-UHR-M  $^{90}\text{Y}$  reconstructions with different matrices and several energy window settings. The 105-135 keV energy window produced better images than the other single energy windows. This is understandable because more photons were detected within this window than in the other windows (Figure 4.3). For all matrices, post-reconstruction combining the images from separate energy windows did not show a clear advantage over using the individual energy windows. Pre-reconstruction combining the data and using a single FMC-based matrix in reconstruction yielded the best image visually and also the highest CNR (Figure 4.11). With this  $^{90}\text{Y}$  scan, a resolution of 0.75 mm was achieved.

## 4.4 Discussion

We have introduced an efficient and accurate Monte-Carlo based system matrix generation method for pinhole SPECT and validated it on our VECTOR scanner with a HE-UHR-M collimator and an EXIRAD-3D collimator for a wide range of radionuclides. In the presented imaging situations, the FMC-based matrix demonstrates advantages over the traditional and ray-tracing matrices. These advantages are mainly exhibited in two aspects. First, for very-high-resolution imaging, i.e. with EXIRAD-3D, the FMC-based matrix lessens the difficult task of fabricating a tiny point source, smaller than the image voxels (50  $\mu\text{m}$  for EXIRAD-3D), as needed with the traditional matrix, and avoids extensive matrix computation time as with the ray-tracing matrix. Second, for imaging radionuclides with complex emission energy spectra such as  $^{67}\text{Ga}$  and  $^{90}\text{Y}$ , the FMC-based matrix offers a

single-matrix image reconstruction solution by modelling multiple photopeak windows or a wide continuous energy window into one matrix. With the ray-tracing method, it is in principal also possible to combine matrices from multiple energies into a single matrix by summing matrix elements for the corresponding voxel-to-pixel paths with certain weights that are proportional to the emission yields at different energies. However, it takes time to perform the same ray-tracing simulation for multiple energies, and it is hard to do this for the continuous emission spectrum of  $^{90}\text{Y}$ . In other cases, with systems having lower resolutions than the resolution that EXIRAD-3D offers, and with radionuclides emitting single energy spectra, the traditional or ray-tracing matrices are expected to be a good choice; however, the FMC-based matrix can be used as well. Therefore, the FMC-based matrix generation method can be a versatile system modelling method for pinhole SPECT systems.

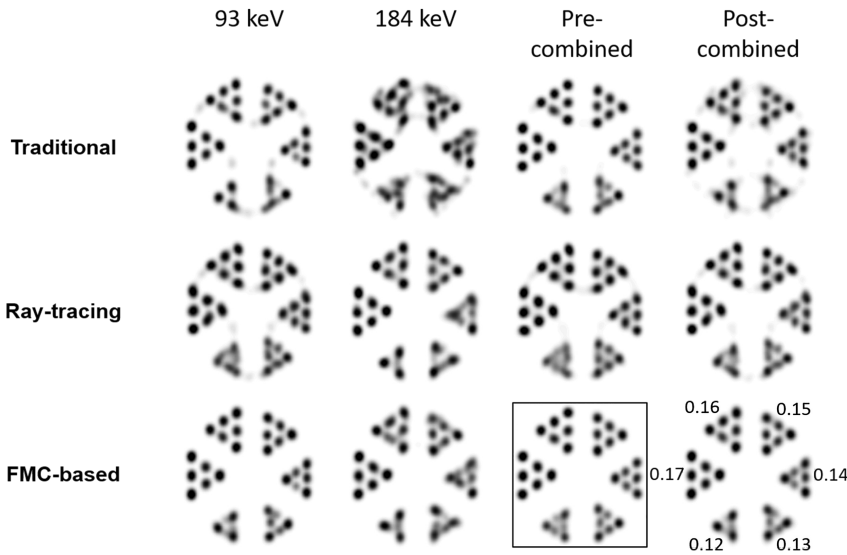


Figure 4.10: Simulated Derenzo phantom scan with  $^{67}\text{Ga}$ . The images were displayed with the iteration number and the filter size that maximise the CNR. The image with the highest CNR was highlighted in a box. Slice thickness was 0.8 mm. Profiles through these images can be seen in Figure 4.16 in the Appendix.

The FMC-based matrix already models realistic image degrading effects, such as positron range or beta-to-bremsstrahlung range, which are not always included in the traditional and ray-tracing matrices. In this work, we have not examined in depth all these effects and only shown the effect of modelling beta-to-bremsstrahlung range for  $^{90}\text{Y}$ . In this case, correcting the beta-to-bremsstrahlung range in the forward projection step of image reconstruction also worked with the traditional and ray-tracing matrices and the need for modelling it inside the matrix as with the FMC-based method was not clear. However, the proposed method is at least simpler than the traditional and ray-tracing methods in the sense that an additional effort to correct for these image-degrading effects is not needed.

Monte-Carlo simulation is usually computationally expensive; however, the point-source

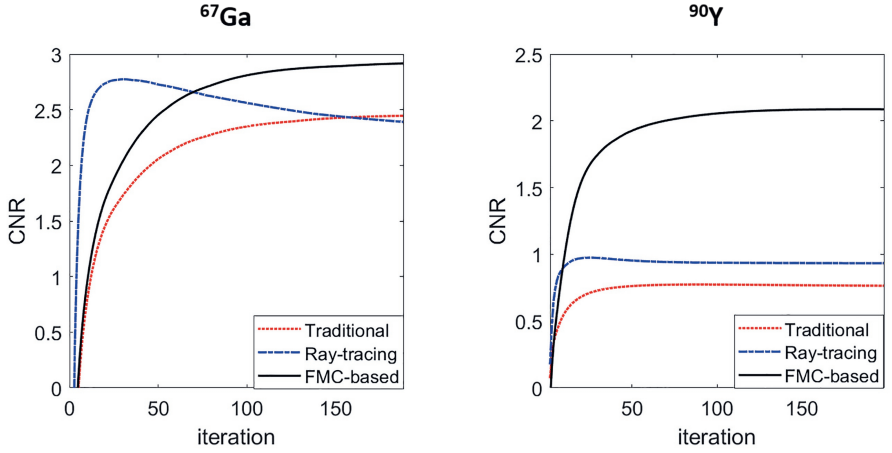


Figure 4.11: CNR comparison between the FMC-based matrices and the reference matrices for the simulated Derenzo phantom scans with  $^{67}\text{Ga}$  and  $^{90}\text{Y}$ . This figure only showed the best case for each matrix generation method (the pre-combined image). Both the traditional and FMC-based matrices for these simulated scans used a  $0\text{-}\mu\text{m}$  point source.

simulation acting as the key step in the FMC-based system modelling procedure takes a relatively short time (less than 1 hour for most of the cases in Table 4.3) thanks to the used acceleration technique (Section 4.2.3). Therefore, FMC-based matrix generation time is only slightly longer than the time required for making the traditional matrix and can be significantly shorter than the time required for calculating the ray-tracing matrix. For instance, generating a matrix for EXIRAD-3D and  $^{99\text{m}}\text{Tc}$  takes about 1.5 days with the FMC-based method or the traditional method, while it takes about 12 days with the ray-tracing method.

With the FMC-based system modelling, ideally, a new matrix needs to be generated when the radionuclide or the energy window setting changes. For a new radionuclide, the procedure needs to be restarted from the point-source simulation step, but if only the energy window setting is adjusted for the same radionuclide, the point-source simulation step does not need to be performed again. Besides, the PSF fitting step in the proposed method uses Gaussian functions, which work well in modelling PSFs for the studied energies ( $\leq 285\text{ keV}$ ). When imaging high-energy isotopes such as PET isotopes, because of more scatter and penetration occurring near the pinhole edges, more complex functions should be used.

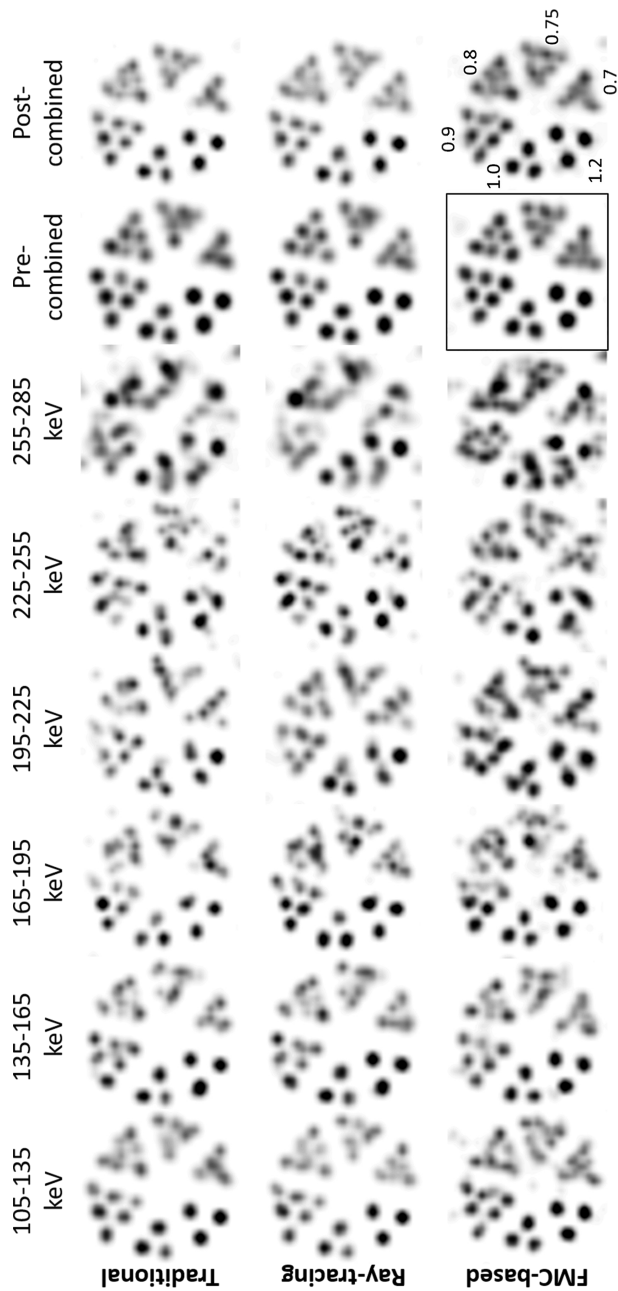


Figure 4.12: Simulated Derenzo phantom scan with  $^{90}\text{Y}$ . The ray-tracing matrix used an analytical collimator, so there was no problem of collimator voxelisation. The images were displayed with the iteration number and the filter size that maximise the CNR. The image with the highest CNR was highlighted in a box. Slice thickness was 2 mm. Profiles through these images can be seen in Figure 4.16 in the Appendix.

## 4.5 Conclusion

This work presents a new FMC-based system modelling method for ultra-high-resolution pinhole SPECT. The results show that the proposed method is efficient, accurate, and versatile in creating energy-dependent system matrix for various radionuclides. It is more generalised than the traditional method when changing radionuclide or energy window setting, and more computationally efficient than the ray-tracing method for very-high-resolution systems such as EXIRAD-3D. The FMC-based method also shows the advantage of being able to combine energies in a single matrix.

## Acknowledgements

The authors would like to thank Sofia Koustoulidou for helping with the experimental scans, and Chris Kamphuis for helping with image reconstructions as well as giving insightful comments and discussions.

## Appendix

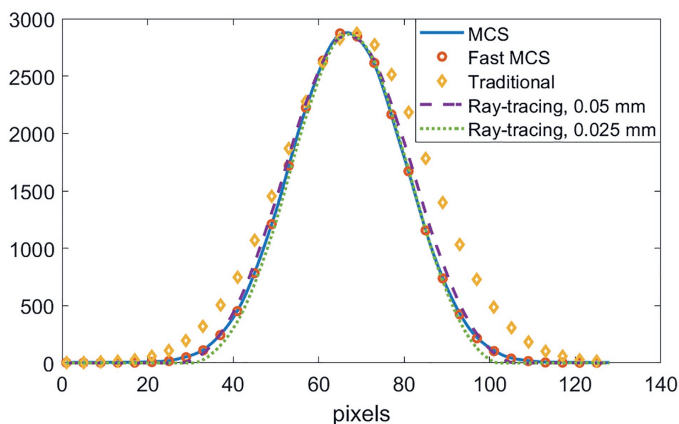


Figure 4.13: Profiles through a PSF location from a point-source scan with  $^{99m}\text{Tc}$  and the EXIRAD-3D collimator. The results are from the MCS, the fast MCS, the traditional matrix, and the ray-tracing matrix. Note that the wide PSF with the traditional matrix is due to a too large point source used in the measurement. Two collimator voxel size were presented for the ray-tracing matrix.

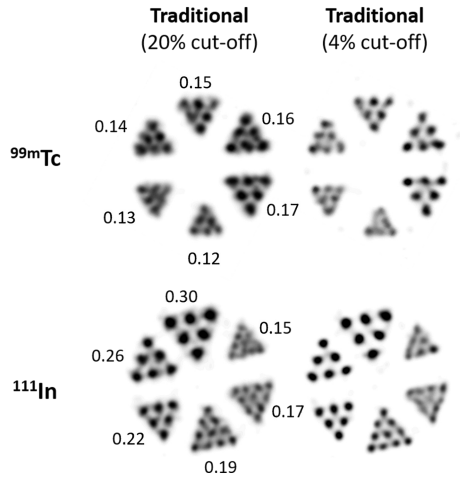


Figure 4.14: Experimental Derenzo phantom scans with  $^{99m}\text{Tc}$  and  $^{111}\text{In}$  with the EXIRAD-3D collimator to compare different cut-offs used for the tradition matrices. The images were displayed with the iteration number and the filter size that maximise the CNR. Slice thicknesses were 0.2 mm and 0.8 mm for  $^{99m}\text{Tc}$  and  $^{111}\text{In}$ , respectively. For both radionuclides, the traditional matrix with 20% cut-off yielded images that resolve smaller rods than the traditional matrix with 4% cut-off. We believe this is because a higher cut-off compensates for the point source size ( $>100\text{-}\mu\text{m}$  diameter) used for calibration that could not be made smaller than the image voxel size ( $50\text{ }\mu\text{m}$ ). This is also demonstrated in Table 4.5 which shows the effect of the point source size.

Table 4.5: Effect of the size of the point source used in calibration measurement on the reconstruction of the Derenzo phantom scan with  $^{99m}\text{Tc}$ . The listed CNR is the highest that was achieved with the optimal iteration number and filter size. The real fabricated point source had a diameter of  $>100\text{ }\mu\text{m}$ , while the diameter of the simulated point source in GATE was easily adjusted to  $100\text{ }\mu\text{m}$  and  $\sim 0\text{ }\mu\text{m}$  (an exact point).

Traditional		FMC-based	
PS $>100\text{ }\mu\text{m}$ 20% cut-off CNR = 1.93	PS $>100\text{ }\mu\text{m}$ 4% cut-off CNR = 1.55	PS $100\text{ }\mu\text{m}$ 4% cut-off CNR = 1.75	PS $\sim 0\text{ }\mu\text{m}$ 4% cut-off CNR = 2.27

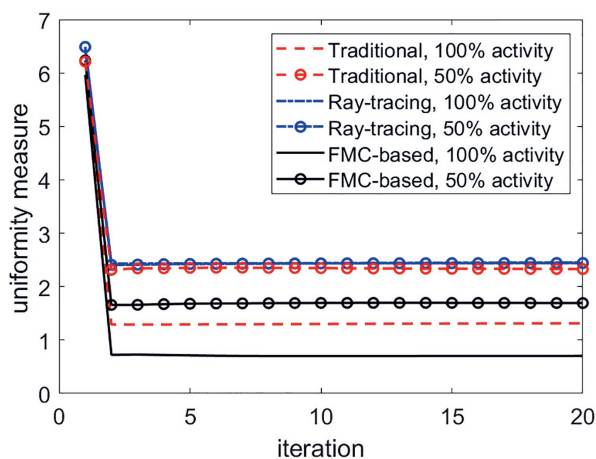


Figure 4.15: Uniformity versus iteration number for the experimental cylindrical phantom scan with  $^{99m}\text{Tc}$  showed in Figure 4.8, comparing the FMC-based matrix with the reference matrices. A smaller number means a better uniformity.

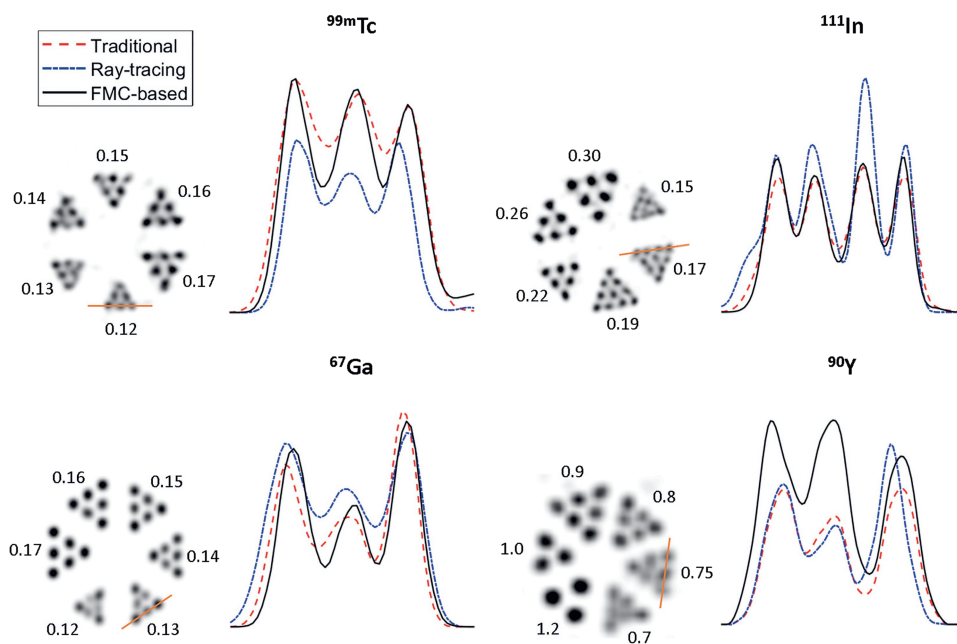


Figure 4.16: Profiles obtained from the best reconstructed Derenzo phantom image (highest CNR) in Figures 4.6, 4.10 and 4.12 for each matrix generation method. Locations of the profile is indicated with a line drawn on the smallest discernible rod sector in each case. The rod diameters are shown in mm.

## Chapter 5

# EXIRAD-HE: Multi-pinhole high-resolution *ex vivo* imaging of high-energy isotopes

---

This chapter is adapted from:

**Minh Phuong Nguyen**, Marlies C. Goorden, and Freek J. Beekman. EXIRAD-HE: multi-pinhole high-resolution *ex vivo* imaging of high-energy isotopes. *Physics in Medicine & Biology* 65.22: 225029, 2020.

**W**<sup>E</sup> developed a dedicated focusing multi-pinhole collimator for a stationary SPECT system that offers down to 120  $\mu\text{m}$  (or 1.7 nL) spatial resolution SPECT images of cryo-cooled tissue samples (EXIRAD-3D). This collimator is suitable for imaging isotopes that are often used in small animal and diagnostic SPECT such as  $^{125}\text{I}$  (27 keV),  $^{201}\text{Tl}$  (71 keV),  $^{99\text{m}}\text{Tc}$  (140 keV), and  $^{111}\text{In}$  (171 and 245 keV). The goal of the present work is to develop high-resolution pinhole imaging of tissue samples containing isotopes with high-energy photon emissions, for example, therapeutic alpha and beta emitters that co-emit high energy gammas (e.g.  $^{213}\text{Bi}$  (440 keV) and  $^{131}\text{I}$  (364 keV)) or 511 keV annihilation photons from PET isotopes. To this end, we optimise and evaluate a new high energy small-bore multi-pinhole collimator through simulations. The collimator-geometry was first optimised by simulating a Derenzo phantom scan with a biologically realistic activity concentration of  $^{18}\text{F}$  at two system sensitivities (0.30% and 0.60%) by varying pinhole placements. Subsequently, the wall thickness was selected based on reconstructions of a Derenzo phantom and a uniform phantom. The obtained collimators were then evaluated for  $^{131}\text{I}$  (364 keV),  $^{213}\text{Bi}$  (440 keV),  $^{64}\text{Cu}$  (511 keV), and  $^{124}\text{I}$  (511 + 603 keV) with biologically realistic activity concentrations, and also for some high activity concentrations of  $^{18}\text{F}$ , using digital resolution, mouse knee joint, and xenograft phantoms. Our results show that placing pinhole centres at a distance of 8 mm from the collimator inner wall yields good image quality, while a wall thickness of 43 mm resulted in sufficient shielding. The collimators offer resolutions down to 0.35 mm, 0.6 mm, 0.5 mm, 0.6 mm, and 0.5 mm when imaging  $^{131}\text{I}$ ,  $^{213}\text{Bi}$ ,  $^{18}\text{F}$ ,  $^{64}\text{Cu}$ , and  $^{124}\text{I}$ , respectively, contained in tissue samples at biologically achievable activity concentrations.

## 5.1 Introduction

Preclinical imaging of radiolabeled molecule distributions in small animals plays an important role in studying the mechanisms of disease and developing diagnostic tracers [152]. A wide and steadily increased variety of tracers with different radioisotopes is available. While conventional SPECT scanners are designed to image isotopes emitting gammas with a typical energy of around 140 keV, many available and emerging isotopes emit gammas with higher energies. These include PET tracers that emit 511 keV annihilation photons (e.g.  $^{18}\text{F}$ ,  $^{124}\text{I}$ , and  $^{64}\text{Cu}$ ), and alpha or beta emitters for theranostic applications that co-emit high-energy gammas (e.g.  $^{131}\text{I}$ ,  $^{213}\text{Bi}$ , and  $^{209}\text{At}$ ). Many commercial preclinical PET scanners for imaging positron emitters have been launched. Recent ones include Mediso NanoPET/CT [153], Bruker Albira [154], Clairvivo [155], and Molecubes  $\beta$ -CUBE [156], which achieve resolutions down to approximately 0.9 mm. With one small field-of-view (FOV) prototype coincidence system, a resolution of 0.6 mm was obtained [157].

In another approach, PET isotopes are successfully imaged using dedicated clustered multi-pinhole collimators in a triangular detector set up (VECTor) at an initial resolution of <0.75 mm *in vivo* for  $^{18}\text{F}$  [34, 36, 37]. Today resolutions of commercial VECTor scanners are <0.6 mm for  $^{18}\text{F}$  simultaneously with 0.4 mm resolution  $^{99\text{m}}\text{Tc}$  imaging. Compared to coincidence PET, multi-pinhole PET effectively removes or reduces several image degrading effects that significantly limit the image quality in small animals. These include limited detector resolution and depth-of-interaction effects whose influence can be strongly diminished by

pinhole magnification, as well as non-collinearity of annihilation photons, and random coincidences which do not play a role in pinhole PET. As a result, the resolution of VECTOR can outperform coincidence PET in a subset of imaging situations [37]. In addition, with VECTOR, the prompt gammas that are emitted by some PET isotopes (e.g. 603 keV for  $^{124}\text{I}$ ) can be employed to exclude the effect of positron range that sets a fundamental limit on the resolution in coincidence PET. This enables for example 0.75 mm resolution PET of  $^{124}\text{I}$  and  $^{89}\text{Zr}$  [35, 38] as well as multi-isotope PET. At the same time, VECTOR has the capability of sub-mm resolution imaging of isotopes that emit single gammas above the conventional SPECT energy range like  $^{131}\text{I}$  (364 keV),  $^{213}\text{Bi}$  (440 keV), and  $^{209}\text{At}$  (545 keV) [39–41]. Therefore, multi-pinhole imaging is a single-system solution for high-resolution imaging of gamma- and positron-emitting isotopes over a broad energy range.

One way to improve the resolution-sensitivity trade-off of tissue samples in pinhole SPECT and PET is to increase the pinhole magnification factor by decreasing the collimator's FOV. This concept was used for the *ex vivo* imaging technique EXIRAD-3D (MILabs B.V.), which was designed for low and medium energy isotopes such as  $^{125}\text{I}$  (27 keV),  $^{201}\text{Tl}$  (71 keV),  $^{99\text{m}}\text{Tc}$  (140 keV), and  $^{111}\text{In}$  (171 keV and 245 keV) [118, 129]. With this technique, 120  $\mu\text{m}$  (or 1.7 nL) resolution was obtained for  $^{99\text{m}}\text{Tc}$ , i.e. about a ten times better volumetric resolution than state-of-the-art *in vivo* preclinical SPECT [27]. EXIRAD-3D consists of a dedicated small FOV multi-pinhole collimator, a tissue holder connected directly to a refillable chamber with dry ice for cryo-cooling the tissue throughout the scan, and dedicated acquisition and reconstruction software.

Today, EXIRAD-3D coupled with *in vivo* imaging modules as is done in the commercial MILabs' nuclear scanners offers both longitudinal information of biological and physiological functions and extra-fine three-dimensional image details, with a direct link between the two datasets. That is achieved with little more effort than the conventional *in vivo* imaging workflow without the need for whole new equipment and a complicated tissue sectioning and handling process as in a histological study. However, note that EXIRAD-3D is only designed for imaging gamma-emitters but not pure alpha- and beta-emitters.

The aim of the present paper is to design an EXIRAD option (EXIRAD-HE) that is also suited for imaging high-energy isotopes. The approach is to use narrow pinhole opening angles to suppress pinhole edge penetration and scatter, with thick collimator's walls. Full system simulations of a Derenzo phantom scan and a cylindrical phantom scan with a biologically realistic activity concentration of  $^{18}\text{F}$  were performed for various collimator designs at two system sensitivities (0.30% and 0.60%). Best performing collimators were subsequently evaluated for  $^{18}\text{F}$  scans with several activity concentrations and for  $^{64}\text{Cu}$ ,  $^{124}\text{I}$ ,  $^{213}\text{Bi}$ , and  $^{131}\text{I}$  with digital joint and xenograft phantoms.

## 5.2 Methods

### 5.2.1 Considerations in collimator design and optimisation

The EXIRAD-HE collimator (see Figure 5.1) is designed to have the same central field-of-view (CFOV) size (4-mm diameter) and inner diameter (21 mm) as the available low-energy

collimator meaning that the same size tissue volumes can be scanned by means of the scanning focus method [32]. With this method, the tissue is moved to multiple positions inside the collimator such that the whole tissue volume is viewed by the CFOV, and acquisitions from all of the scanned positions are used together in image reconstruction. The collimator is mounted in a U-SPECT or VECTOR system having a fixed triangular detector setup with three large-field-of-view gamma cameras. In this study, we assume a 9.5-mm-thick NaI(Tl) crystal with a usable area of  $497.4 \times 410.6 \text{ mm}^2$  for each detector. The crystal surface is placed at a distance of 210 mm from the collimator's centre. The EXIRAD-HE collimator contains a large number of round knife-edge pinholes placed manually in such a way that overlapping pinhole projections are limited without using a shielding layer (see Section 5.2.4(iii)). All pinholes' axes point towards the collimator's centre, and the pinholes' centres are placed at the same distance from the collimator's longitudinal axis. Collimator material assumed is a tungsten alloy consisting of 97% W, 1.5% Ni, and 1.5% Fe.

## 5

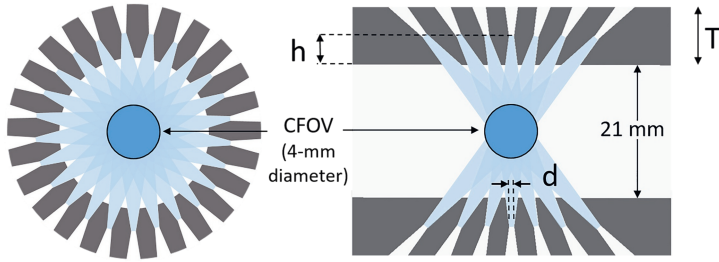


Figure 5.1: Sketch of the EXIRAD-HE focusing multi-pinhole collimator. Pinholes are placed in several rings and all focus on a central FOV.

With the above-mentioned constraints, we restricted the parameters for optimisation to be the distance from the pinhole's centre to the collimator's inner surface ( $h$ ), the pinhole diameter ( $d$ ), and the wall thickness ( $T$ ) (see Figure 5.1). Other parameters as listed in Table 5.1, if not fixed, can be expressed by these parameters. For example, pinhole opening angle only depends on  $h$  because the size of the CFOV (4-mm-diameter sphere) and the distance from the collimator's longitudinal axis to the collimator's inner surface (10.5 mm) were fixed. Also, the total number of pinholes were calculated from the detector size ( $3 \times 497.4 \times 410.6 \text{ mm}^2$ ) and the size of pinhole projections (again only depending on  $h$ ) (see Equation (5.3)). For the three parameters to be optimised, the following considerations were taken into account:

- For  $h$ , one may expect that the closer the pinhole is to the object (i.e.  $h \rightarrow 0$ ), the higher the system resolution that can be achieved for a fixed sensitivity [158]. This suggests putting the pinhole apertures as close to the inner surface of the collimator as possible. However, putting pinholes closer gives more sensitivity per pinhole but fewer pinholes that can be placed for the same detector area, which in some cases, limits the resolution-sensitivity trade-off [15]. Besides, for the high energy photons (e.g. 511 keV), putting pinholes closer to the inner collimator wall would result in a significant increase of pinhole edge scatter and penetration because of shorter paths

that photons travel through the pinhole edges, which deteriorates image quality. Thus an intermediate value for  $h$  may be most beneficial.

- The pinhole diameter  $d$  directly decides the resolution-sensitivity trade-off of the system: reducing the pinhole diameter improves the resolution at the expense of decreasing the sensitivity and vice versa.
- For  $T$ , we would expect that the larger the wall thickness, the better prevention of direct collimator wall penetration which is important for image quality. However, the thicker the collimator, the heavier and more expensive the collimator is which limits its practical use as a final product.

It is not straightforward to find an optimal set for all of these parameters analytically. We, therefore, utilised an analytical model for the initial estimate of the parameter sets, and then our optimisation was based on evaluating the quality of the final reconstructed images obtained from Monte Carlo Simulation (MCS) data. The following sections will explain this process in more detail.

### 5.2.2 Analytical model

The analytical model was used for  $^{18}\text{F}$  (511 keV), and we only optimised the collimator for this energy, which lies inside the studied energy range (364 – 603 keV). For the initial optimisation, we used an analytical model which is based on the models in [11, 158] that can efficiently predict the performance of multi-pinhole SPECT and has been applied in optimising a small-animal SPECT system, namely U-SPECT-I [17], as well as in a theoretical analysis of a human brain SPECT [15]. It models collimator and detectors as spherical layers surrounding the scanned object (Figure 5.2(a)). The parameters used in this model are included in Table 5.1.

To approximate the cylindrical collimator and the triangularly-placed detectors in EXIRAD-HE by the spherical layers in the analytical model, the average distance from the pinholes' centres and the detector surface to the collimator's centre were set as the radius of the collimator layer ( $r_c$ ) and the radius of the detector layer ( $r_d$ ), respectively. To this end, we sampled uniformly on each detector's surface a set of  $50 * 50 = 2500$  points ( $\mathbf{D}$ ) from each of which a line was drawn through the collimator's centre. Intersections ( $\mathbf{C}$ ) of these lines with the cylindrical surface that goes through all pinholes' centres were calculated. Then,  $r_d$  (or  $r_c$ ) was set as the average distance from  $\mathbf{D}$  (or  $\mathbf{C}$ ) to the collimator's centre. Consequently,  $r_d$  was 278 mm as the detectors were fixed, and  $r_c$  depended on the real distance from pinholes' centres to the collimator centre (which is different for the various collimators we considered).

With the analytical model, we calculated the sensitivity over the whole CFOV instead of the peak sensitivity calculated at the collimator's centre as was done in [158]. To this end, we took the average of the sensitivities over  $n = 8820$  points uniformly distributed within the spherical CFOV. The sensitivity at each point reads [11]:

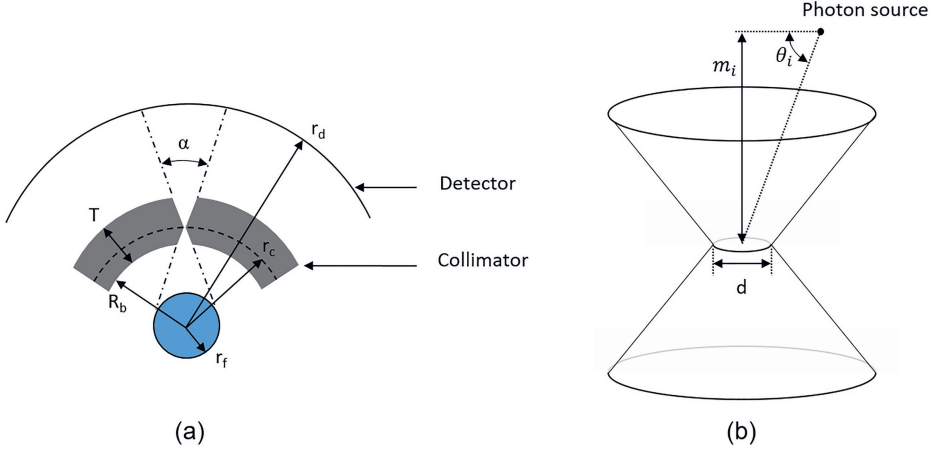


Figure 5.2: (a) Analytical model of the EXIRAD-HE. (b) Schematic sketch of a pinhole and a photon source for sensitivity calculation in Equation (5.1).

5

$$S_i = \frac{d^2 \sin^3 \theta_i}{16 m_i^2} + \frac{\sin^5 \theta_i \tan^2 \frac{\alpha}{2}}{8 m_i^2 \mu^2} \left( 1 - \frac{\cot^2 \theta_i}{\tan^2 \frac{\alpha}{2}} \right)^{\frac{1}{2}} * \left[ 1 - \frac{\cot^2 \theta_i}{\tan^2 \frac{\alpha}{2}} + \mu d \csc \theta_i \cot \frac{\alpha}{2} \right]. \quad (5.1)$$

where  $S_i$  is the sensitivity at photon source position  $i$ ;  $\theta_i$  and  $m_i$  define the location of the photon source (Figure 5.2(b));  $d$  is pinhole diameter;  $\alpha$  is pinhole opening angle;  $\mu$  is attenuation coefficient of the pinhole material. This average sensitivity was multiplied by the number of pinholes ( $N$ ), detector efficiency ( $\epsilon$ ), and then multiplied by two because of the gamma pair production, to obtain the system sensitivity over the CFOV:

$$S_{CFOV} = \frac{1}{n} \sum_i S_i * N * \epsilon * 2. \quad (5.2)$$

The number of pinholes was calculated as:

$$N = \frac{3 * D_X * D_Z * \pi/4}{\pi \left( \frac{r_d - r_c}{r_c} r_f \right)^2}. \quad (5.3)$$

This took into account that a fraction of  $\pi/4$  of the total detector surface ( $3 * D_X * D_Z$ ) is covered with non-overlapping pinhole projections. A detector photopeak efficiency  $\epsilon$  of 14.3% for 511 keV was obtained from MCS, as explained in Section 5.2.3. The radius of the CFOV ( $r_f$ ) is 2 mm.

Table 5.1: List of parameters in EXIRAD-HE.

Parameter	Description	Value
<b>h</b>	Distance from the pinhole's centre to the collimator's inner surface	<b>To be optimised</b>
<b>d</b>	Pinhole diameter	<b>To be optimised</b>
<b>T</b>	Wall thickness	<b>To be optimised</b>
$D_x, D_z$	Dimensions of each detector	497.4 mm, 410.6 mm
$R_b$	The radius of the collimator's bore	10.5 mm
$r_d$	The radius of the detector layer	278 mm
$r_c$	The radius of the collimator layer	Depends on <b>h</b>
$r_f$	The radius of the CFOV	2 mm
$\alpha$	Pinhole opening angle	$2^{\circ} \arcsin(r_f/r_c)$
<b>N</b>	Total number of pinholes	See Equation (5.3)
$\epsilon$	Detector efficiency	14.3%
$R_i$	Detector spatial resolution	3.5 mm
$\mu$	The attenuation coefficient of the pinhole material	See Table 5.2
$S_{CFOV}$	System sensitivity over the CFOV	Initially 0.30% and 0.60%

### 5.2.3 Monte Carlo simulations

#### General settings

Geant4 Application for Tomographic Emission (GATE) [76–79] was used for all MCS in this research to simulate photon transport inside the scanner. Our simulation method was validated with experimental data from EXIRAD-3D with a low-energy collimator in a previous publication (Chapter 2 [118]) where detailed settings can be found. In this work, to simulate the high-energy collimators, we adapted the following. Firstly, instead of manually defining the physics processes, here the “physic list builder” mechanism was used as recommended in the recent GATE documentation, and the general “emstandard” builder provided by the Geant4 community was set. This included, but was not limited to, photoelectric effect, Compton scattering, Rayleigh scattering, electron ionisation, bremsstrahlung, multiple scatter, and positron annihilation for positron emitters. Secondly, GATE’s “ion source” was defined by setting the isotope’s atomic number ( $Z$ ) and atomic weight ( $A$ ) (e.g.  $Z = 9$  and  $A = 18$  for a  $^{18}\text{F}$  source). This way, both the radioactive decay and the atomic de-excitation were incorporated, and it was straightforward to change the radioactive isotopes for different scan simulations. Finally, the detector’s spatial resolution and energy resolution were set in a different way than in [118]. The detector’s spatial resolution was fixed to 3.5 mm for all studied isotopes, instead of scaling it by the reciprocal of the square root of the photon’s energy which would result in a too good resolution for high energies because this way of scaling would not appropriately consider the large amount of scatter of the high-energy photons. The detector energy resolution was modelled using the inverse square law [76],  $R_{\text{energy}} = R_0 \sqrt{E_0/E}$ , where  $R_0 = 9\%$  was assumed as the full-width-at-half-maximum (FWHM) energy resolution at  $E_0 = 511$  keV.

After getting the projection images from the GATE output, realistic background radiation (from e.g. cosmic radiation) was added to both the photopeak window and the two side windows. This was based on the count rate from a background radiation measurement with a U-SPECT/CT system at MILabs B.V., Utrecht, the Netherlands, as reported in Table 5.2.

This table also specifies the photopeak window, the side windows, and some other settings for each isotope.

Table 5.2: Studied isotopes and corresponding simulation settings. The attenuation coefficient in collimator was obtained from NIST database [86, 87], and the attenuation coefficient in the detector was calculated from MCS (Section 5.2.3).

	<sup>18</sup> F	<sup>64</sup> Cu	<sup>124</sup> I	<sup>218</sup> Bi	<sup>134</sup> I
Half-life	1.83 h	12.7 h	4.18 d	45.59 m	8 d
Peak energy (keV)	511	511	603	440	364
Photopeak window (keV)	460-562	460-562	543-663	396-484	328-400
Side windows (keV)	434-460 562-588	434-460 562-588	513-543 663-693	374-396 484-506	309-328 400-419
Background radiation in photopeak window	81 cps	81 cps	80 cps	84 cps	98 cps
Background radiation in two side windows	40 cps	40 cps	38 cps	42 cps	41 cps
Detector spatial resolution (mm)	3.5	3.5	3.5	3.5	3.5
Detector energy resolution (%)	9.0	9.0	8.3	9.7	10.7
Attenuation coefficient in collimator (mm <sup>-1</sup> )	0.250	0.250	0.204	0.309	0.420
Attenuation coefficient in detector crystal (mm <sup>-1</sup> )	0.012	0.012	0.010	0.017	0.025

### Simulation of system sensitivity

The system sensitivity obtained from MCS was used in the collimator optimisation process to obtain pairs of **h** and **d** that would provide such sensitivity (Section 5.2.4). Here a uniform spherical <sup>18</sup>F distribution that exactly fits inside the CFOV (4-mm diameter) and emits 10<sup>8</sup> positrons was simulated. The activity distribution was placed at the centre of a PMMA sphere having a diameter of 10 mm that acts as the annihilation environment. Sensitivity was calculated as the number of detected counts within the photopeak window (20%) over the number of emissions. Note that all the sensitivities reported in this work were for <sup>18</sup>F.

### Simulation of detector efficiency

The detector efficiency was used in the analytical model. To simulate this, a uniform spherical <sup>18</sup>F source that fits in the CFOV and emits 10<sup>8</sup> positrons was placed at the centre of a full multi-pinhole collimator (**h** = 8 mm, **d** = 0.27 mm, and **T** = 60 mm). The activity distribution was placed at the centre of a PMMA sphere having a diameter of 10 mm that acts as the annihilation environment. By setting the detector's material as NaI with a normal density (3.67 g/cm<sup>3</sup>) and then with a very high density (367000 g/cm<sup>3</sup>), and taking the ratio between the counts in these two cases, we obtained a detector efficiency of 14.3% for 511 keV.

### Simulation of attenuation coefficient in detector crystal

The attenuation coefficient in the detector was simulated for each isotope and used both in the analytical model (Section 5.2.2) and in generating the system matrix for image reconstruction (Section 5.2.5). To this end, a point source containing the studied isotope that

emits  $10^5$  photons in a beam perpendicular to one of the 9.5-mm-thick NaI(Tl) scintillators was simulated. No collimator was included, and the beam was defined in GATE by the source's emission angle. Only for this simulation, the source was defined with gamma particle type and the corresponding mono-energy instead of the ion type. Subsequently, the attenuation coefficient was calculated with Equation (5.4), and the obtained numbers are listed in Table 5.2. This equation assumed Beer's law that did not fully include the Compton scatter (only the part that ends up being detected in the photopeak was considered); however, it provided an effective attenuation coefficient that we need for the analytical model and the system matrix generation.

$$\mu_{detector} = -\frac{1}{9.5} \log \left( 1 - \frac{\text{number of detected photons}}{10^5} \right). \quad (5.4)$$

## 5.2.4 Collimator optimisation and evaluation procedure

We here optimised the collimator for  $^{18}\text{F}$  because 511 keV lies near the middle of the studied energy range (364 – 603 keV) and we aimed to attain a collimator that can be used for a wide energy range. The optimisation procedure was as follows:

- (i) First, we assumed  $T = 60$  mm which is significantly larger than the thickness of the available low-energy collimator for EXIRAD-3D (25.5 mm) to prevent collimator wall penetration by the high-energy photons. The probability that 511 keV photons pass through a 60-mm-thick collimator material of 97% W, 1.5% Ni, and 1.5% Fe is  $3.1 \times 10^{-5}\%$ .
- (ii) For a fixed sensitivity averaged over the CFOV ( $S_{CFOV}$ ) of either 0.30% (sensitivity of an available *in vivo* high-energy collimator (HE-UHR-M) in VECTor [34]) or double that, 0.60%,  $\mathbf{h}$  was varied from 0 mm to 10 mm with a step size of 2 mm and the corresponding  $\mathbf{d}$  to achieve the desired sensitivity was roughly calculated with an analytical model as explained in Section 5.2.2. Subsequently,  $\mathbf{d}$  was fine-tuned with a step size of 5  $\mu\text{m}$  using MCS (see Section 5.2.3) to match the sensitivity exactly.
- (iii) The combinations of  $\mathbf{h}$  and  $\mathbf{d}$ , each defining a unique collimator, were used to create complete multi-pinhole collimators with the pinhole projections illustrated in Figure 5.3. The pinholes were distributed into rings, and in each ring, the axes between adjacent pinholes made an angle equal to the pinhole opening angle. The angular shift between adjacent rings was half the pinhole opening angle. The distances between the rings were set manually.
- (iv) The collimators were then evaluated at fixed  $S_{CFOV}$  based on full image reconstruction of a Derenzo phantom with a realistic activity concentration of  $^{18}\text{F}$  (described in Section 5.2.5). For each  $S_{CFOV}$ , the value of  $\mathbf{h}$  that results in the reconstructed Derenzo image with the highest contrast-to-noise ratio (CNR, Equation (5.5)) was selected.

- (v) For each  $S_{CFOV}$  with the chosen set of  $\mathbf{h}$  and  $\mathbf{d}$ , the wall thickness  $\mathbf{T}$  was reduced from 60 mm to 50 mm, 43 mm, and 30 mm to see which thickness still maintains good reconstructed image quality. To this end, we simulated both a Derenzo phantom and a uniform phantom (described in Section 5.2.5) with a realistic  $^{18}\text{F}$  activity concentration. The image quality was based on visual assessment, and quantitative metrics (CNR calculation for the Derenzo phantom, and portion of reconstructed activity present outside the uniform phantom).
- (vi) Finally, we obtained an optimised collimator for each  $S_{CFOV}$ , defined by a set of  $\mathbf{h}$ ,  $\mathbf{d}$ , and  $\mathbf{T}$ , and the estimated collimator weights, as well as the updated sensitivities for the finally chosen wall thickness, were recorded.

Subsequently, two collimator designs selected for the two considered sensitivities were evaluated with high concentrations of  $^{18}\text{F}$  and biologically realistic activities of some other high-energy isotopes, namely  $^{64}\text{Cu}$ ,  $^{124}\text{I}$ ,  $^{213}\text{Bi}$ , and  $^{131}\text{I}$ , to see which spatial resolution can be achieved. For comparison, simulations with the *in vivo* collimator HE-UHR-M in the VECTor system [34] having a pinhole diameter of 0.7 mm were added to see how much resolution gain the new EXIRAD-HE collimators offers.

Furthermore, a digital mouse knee joint phantom and a digital tumour xenograft phantom (described in Section 5.2.5) were simulated to evaluate the collimators' performance in tissue scans. The reconstructed images with the new collimators were also compared with those obtained with the HE-UHR-M collimator and 1-mm-blurred images of the original activity distribution that represents typical images of commercial coincidence PET.

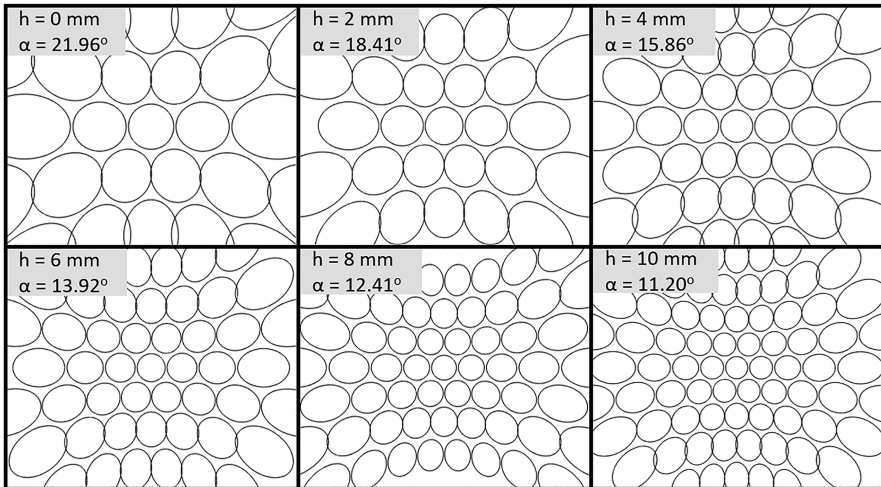


Figure 5.3: Geometric projection on one of the detectors with the manually placed pinholes for varying distance from pinhole centres to the collimator inner surface ( $h$ ). The indicated opening angle for each  $h$  is for the pinholes in middle rings. The opening angle of the pinholes in the two outermost rings is two degrees smaller than that to prevent projection overlapping.

### 5.2.5 Image reconstruction

#### General settings

All studied scans were simulated with MCS. In each scan, the object was placed at multiple bed positions and the projections acquired from all bed positions were used together in image reconstruction [32]. For image reconstruction, a system matrix was generated for each of the investigated collimators, using the ray-tracing method as described in [36]. In this method, the system matrix was calculated given the position and orientation of the collimators and detectors, as well as the energy-dependent linear attenuation coefficients of the collimator and detector materials. The system matrix for each isotope was generated at the energy of the chosen photopeak (Table 5.2). To keep a reasonable matrix size and reconstruction time, only the gamma photon paths that have a probability of at least 1% to pass through the collimator material are included into the system matrix. Reconstructions were performed using the similarity-regulated ordered-subset expectation maximisation (SROSEM) algorithm [53]. Post-filtering was applied with the filter size indicated for each phantom. Images were reconstructed on an isotropic 0.25-mm-voxel grid. Scatter and background radiation were corrected using the triple-energy window method [94] with two side windows adjacent to the photopeak, each having a width of 25% of the photopeak window's width. Positron range was corrected by including it in the forward step of the reconstruction using pre-calculated kernels [36]. Note that positron range correction was not applicable for  $^{124}\text{I}$ ,  $^{213}\text{Bi}$ , and  $^{131}\text{I}$  for the corresponding acquired photopeaks.

#### Digital Derenzo phantoms

Two Derenzo phantoms simulated in this work are shown in Figure 5.4. Derenzo phantom 1 was used most of the time, and Derenzo phantom 2 was only for the  $^{131}\text{I}$  scan in Figure 5.7 to show smaller rods. Each phantom has six sectors, in each of which, the distance between centres of two adjacent rods was twice the rod diameter. The whole phantom was placed at the centre of a PMMA cylinder having a diameter of 14 mm and a length of 8 mm.

Various activities in the phantoms and scan times were assumed for the collimator optimisation and evaluation. We simulated biologically realistic activity concentration in mice of  $^{18}\text{F}$  (4.39 MBq/ml),  $^{64}\text{Cu}$  (9 MBq/ml),  $^{124}\text{I}$  (9.6 MBq/ml),  $^{213}\text{Bi}$  (12.4 MBq/ml),  $^{131}\text{I}$  (54 MBq/ml) that were retrieved from [40, 159–162]. Higher  $^{18}\text{F}$  activities (20 MBq/ml and 60 MBq/ml), which can be of interest in *ex vivo* imaging, were also tested. The scan time was set to 4 hours for  $^{18}\text{F}$ , 1 hour for  $^{213}\text{Bi}$ , and 16 hours for  $^{64}\text{Cu}$ ,  $^{124}\text{I}$ , and  $^{131}\text{I}$  considering the isotopes' half-lives (see Table 5.2).

Data acquisition with sixteen bed positions was simulated for this phantom. The images that were shown had the iteration number and the 3D Gaussian post-filter that maximised the CNR. The CNR was calculated in the same way as in [37]. For this purpose, we drew the activity regions (red circle) and the background regions (blue circles) as indicated in Figure 5.4 that span a depth of 1.5 mm (or six slices). CNR was defined as:

$$CNR = \frac{1}{n_s} \sum_s \frac{\bar{I}_s - \bar{B}_s}{\bar{I}_s} \bigg/ \frac{\sqrt{\sigma_{I_{s,p}}^2 + \sigma_{B_{s,p}}^2}}{\bar{I}_s}, \quad (5.5)$$

where  $\bar{I}_s$  and  $\bar{B}_s$  are the mean intensity over the activity regions and the background regions of sector  $s$ , respectively.  $\sigma_{I_{s,p}}$  and  $\sigma_{B_{s,p}}$  are standard deviations over these regions, calculated on a subset of planes  $p$ ,  $p \in \{1, 3, 5\}$  to reduce covariance between planes.  $\bar{I}_s$  is mean intensity over all regions of interest in sector  $s$ , and  $n_s$  is the number of rod sectors. For EXIRAD-HE, all sectors were included, while for HE-UHR-M, only the three largest sectors were used in CNR calculation because the smaller sectors were not well resolved. The CNR's mean and standard deviation reported in Table 5.3 and Table 5.4 were calculated with three noise realisations, while the CNR for Figure 5.7 was from one realisation.

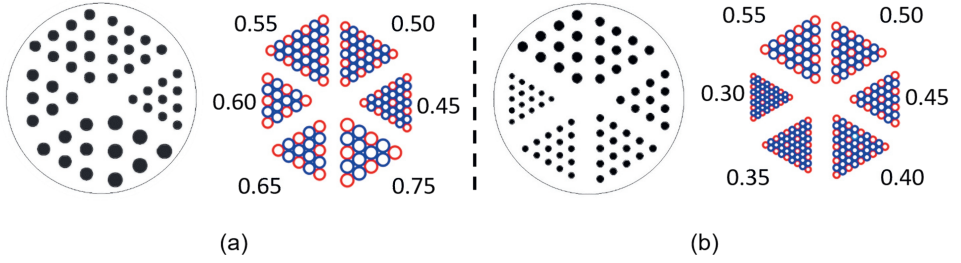


Figure 5.4: Derenzo phantoms with rod diameters in mm and the regions of interest for the CNR calculation. (a) Derenzo phantom 1. (b) Derenzo phantom 2.

### Digital uniform phantom

To study the wall thickness, a uniformly filled syringe (6.5 mm inner diameter and 10 mm length) was simulated. The whole phantom was placed at the centre of a PMMA cylinder having a diameter of 14 mm and a length of 14 mm. The phantom was assumed to contain 4.39 MBq/ml  $^{18}\text{F}$  and to have been scanned for 4 hours. Forty-five bed positions were used for this phantom. All the uniform phantom images were shown at the 10<sup>th</sup> iteration with the same post-reconstruction filters, a 0.7-mm-FWHM 3D Gaussian filter followed by a 7\*7\*7-voxels Median filter. Reconstructed image quality was evaluated based on visual assessment and the percentage of activity reconstructed outside the phantom.

### Digital mouse tissue phantoms

A mouse knee joint phantom was derived from a real 3D image of a mouse knee joint containing  $^{99m}\text{Tc}$ -methylene diphosphonate ( $^{99m}\text{Tc}$ -MDP) scanned with the low-energy EXIRAD collimator, and here assumed to contain  $^{18}\text{F}$ -Na as these isotopes label the same target in the bone. The mouse knee joint contained 56 MBq/ml  $^{18}\text{F}$  (obtained from experimental data with  $^{18}\text{F}$ ) and has been scanned for 4 hours. This phantom volume had a size of 4.45\*4.45\*6.45 mm<sup>3</sup>, and three bed positions were used.

Furthermore, a tumour xenograft phantom consisting of a large tumour with a necrotic core, and two small spherical tumours next to each other was simulated to contain  $^{131}\text{I}$ -NaI. The mouse was assumed to be injected with 20 MBq  $^{131}\text{I}$  and 10.2% ID/g was on the tumour at the time of termination [163]. The xenograft was presumed to be snap-frozen and imaged for 16 hours. This phantom volume had a size of  $6.25 \times 6.25 \times 6.25 \text{ mm}^3$ , and five bed positions were used.

In both cases, the reconstructed images were displayed at the iteration number and the 3D Gaussian filter size that yielded the lowest normalised mean-squared error (NMSE) and evaluated based on both visual assessment and NMSE.

## 5.3 Results

### 5.3.1 Collimator optimisation

Figure 5.5 compares reconstructed images of Derenzo phantom 1 when varying  $h$ . The pinhole diameters  $d$  that result in the desired system sensitivities and the image CNRs are reported in Table 5.3. “N/A” represents the case in which no non-negative value of  $d$  can be found to achieve the target  $S_{\text{CFOV}}$ . This was also the case when setting  $h = 0 \text{ mm}$ . For both sensitivity levels,  $h = 8 \text{ mm}$  offered the images with the highest CNR and was hence selected.

5

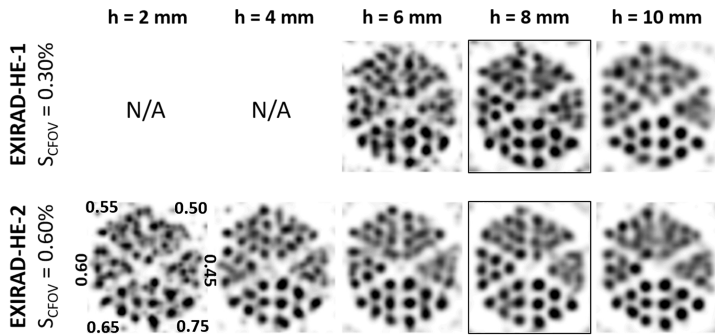


Figure 5.5: Images of Derenzo phantom 1 filled with 4.39 MBq/ml  $^{18}\text{F}$  and scanned for 4 hours for the optimisation of  $h$  and  $d$ . Each image was obtained with one collimator and displayed with the iteration and the 3D Gaussian filter size that maximises the CNR. The optimal image for each sensitivity is enclosed in a square box. Slice thickness was 1.5 mm.

Figure 5.6 shows the reconstructed images of Derenzo phantom 1 and the uniform phantom when varying wall thickness, and Table 5.4 presents the corresponding CNRs of the Derenzo images as well as the percentage of activity reconstructed outside the uniform. Visual assessment on the Derenzo phantom’s rods and on the activity within the uniform phantom volume does not show significant image degradation as the wall thickness reduces from 60 mm to 30 mm. However, the artefacts outside the uniform phantom do increase, especially

Table 5.3: The obtained values of **d** to achieve the desired system sensitivities and the CNRs from three realisations, represented as mean  $\pm$  standard deviation, for the corresponding values of **h**.

<b>h</b> (mm)		2	4	6	8	10
$S_{CFOV} = 0.30\%$	<b>d</b> (mm)	N/A	N/A	0.160	<b>0.270</b>	0.305
	CNR			$0.96 \pm 0.04$	<b><math>1.77 \pm 0.06</math></b>	$1.10 \pm 0.04$
$S_{CFOV} = 0.60\%$	<b>d</b> (mm)	0.135	0.385	0.505	<b>0.595</b>	0.620
	CNR	$0.50 \pm 0.07$	$1.38 \pm 0.04$	$1.77 \pm 0.06$	<b><math>2.02 \pm 0.05</math></b>	$1.96 \pm 0.03$

for the 30-mm thick collimator. Table 5.4 indicates that as the collimator wall gets thinner, the CNR decreases and the activity reconstructed outside the uniform phantom increases with the most degradation when going from 43 mm to 30 mm. Therefore, we chose **T** = 43 mm to keep a reasonable collimator weight of 16 kg for the core. The weight variation between the collimators for the two sensitivities is negligible because only pinhole diameters change (0.270 mm versus 0.595 mm).

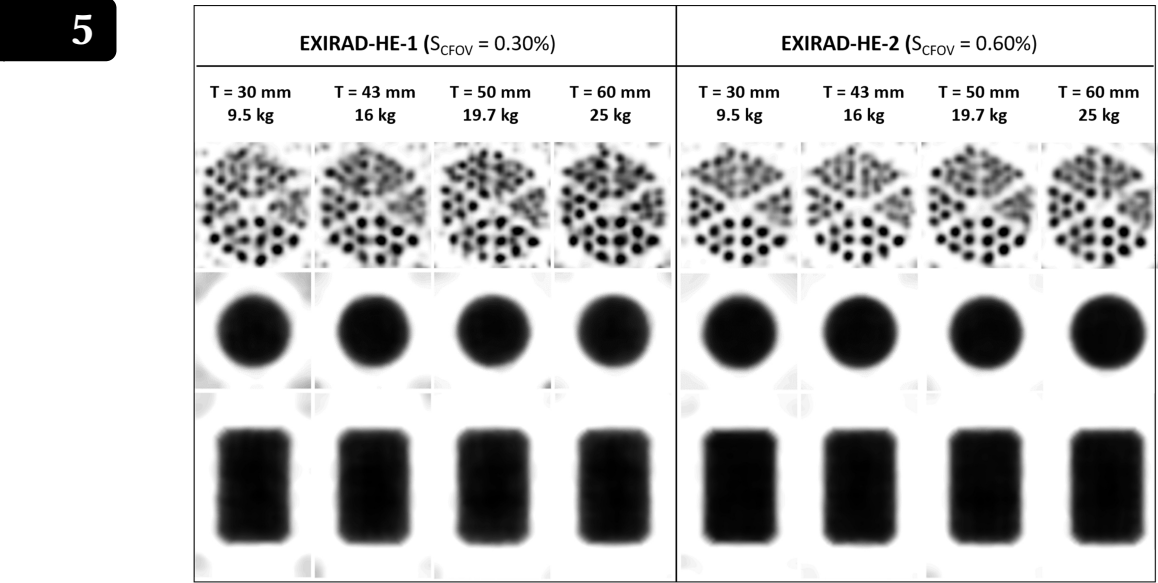


Figure 5.6: Reconstructed images of the Derenzo phantom 1 and the uniform phantom, both filled with 4.39 MBq/ml  $^{18}\text{F}$  and scanned for 4 hours, for the optimisation of **T**. Here the value of **h** was already fixed to 8 mm. Note that the listed sensitivities are only for **T** = 60 mm and we would expect slightly higher sensitivities for the smaller wall thicknesses. The Derenzo images were displayed with the iteration and the 3D Gaussian filter size that maximises the CNR. All the uniform phantom images were shown at the 10<sup>th</sup> iteration with the same post-reconstruction filters, 0.7-mm-FWHM 3D Gaussian filter +  $7*7*7$ -voxels Median filter. Slice thickness was 1.5 mm.

Table 5.5 presents the final parameters of the two optimal collimators, EXIRAD-HE-1 and EXIRAD-HE-2, with reference to the HE-UHR-M collimator. It turns out that EXIRAD-HE-1 and EXIRAD-HE-2 are only different in the pinhole diameter, which leads to the different system sensitivities. The listed sensitivities of the EXIRAD-HE collimators here were

Table 5.4:  $A_{outside}$  stands for the percentage of reconstructed activity outside uniform phantom relative to the total activity. Note that the listed sensitivities are for  $T = 60$  mm.

$T$ (mm)		30	43	50	60
$S_{CFOV} = 0.30\%$	CNR	$1.58 \pm 0.02$	<b><math>1.52 \pm 0.07</math></b>	$1.59 \pm 0.26$	$1.77 \pm 0.06$
	$A_{outside}$	26.7%	<b>15.6%</b>	13.6%	10.3%
$S_{CFOV} = 0.60\%$	CNR	$1.88 \pm 0.01$	<b><math>1.92 \pm 0.18</math></b>	$1.93 \pm 0.11$	$2.02 \pm 0.05$
	$A_{outside}$	18.8%	<b>12.6%</b>	11.0%	9.1%

Table 5.5: Parameters of the selected EXIRAD-HE collimators and reference to the HE-UHR-M collimator in VECTor which was also simulated in this work for comparison. For each collimator, two angles are listed: the larger one is for the inner rings, and the smaller one is for the two outermost rings near two ends of the collimator.

	EXIRAD-HE-1	EXIRAD-HE-2	HE-UHR-M
$S_{CFOV}$ (%)	0.312	0.617	0.30
$r_f$ (mm)	2	2	6
$h$ (mm)	8	8	8
$d$ (mm)	0.270	0.595	0.70
$T$ (mm)	43	43	43
$\alpha$ (degree)	12.41, 10.41	12.41, 10.41	18, 16
$N$	177	177	162
Number of rings	7 rings	7 rings	4 clustered-rings

calculated with  $^{18}\text{F}$  and the chosen wall thickness ( $T = 43$  mm), which are now slightly higher than the initially targeted sensitivities set at the beginning of the optimisation process.

### 5.3.2 Evaluation with digital Derenzo phantoms

Figure 5.7 displays simulated images of the Derenzo phantoms filled with  $^{18}\text{F}$  at several activity concentrations as well as some other high-energy isotopes using the optimal collimators. These reconstructed images are placed next to the images obtained with the *in vivo* collimator HE-UHR-M in VECTor to see the benefit of the new *ex vivo* collimator. Each column corresponds to a scan with a fixed setup, and only the collimator is changed. The image that shows the clearest rods in each scan is enclosed in a box. Here only the scans with  $^{131}\text{I}$  used the smaller phantom, Derenzo phantom 2, to visualise rods with smaller sizes.

In all of the investigated scans, the two EXIRAD-HE collimators clearly offer better images than the HE-UHR-M collimator. Comparing between EXIRAD-HE-1 and EXIRAD-HE-2, in some scans, the higher-sensitivity collimator performs better, while in the other scans the lower-sensitivity design offers superior images. That is understandable since, with relatively low radioactivity, we would choose a high-sensitivity collimator to acquire more counts that benefit image quality, and if the radioactivity is already relatively high, a

high-resolution collimator will offer a better image resolution.

The achievable spatial resolutions, defined by the diameters of the smallest visible rods, are 0.5 mm, 0.6 mm, 0.5 mm, 0.6 mm, and 0.35 mm for  $^{18}\text{F}$ ,  $^{64}\text{Cu}$ ,  $^{124}\text{I}$ ,  $^{213}\text{Bi}$ , and  $^{131}\text{I}$  imaging, respectively.

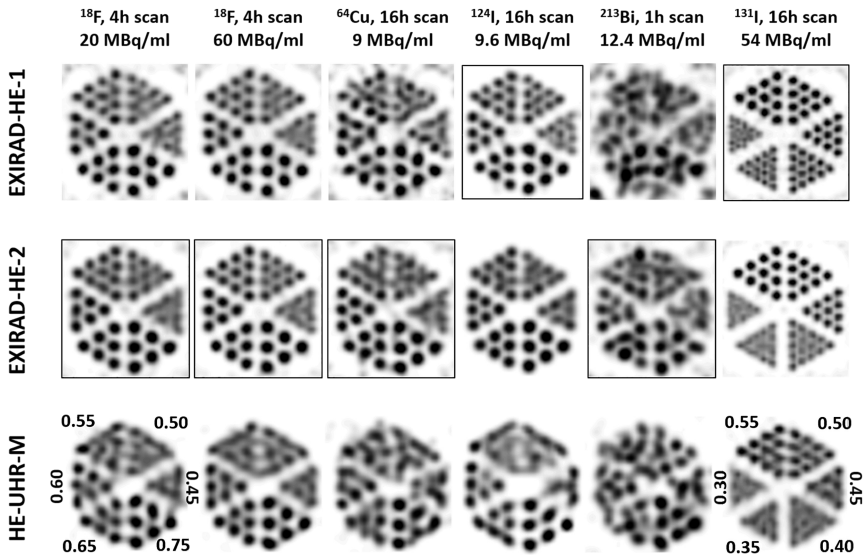


Figure 5.7: Simulated images of the Derenzo phantoms with  $^{18}\text{F}$  at several activity levels as well as with some other high-energy isotopes using the optimal collimators in Table 5.5. Only the  $^{131}\text{I}$  scan (rightmost column) was simulated with a smaller Derenzo phantom to visualise rods with smaller diameters. The images were displayed with the iteration and the 3D Gaussian filter size that maximises CNR. However, maximising CNR was visually suboptimal for  $^{213}\text{Bi}$  and  $^{131}\text{I}$  scans with EXIRAD-HE, so the iteration number and the filter size were chosen manually for these cases. In each column, the performance of the three collimators is compared, and the image that shows the clearest rods is enclosed in a square box. Slice thickness was 1.5 mm.

### 5.3.3 Evaluation with digital mouse tissue phantoms

Figure 5.8 and Figure 5.9 demonstrate the performance of the new collimators in imaging a mouse knee joint containing  $^{18}\text{F}$ -NaF, and a tumour xenograft containing  $^{131}\text{I}$ -NaI, respectively. In both cases, EXIRAD-HE resolves more details than HE-UHR-M. The xenograft image obtained with the HE-UHR-M collimator shows a smaller necrotic core of the central tumour than the actual shape, an unclear separation between the central tumour and the smaller tumours, and the invisibility of the smallest tumour. With the EXIRAD-HE collimators, the whole reconstructed shape of the xenograft is very close to that of the true phantom, and each of the tumours can be recovered with great detail. EXIRAD-HE-1 performs better than EXIRAD-HE-2 in the knee joint scan, while EXIRAD-HE-2 yields an image with clearer shape of the tumours than EXIRAD-HE-1 does in the xenograft scan. These results agree with the NMSE as reported in the legends of Figure 5.8 and Figure 5.9.

In both cases, the 1-mm-blurred images of the phantom offer significantly less detail than the images with EXIRAD-HE and HE-UHR-M.

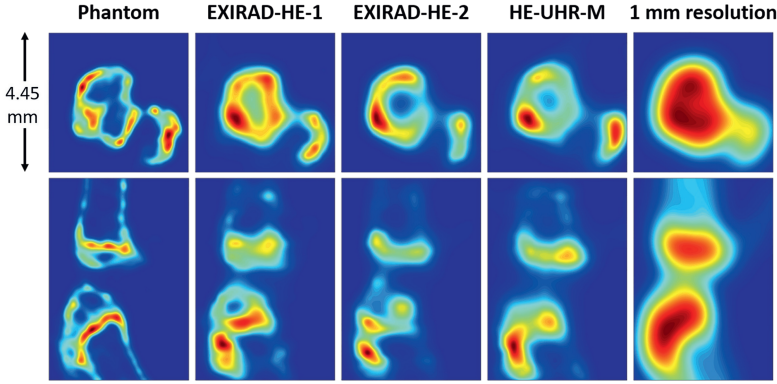


Figure 5.8: Simulation of a mouse knee joint phantom with the optimal collimators (Table 5.5) in comparison with the HE-UHR-M collimator in VECTor and the 1-mm-blurred image of the phantom. The images are shown at the iteration number that gives the lowest NMSE. The optimal NMSE is 0.17, 0.18, and 0.25 for EXIRAD-HE-1, EXIRAD-HE-2, and HE-UHR-M, respectively. Slice thickness was 0.5 mm.

## 5.4 Discussion

We have introduced two multi-pinhole collimators for *ex vivo* imaging of high-energy isotopes. Both collimators have shown, in various simulated scans, superior image resolution to the *in vivo* multi-pinhole SPECT/PET. The new collimators yielded a resolution of 0.5 mm, 0.6 mm, 0.5 mm, 0.6 mm, and 0.35 mm for  $^{18}\text{F}$ ,  $^{64}\text{Cu}$ ,  $^{124}\text{I}$ ,  $^{213}\text{Bi}$ , and  $^{131}\text{I}$ , respectively at realistic activity concentration levels. We believe that these resolution gains are important in many applications. For example, in a mouse scan with Fluorodeoxyglucose to detect the reduction in posterior cingulate activity – a sign for Alzheimer’s disease, a resolution of 0.5 mm is on the verge of being possible to detect this effect, and a resolution of 0.75 mm or worse fails to detect significantly abnormal activity [164]. Besides, the 1-mm-resolution images presented in Figure 5.8 and Figure 5.9 emphasise that sub-mm resolutions can reveal a lot of extra details.

These achievable resolutions with EXIRAD-HE for the PET isotopes  $^{18}\text{F}$  and  $^{64}\text{Cu}$  are probably already near the fundamental limit because of the positron range effect [165]. The average positron ranges of  $^{18}\text{F}$  and  $^{64}\text{Cu}$  in water are 0.64 mm and 0.56 mm, respectively [166]. This effect is not present if we utilise prompt gammas from non-pure positron emitters or single gammas from isotopes like  $^{213}\text{Bi}$  or  $^{131}\text{I}$  for imaging; therefore, EXIRAD-HE is most suitable for such isotopes. Besides, for sufficiently long half-life isotopes, the scan duration could be extended as the tissue sample is kept frozen over the course of the scan for good image quality.

Considering the manufacturing feasibility, the proposed EXIRAD-HE collimators only

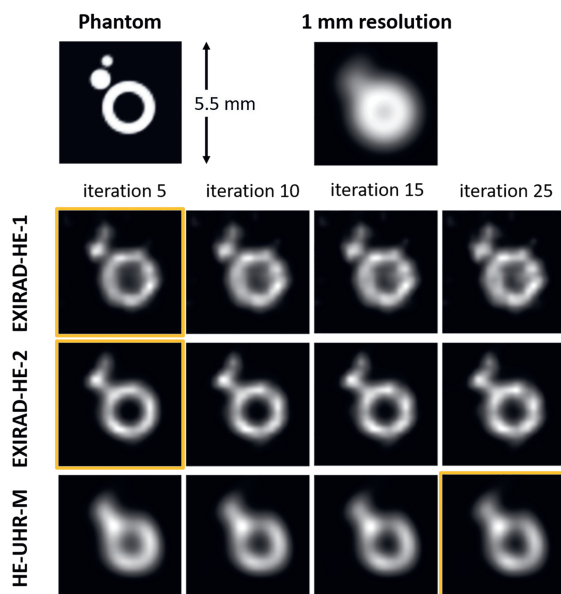


Figure 5.9: Simulation of a mouse tumour xenograft phantom with the optimal collimators (Table 5.5) in comparison with the HE-UHR-M collimator in VECtor and the 1-mm-blurred image of the phantom. Images are shown at several iteration numbers, and the images with the lowest NMSE are enclosed in boxes. The optimal NMSE is 0.05, 0.03, and 0.12 for EXIRAD-HE-1, EXIRAD-HE-2, and HE-UHR-M, respectively. Slice thickness was 0.5 mm.

consist of round pinholes with no shielding outside as is present for the low-energy EXIRAD collimator [118]. Adding a trapezium-hole shielding, we would be able to place the pinholes of the same opening angle slightly tighter, which translates into more pinholes without the cost of projection overlapping. Even though each pinhole will be truncated, the overall system sensitivity is expected to slightly increase for the same system resolution. However, the manufacturing complexity and cost will increase significantly because of the large number of narrow trapezium holes in this shielding.

As seen in Figures 5.7 to 5.9, each of the two proposed collimators has certain advantages, and the choice between them depends on the imaging situation. For relatively low activity levels, one may prefer the higher-sensitivity collimator for higher counts whereas when the count level is sufficient, the lower-sensitivity collimator would be selected for optimal image resolution.

## 5.5 Conclusion

This chapter presented the design, optimisation, and evaluation of new multi-pinhole collimators for *ex vivo* 3D tomographic imaging of high-energy isotopes. We found that placing pinhole centres at a distance of 8 mm from the collimator inner surface yielded optimal image resolution for fixed system sensitivity over the CFOV. A wall thickness of

43 mm that keeps a reasonable weight (16 kg for the core) still maintains excellent image quality compared to a wall thickness of 60 mm (25 kg for the core). With the two optimal high-energy collimators, the system offers a resolution of 0.35 mm, 0.6 mm, 0.5 mm, 0.6 mm, and 0.5 mm when imaging  $^{131}\text{I}$ ,  $^{213}\text{Bi}$ ,  $^{18}\text{F}$ ,  $^{64}\text{Cu}$ , and  $^{124}\text{I}$ , respectively, contained in tissue samples.

## Acknowledgements

The authors would like to thank Ruud Ramakers (MILabs B.V.) for providing the experimental activity concentration of  $^{18}\text{F}$ -Na in the mouse knee, and the background radiation measurement data.



## Chapter 6

### Thesis conclusion

The use of a multi-pinhole collimator helps to achieve ultra-high resolution imaging of gamma and positron emitters (SPECT and PET), especially in preclinical applications. *In vivo* resolution is dependent on the animal size because this size is the factor limiting how close pinholes can be placed to the activity distribution in order to achieve a high magnification and good sensitivity. A higher resolution than what can currently be achieved *in vivo* is still desirable. *Ex vivo* scanning of small tissue samples is a straightforward way to increase the resolution. The aim of this thesis is to develop and validate *ex vivo* nuclear molecular imaging modules for the available preclinical U-SPECT and VECTor systems for a broad energy range. From an existing design of a dedicated multi-pinhole collimator for *ex vivo* SPECT with low- and mid-energy isotopes (EXIRAD-3D, MILabs B.V.), different materials were evaluated for the collimator using Monte Carlo simulations. Then, a fabricated EXIRAD-3D collimator was experimentally characterised to test its performance. Further development in terms of system modelling for image reconstruction was presented for EXIRAD-3D, but the presented method can also be applied to other multi-pinhole SPECT systems. In addition, two new collimators for *ex vivo* imaging of high-energy isotopes (EXIRAD-HE) were designed and optimised in this thesis.

In **Chapter 2**, the use of different collimator materials has been studied for EXIRAD-3D using Monte Carlo simulations. Starting from the existing design of the EXIRAD-3D collimator (0.15-mm pinhole diameter, 92.5% tungsten alloy), the collimator's material was set to either lead, tungsten, gold, or depleted uranium, while keeping the system sensitivity unchanged by adjusting the pinhole diameter. For different materials, we compared PSFs and Derenzo resolution phantom images based on a visual assessment as well as a contrast-to-noise ratio (CNR) analysis. The studies were performed for a wide range of radioisotopes:  $^{125}\text{I}$  (27 keV),  $^{201}\text{Tl}$  (71 keV),  $^{99m}\text{Tc}$  (140 keV), and  $^{111}\text{In}$  (171 keV and 245 keV). The reliability of the Monte Carlo simulations was confirmed with an experimental scan on the real system. The simulation results showed that using materials with higher photon-stopping power yields images with CNR improved up to 36.6% compared to using lead. As suggested from the visual assessment on the reconstructed images, tungsten is generally a good choice for EXIRAD-3D collimator for a wide range of SPECT isotopes. For relatively high-energy isotopes such as  $^{111}\text{In}$ , using pinhole inserts made of gold can be beneficial. In terms of practical usage, tungsten alloy should be used instead of pure tungsten for easier casting, while either gold or platinum-gold alloy can be used. Besides, since gold is expensive, it should be used only for the pinhole inserts instead of the whole collimator; however, using

tungsten is still a more economical choice.

In **Chapter 3**, EXIRAD-3D with a collimator made of a 92.5% tungsten alloy for imaging low- and mid-energy isotopes was experimentally characterised to obtain its performance in various phantom scans and mouse knee joint, thyroid, and kidney scans. The phantom scans with  $^{99m}\text{Tc}$  demonstrated a 120  $\mu\text{m}$  spatial image resolution and good image uniformity. The results also showed that the reconstructed activity scales linearly with the activity present in the phantom. EXIRAD-3D visualised tiny details of bone turnover on many structures in the knee joint containing [ $^{99m}\text{Tc}$ ]MDP. It also provided a clear [ $^{123}\text{I}$ ]NaI SPECT image of the mouse thyroid that shows well-separated thyroidal lobes (about 2.5 mm long, 1.3 mm wide, and 0.6 mm deep), and even the thin isthmus (about 0.3 mm thick) connecting the two lobes. The [ $^{99m}\text{Tc}$ ]DMSA image of the mouse kidney accurately revealed the tracer distribution in the renal cortex. This is a good level of detail achieved with SPECT.

The EXIRAD-3D presented in **Chapter 3** already offered a great experimental performance; however, it can still be improved in terms of system modelling in image reconstruction. A new Fast Monte-Carlo based (FMC-based) matrix generation method was introduced in **Chapter 4** that addressed some challenges with the available system modelling methods used in our U-SPECT and VECTOR scanners (traditional method and ray-tracing method). The proposed method was evaluated with both experimental scans with  $^{99m}\text{Tc}$ ,  $^{111}\text{In}$ , and  $^{123}\text{I}$ , and Monte Carlo simulated scans with  $^{67}\text{Ga}$  and  $^{90}\text{Y}$ . Compared to the traditional method, the FMC-based method generalised better when the isotopes emit gamma photon energies different from the energy used in calibration, and it lessened the need of fabricating a very small activity point source (smaller than the image voxel size) which is difficult for EXIRAD-3D. Besides, the FMC-based method is computationally more efficient for EXIRAD-3D than the ray-tracing matrices. The proposed method also showed the advantage of being able to combine energies in a single matrix when imaging isotopes with multiple photopeak energies such as  $^{67}\text{Ga}$  or isotopes with a continuous energy spectrum such as  $^{90}\text{Y}$ . FMC is an efficient, accurate, and versatile tool for creating system matrices for not only EXIRAD-3D but also other pinhole SPECT systems.

Many available and emerging isotopes emit gammas with relatively high energies outside the conventional SPECT energy range (27–245 keV); PET tracer decay results in 511 keV annihilation photons, and many alpha or beta emitters used for theranostic applications co-emit high-energy gammas. Therefore, it is of interest to develop an EXIRAD option for imaging high-energy isotopes. **Chapter 5** presents the collimator design, optimisation, and evaluation for such an option called EXIRAD-HE. New collimators were designed using narrow-opening-angle pinholes and thick collimator walls. Full Monte Carlo simulations of a Derenzo phantom scan and a uniform phantom scan with  $^{18}\text{F}$  were performed to optimise the collimators such that the system offers the best resolution at two pre-determined system sensitivities. The optimal collimators were subsequently evaluated for a wide range of high-energy isotopes, namely  $^{18}\text{F}$ ,  $^{64}\text{Cu}$ ,  $^{124}\text{I}$ ,  $^{213}\text{Bi}$ , and  $^{131}\text{I}$  using both Derenzo phantoms and digital mouse knee joint and xenograft phantoms. The optimisation study suggests that placing pinhole centres at a distance of 8 mm from the collimator's inner surface yields optimal image resolution for fixed system sensitivity. A collimator wall thickness of 43 mm maintains the excellent image quality obtained with a 60 mm thick wall while keeping

the collimator core at a reasonable weight. Finally, the two best performing collimators for two different system sensitivities were further investigated. With these collimators, EXIRAD-HE achieves a spatial resolution of 0.35 mm, 0.6 mm, 0.5 mm, 0.6 mm, and 0.5 mm when imaging  $^{131}\text{I}$ ,  $^{213}\text{Bi}$ ,  $^{18}\text{F}$ ,  $^{64}\text{Cu}$ , and  $^{124}\text{I}$ , respectively.

Developing the EXIRAD modules based on the U-SPECT and VECTor systems has involved significant efforts. Not only dedicated multi-pinhole collimators with a small bore were developed, but also system modelling software was optimised for image reconstruction. Besides, a novel specialised cryo-cooling unit with sample holder, which was not priorly used for *in vivo* scans, has been created for EXIRAD. This cooler is often needed to keep tissue frozen throughout the scan to avoid tissue deformation and radioactivity leakage.

The presented *ex vivo* imaging modules achieved a measured resolution of 0.12 mm for medium-energy ( $^{99m}\text{Tc}$ ) and simulated resolutions of 0.35-0.6 mm for high-energy isotopes, which are significantly better than the resolutions obtained *in vivo*. In practice, compared to the *in vivo* workflow, the resolution gain with EXIRAD comes with relatively little additional effort except for dissecting and snap-freezing the tissues. For higher resolutions, traditional autoradiography would still be a common choice; however, autoradiography requires significantly more manual work to slice the tissue and image each slice. Besides, creating fully 3D images from those slices is still a difficult task because distortion and other artefacts are potentially present during the tissue slicing and image registration process, and because in common practice, not all sections can be collected due to limitations in time, labour, and laboratory resources. Therefore, EXIRAD can be a very efficient alternative for autoradiography in a subset of pharmaceutical and biological studies, especially as an option on a U-SPECT/CT or VECTor/CT system to facilitate longitudinal studies on the same animal and to provide a direct link between *in vivo* and *ex vivo* datasets.

As for possible further research on this topic, it would be interesting to fabricate the EXIRAD-HE collimators designed in this thesis for experimental scans. In addition, the FMC-based matrix generation method was well-validated for a wide range of radioisotopes (93 keV – 285 keV), but it would also be useful to know its performance for e.g. 511 keV ( $^{18}\text{F}$ ) or 909 keV ( $^{89}\text{Zr}$ ). For these high energies, the PSF fitting step in the FMC-based method can be challenging as it requires a more complex function than the Gaussian function currently used. Besides, FMC models some physics processes such as photon scatter better than the ray-tracer. The effect of this does not show clear advantages for the studied energy range; however, it may be significant for high energies. The detailed analysis of this would be interesting for future research.



# Bibliography

- [1] Martin Pomper, Henry VanBrocklin, and Carolyn Anderson. What is molecular imaging? *Journal of Nuclear Medicine*, 49(supplement 1), 2008.
- [2] Janet C Miller and James H Thrall. Clinical molecular imaging. *Journal of the American College of Radiology : JACR*, 1(1 Suppl):4–23, 2004.
- [3] A Signore, S J Mather, G Piaggio, | G Malviya, and R A Dierckx. Molecular Imaging of Inflammation/Infection: Nuclear Medicine and Optical Imaging Agents and Methods. 2010.
- [4] D. Alvarez-Fischer, G. Blessmann, C. Trosowski, M. Béhé, T. Schurrat, A. Hartmann, T. M. Behr, W. H. Oertel, G. U. Höglinger, and H. Höffken. Quantitative [123I]FP-CIT pinhole SPECT imaging predicts striatal dopamine levels, but not number of nigral neurons in different mouse models of Parkinson’s disease. *NeuroImage*, 38(1):5–12, oct 2007.
- [5] Jacqueline A. Gleave, Troy H. Farncombe, Chantal Saab, and Laurie C. Doering. Correlative single photon emission computed tomography imaging of [123I]altropane binding in the rat model of Parkinson’s. *Nuclear Medicine and Biology*, 38(5):741–749, jul 2011.
- [6] Sven R. Suwijn, Kora de Bruin, Rob M.A. de Bie, and Jan Booij. The role of SPECT imaging of the dopaminergic system in translational research on Parkinson’s disease. *Parkinsonism and Related Disorders*, 20(SUPPL.1):S184–S186, 2014.
- [7] Werner Poewe, Klaus Seppi, Caroline M. Tanner, Glenda M. Halliday, Patrik Brundin, Jens Volkmann, Anette Eleonore Schrag, and Anthony E. Lang. Parkinson disease. *Nature Reviews Disease Primers*, 3(1):1–21, mar 2017.
- [8] Andreas K. Buck, Stephan Nekolla, Sibylle Ziegler, Ambros Beer, Bernd J. Krause, Ken Herrmann, Klemens Scheidhauer, Hans Juergen Wester, Ernst J. Rummeny, Markus Schwaiger, and Alexander Drzezga. SPECT/CT, aug 2008.
- [9] Kooresh Shoghi-Jadid, Gary W. Small, Eric D. Agdeppa, Vladimir Kepe, Linda M. Ercoli, Prabha Siddarth, Stephen Read, Nagichettiar Satyamurthy, Andrej Petric, Sung Cheng Huang, and Jorge R. Barrio. Localization of neurofibrillary tangles and beta-amyloid plaques in the brains of living patients with alzheimer disease. *American Journal of Geriatric Psychiatry*, 10(1):24–35, jan 2002.
- [10] Freek J. Beekman, David P. McElroy, Frank Berger, Sanjiv S. Gambhir, Edward J. Hoffman, and Simon R. Cherry. Towards in vivo nuclear microscopy: Iodine-125 imaging

- in mice using micro-pinholes. *European Journal of Nuclear Medicine*, 29(7):933–938, 2002.
- [11] S. D. Metzler, J. E. Bowsher, M. F. Smith, and R. J. Jaszcak. Analytic determination of pinhole collimator sensitivity with penetration. *IEEE Transactions on Medical Imaging*, 20(8):730–741, 2001.
  - [12] S. D. Metzler, J. E. Bowsher, K. L. Greer, and R. J. Jaszcak. Analytic determination of the pinhole collimator’s point-spread function and RMS resolution with penetration. *IEEE Transactions on Medical Imaging*, 21(8):878–887, 2002.
  - [13] S D Metzler and R Accorsi. Resolution- Versus Sensitivity-Effective Diameter in Pinhole Collimation: Experimental Verification. *Physics in Medicine and Biology*, 50(21):5005–17, 2005.
  - [14] M C M Rentmeester, F van der Have, and F J Beekman. Optimizing multi-pinhole SPECT geometries using an analytical model. *Physics in medicine and biology*, 52(9):2567–81, 2007.
  - [15] M C Goorden, M C M Rentmeester, and F J Beekman. Theoretical analysis of full-ring multi-pinhole brain SPECT. *Physics in Medicine and Biology*, 54(21):6593–6610, nov 2009.
  - [16] Lars R. Furenlid, Donald W. Wilson, Yi Chun Chen, Hyunki Kim, Philip J. Pietraski, Michael J. Crawford, and Harrison H. Barrett. FastSPECT II: A second-generation high-resolution dynamic SPECT imager. *IEEE Transactions on Nuclear Science*, 51(3 II):631–635, jun 2004.
  - [17] Freek J Beekman, Frans van der Have, Brendan Vastenhouw, Annemarie J a van der Linden, Peter P van Rijk, J Peter H Burbach, and Marten P Smidt. U-SPECT-I: a novel system for submillimeter-resolution tomography with radiolabeled molecules in mice. *Journal of nuclear medicine : official publication, Society of Nuclear Medicine*, 46(7):1194–1200, 2005.
  - [18] Hyunki Kim, Lars R. Furenlid, Michael J. Crawford, Donald W. Wilson, H. Bradford Barber, Todd E. Peterson, William C.J. Hunter, Zhonglin Liu, James M. Woolfenden, and Harrison H. Barrett. SemiSPECT: A small-animal single-photon emission computed tomography (SPECT) imager based on eight cadmium zinc telluride (CZT) detector arrays. *Medical Physics*, 2006.
  - [19] Nils Schramm, John Hoppin, Christian Lackas, Flavio Forrer, Roelf Valkema, and Marion de Jong. *The NanoSPECT: A high-sensitivity multi-pinhole SPECT system with submillimeter (nanoliter) spatial resolution for imaging small rodents*, volume 47. Society of Nuclear Medicine, may 2006.
  - [20] Jacob Y. Hesterman, Matthew A. Kupinski, Lars R. Furenlid, Donald W. Wilson, and Harrison H. Barrett. The multi-module, multi-resolution system (M3R): A novel small-animal SPECT system. *Medical Physics*, 34(3):987–993, feb 2007.

- 
- [21] Frans van der Have, Brendan Vastenhouw, Ruud M. Ramakers, Woutjan Branderhorst, Jens O. Krah, Changguo Ji, Steven G. Staelens, and Freek J. Beekman. U-SPECT-II: An Ultra-High-Resolution Device for Molecular Small-Animal Imaging. *Journal of nuclear medicine : official publication, Society of Nuclear Medicine*, 50(4):599–605, mar 2009.
  - [22] Johan Nuyts, Kathleen Vunckx, Michel Defrise, and Christian Vanhove. Small animal imaging with multi-pinhole SPECT. *Methods*, 48(2):83–91, jun 2009.
  - [23] L. J. Meng, G. Fu, E. J. Roy, B. Suppe, and C. T. Chen. An ultrahigh resolution SPECT system for I-125 mouse brain imaging studies. *Nuclear Instruments and Methods in Physics Research, Section A: Accelerators, Spectrometers, Detectors and Associated Equipment*, 600(2):498–505, 2009.
  - [24] Reza Golestani, Chao Wu, René A Tio, Clark J Zeebregts, Artiom D Petrov, Freek J Beekman, Rudi A J O Dierckx, Hendrikus H Boersma, and Riemer H J A Slart. Small-animal SPECT and SPECT/CT: application in cardiovascular research. *European journal of nuclear medicine and molecular imaging*, 37(9):1766–77, aug 2010.
  - [25] F. Sánchez, A. Orero, A. Soriano, C. Correcher, P. Conde, A. González, L. Hernández, L. Moliner, M. J. Rodríguez-Alvarez, L. F. Vidal, J. M. Benlloch, S. E. Chapman, and W. M. Leevy. ALBIRA: A small animal PET/SPECT/CT imaging system. *Medical Physics*, 40(5):051906, apr 2013.
  - [26] M Peterson, S-E Strand, and M Ljungberg. Using the Alloy Rose’s Metal as Pinhole Collimator Material in Preclinical Small Animal Imaging: A Monte Carlo Evaluation. *Medical Physics*, 42(4):1698–1709, 2015.
  - [27] Oleksandra Ivashchenko, Frans van der Have, Jose L Villena, Harald C Groen, Ruud M Ramakers, Harrie H Weinans, and Freek J Beekman. Quarter-millimeter-resolution molecular mouse imaging with U-SPECT+. *Molecular imaging*, 13, 2014.
  - [28] A. Wouters, K. M. Simon, and J. G. Hirschberg. Direct Method of Decoding Multiple Images. *Applied Optics*, 12(8):1871, aug 1973.
  - [29] L T Chang, S N Kaplan, B Macdonald, V Perez-Mendez, and L Shiraishi. A method of tomographic imaging using a multiple pinhole-coded aperture. *Journal of nuclear medicine : official publication, Society of Nuclear Medicine*, 15(11):1063–5, nov 1974.
  - [30] R A Vogel, D Kirch, M LeFree, and P Steele. A new method of multiplanar emission tomography using a seven pinhole collimator and an Anger scintillation camera. *Journal of nuclear medicine : official publication, Society of Nuclear Medicine*, 19(6):648–54, jun 1978.
  - [31] R. K. Rowe, J. N. Aarsvold, H. H. Barrett, J. C. Chen, W. P. Klein, B. A. Moore, I. W. Pang, D. D. Patton, and T. A. White. A stationary hemispherical SPECT imager for three-dimensional brain imaging. *Journal of Nuclear Medicine*, 1993.
  - [32] Brendan Vastenhouw and Freek Beekman. Submillimeter total-body murine imaging with U-SPECT-I. *Journal of Nuclear Medicine*, 48(3):487–493, 2007.

- [33] Marlies C Goorden and Freek J Beekman. High-resolution tomography of positron emitters with clustered pinhole SPECT. *Physics in medicine and biology*, 55(5):1265–77, 2010.
- [34] M. C. Goorden, F. van der Have, R. Kreuger, R. M. Ramakers, B. Vastenhouw, J. P. H. Burbach, J. Booij, C. F. M. Molthoff, and F. J. Beekman. VECTOR: A Preclinical Imaging System for Simultaneous Submillimeter SPECT and PET. *Journal of Nuclear Medicine*, 54(2):306–312, feb 2013.
- [35] Freek J Beekman, Chris Kamphuis, Sofia Koustoulidou, Ruud M Ramakers, and Marlies C Goorden. Positron range-free and multi-isotope tomography of positron emitters. *Physics in Medicine & Biology*, feb 2021.
- [36] Marlies C Goorden, Jarno van Roosmalen, Frans van der Have, and Freek J Beekman. Optimizing modelling in iterative image reconstruction for preclinical pinhole PET. *Physics in medicine and biology*, 61(10):3712–33, 2016.
- [37] Matthew D Walker, Marlies C Goorden, Katherine Dinelle, Ruud M Ramakers, Stephan Blinder, Maryam Shirmohammad, Frans van der Have, Freek J Beekman, and Vesna Sossi. Performance Assessment of a Preclinical PET Scanner with Pinhole Collimation by Comparison to a Coincidence-Based Small-Animal PET Scanner. *Journal of nuclear medicine*, 55(8):1368–1374, 2014.
- [38] Freek J Beekman, Chris Kamphuis, Sofia Koustoulidou, Branden Vastenhouw, D Rendon, Ruud M Ramakers, S Blazis, S van Cauter, Marlies C Goorden, and Felix Gremse. VECTOR-6: Broadband photon tomography takes the versatility of multi-modality preclinical imaging beyond the limits of PET-SPECT-CT and Optical Imaging. In *WMIC 2018, Seattle, USA*, 2018.
- [39] Jan de Swart, Ho Sze Chan, Marlies C Goorden, Alfred Morgenstern, Frank Bruchertseifer, Freek J Beekman, Marion de Jong, and Mark W Konijnenberg. Utilizing High-Energy  $\gamma$ -Photons for High-Resolution  $^{213}\text{Bi}$  SPECT in Mice. *Journal of Nuclear Medicine*, 57(3):486–92, mar 2016.
- [40] Frans van der Have, Oleksandra Ivashchenko, Marlies C. Goorden, Ruud M. Ramakers, and Freek J. Beekman. High-resolution clustered pinhole  $^{131}\text{I}$  SPECT imaging in mice. *Nuclear Medicine and Biology*, 43(8):506–511, 2016.
- [41] J R Crawford, A K H Robertson, H Yang, C Rodríguez-Rodríguez, P L Esquinas, P Kunz, S Blinder, V Sossi, P Schaffer, and T J Ruth. Evaluation of  $^{209}\text{At}$  as a theranostic isotope for  $^{209}\text{At}$ -radiopharmaceutical development using high-energy SPECT. *Physics in Medicine & Biology*, 63(4):045025, feb 2018.
- [42] Marlies C Goorden, Chris Kamphuis, Ruud M Ramakers, and Freek J Beekman. Accelerated image reconstruction by a combined dual-matrix dual-voxel approach. *Physics in Medicine & Biology*, 65(10):105014, 2020.
- [43] Eric G. Solon. Autoradiography techniques and quantification of drug distribution. *Cell and Tissue Research*, 360(1):87–107, 2015.

- 
- [44] M S Al-Tikriti, H M Dey, S S Zoghbi, R M Baldwin, Y Zea-Ponce, and R B Innis. Dual-isotope autoradiographic measurement of regional blood flow and benzodiazepine receptor availability following unilateral middle cerebral artery occlusion. *Eur J Nucl Med*, 21(3):196–202, 1994.
  - [45] Walter E. Stumpf. Whole-body and microscopic autoradiography to determine tissue distribution of biopharmaceuticals - Target discoveries with receptor micro-autoradiography engendered new concepts and therapies for vitamin D. *Advanced Drug Delivery Reviews*, 65(8):1086–1097, 2013.
  - [46] Andrew McEwen and CLaire Henson. Quantitative whole-body autoradiography: past, present and future. *Bioanalysis*, 7(5):557–568, 2015.
  - [47] RJ Hargreaves, J Hoppin, J Sevigny, S Patel, P Chiao, M Klimas, and A Verma. Optimizing Central Nervous System Drug Development Using Molecular Imaging. *Clinical Pharmacology & Therapeutics*, 98(1):47–60, jul 2015.
  - [48] Philippe P. Bruyant. Analytic and iterative reconstruction algorithms in SPECT. *Journal of Nuclear Medicine*, 2002.
  - [49] K. Lange and R. Carson. EM reconstruction algorithms for emission and transmission tomography. *Journal of Computer Assisted Tomography*, 1984.
  - [50] L a Shepp and Y Vardi. Maximum likelihood reconstruction for emission tomography. *IEEE transactions on medical imaging*, 1(2):113–122, 1982.
  - [51] H Malcolm Hudson and Richard S Larkin. Accelerated Image Reconstruction Using Ordered Subsets of Projection Data. *IEEE transactions on medical imaging*, 13(4):601–609, 1994.
  - [52] Woutjan Branderhorst, Brendan Vastenhouw, and Freek J Beekman. Pixel-based subsets for rapid multi-pinhole SPECT reconstruction. *Physics in medicine and biology*, 55(7):2023–2034, 2010.
  - [53] P E B Vaissier, F J Beekman, and M C Goorden. Similarity-regulation of OS-EM for accelerated SPECT reconstruction. *Physics in medicine and biology*, 61(11):4300–15, 2016.
  - [54] Frans van der Have, Brendan Vastenhouw, Mart Rentmeester, and F.J. Beekman. System Calibration and Statistical Image Reconstruction for Ultra-High Resolution Stationary Pinhole SPECT. *IEEE Transactions on Medical Imaging*, 27(7):960–971, jul 2008.
  - [55] Freek Beekman and Frans Van Der Have. The pinhole: Gateway to ultra-high-resolution three-dimensional radionuclide imaging. *European Journal of Nuclear Medicine and Molecular Imaging*, 34(2):151–161, 2007.
  - [56] D E Copeland and E W Benjamin. Pinhole camera for gamma-ray sources. *Nucleonics*, 5(2):44–9, aug 1949.

- [57] Hal O. Anger. Scintillation Camera. *Review of Scientific Instruments*, 29(1):27–33, jan 1958.
- [58] J R Mallard and M J Myers. The performance of a gamma camera for the visualization of radioactive isotope in vivo. *Physics in medicine and biology*, 8:165–82, jun 1963.
- [59] Hyunki Kim, Lars R. Furenlid, Michael J. Crawford, Donald W. Wilson, H. Bradford Barber, Todd E. Peterson, William C.J. Hunter, Zhonglin Liu, James M. Woolfenden, and Harrison H. Barrett. SemiSPECT: A small-animal single-photon emission computed tomography (SPECT) imager based on eight cadmium zinc telluride (CZT) detector arrays. *Medical Physics*, 2006.
- [60] T.F. Peterson, Hyunki Kim, M.J. Crawford, B.M. Gershman, W.C.J. Hunter, H.B. Barber, L.R. Furenlid, D.W. Wilson, J.M. Woolfenden, and H.H. Barrett. SemiSPECT: a small-animal imaging system based on eight CdZnTe pixel detectors. In *2002 IEEE Nuclear Science Symposium Conference Record*, volume 3, pages 1844–1847. IEEE, 2002.
- [61] Kenta Miwa, Masayuki Inubushi, Yasuto Takeuchi, Tetsuro Katafuchi, Mitsuru Koizumi, Tsuneo Saga, and Masayuki Sasaki. Performance characteristics of a novel clustered multi-pinhole technology for simultaneous high-resolution SPECT/PET. *Annals of Nuclear Medicine*, 29(5):460–466, 2015.
- [62] Moshe Bocher, Ira M Blevis, Leonid Tsukerman, Yigal Shrem, Gil Kovalski, and Lana Volokh. A fast cardiac gamma camera with dynamic SPECT capabilities: design, system validation and future potential. *European journal of nuclear medicine and molecular imaging*, 37(10):1887–902, oct 2010.
- [63] Jason D Bowen, Qiu Huang, Justin R Ellin, Tzu-Cheng Lee, Uttam Shrestha, Grant T Gullberg, and Youngho Seo. Design and performance evaluation of a 20-aperture multipinhole collimator for myocardial perfusion imaging applications. *Physics in Medicine and Biology*, 58(20):7209–7226, oct 2013.
- [64] Tzu-Cheng Lee, Justin R. Ellin, Qiu Huang, Uttam Shrestha, Grant T. Gullberg, and Youngho Seo. Multipinhole collimator with 20 apertures for a brain SPECT application. *Medical Physics*, 41(11):112501, oct 2014.
- [65] Freek J Beekman, Frans van der Have, M C Goorden, P E B Vaissier, Jarno van Roosmalen, and H Doring. G-SPECT-I: a full ring high sensitivity and ultra-fast clinical molecular imaging system with <3mm resolution. In *Eur J Nucl Med Mol Imaging*, page 42 Suppl 1:S209, 2015.
- [66] Michael A. King, Joyeeta M Mukherjee, Arda Konik, I. George Zubal, Joyoni Dey, and Robert Licho. Design of a Multi-Pinhole Collimator for I-123 DaTscan Imaging on Dual-Headed SPECT Systems in Combination with a Fan-Beam Collimator. *IEEE Transactions on Nuclear Science*, 63(1):90–97, feb 2016.
- [67] Jarno van Roosmalen, Marlies C Goorden, and Freek J Beekman. Molecular breast tomosynthesis with scanning focus multi-pinhole cameras. *Physics in Medicine & Biology*, 5508:5508, 2016.

- 
- [68] Forrest McDougal and Martin Tornai. *Molecular breast imaging using a fully tomographic stationary clinical cardiac SPECT scanner: a phantom study*, volume 58. Society of Nuclear Medicine, may 2017.
  - [69] Ling Chen, Benjamin M.W. Tsui, and Greta S.P. Mok. Design and evaluation of two multi-pinhole collimators for brain SPECT. *Annals of Nuclear Medicine*, 31(8):1–13, 2017.
  - [70] R J Jaszczak. Uranium Pinhole Collimators for I-131 SPECT Imaging. 46(4):1165–1171, 1999.
  - [71] C.R. Tenney, M.P. Tornai, M.F. Smith, T.G. Turkington, and R.J. Jaszczak. Uranium pinhole collimators for 511-keV photon SPECT imaging of small volumes. *IEEE Transactions on Nuclear Science*, 48(4):1483–1489, 2001.
  - [72] Martin P Tornai, James E Bowsher, Ronald J Jaszczak, Brett C Pieper, Kim L Greer, Patricia H Hardenbergh, and R Edward Coleman. Mammotomography with pinhole incomplete circular orbit SPECT. *Journal of nuclear medicine : official publication, Society of Nuclear Medicine*, 44(4):583–93, apr 2003.
  - [73] J Mejia, O Y Galvis-Alonso, A A de Castro, J Braga, J P Leite, and M V Simões. A clinical gamma camera-based pinhole collimated system for high resolution small animal SPECT imaging. *Brazilian journal of medical and biological research = Revista brasileira de pesquisas medicas e biologicas*, 43(12):1160–6, dec 2010.
  - [74] Frans van der Have and Freek J Beekman. Photon penetration and scatter in micro-pinhole imaging: a Monte Carlo investigation. *Physics in Medicine and Biology*, 49(8):1369–1386, apr 2004.
  - [75] Victor Bom, Marlies Goorden, and Freek Beekman. Comparison of pinhole collimator materials based on sensitivity equivalence. *Physics in medicine and biology*, 56(11):3199–214, 2011.
  - [76] S Jan, D Benoit, E Becheva, Hsin-hon Lin, Keh-shih Chuang, Carlo Pet, Richard Brown, S Jan, G Santin, D Strul, S Staelens, and K Assi. GATE : a simulation toolkit for PET and SPECT. 2004.
  - [77] S. Jan, D. Benoit, E. Becheva, T. Carlier, F. Cassol, P. Descourt, T. Frisson, L. Grevillot, L. Guigues, L. Maigne, C. Morel, Y. Perrot, N. Rehfeld, D. Sarrut, D. R. Schaart, S. Stute, U. Pietrzyk, D. Visvikis, N. Zahra, and I. Buvat. GATE V6: A major enhancement of the GATE simulation platform enabling modelling of CT and radiotherapy. *Physics in Medicine and Biology*, 56(4):881–901, 2011.
  - [78] Steven Staelens, Kathleen Vunckx, Jan De Beenhouwer, Freek Beekman, Yves D Asseler, Johan Nuyts, and Ignace Lemahieu. GATE simulations for optimization of pinhole imaging. 569:359–363, 2006.
  - [79] Chia Lin Chen, Yuchuan Wang, Jason J.S. Lee, and Benjamin M.W. Tsui. Integration of SimSET photon history generator in GATE for efficient Monte Carlo simulations of pinhole SPECT. *Medical Physics*, 35(7):3278–3284, 2008.

- [80] S Y F Chu, L P Ekstrom, and R B Firestone. Table of Radioactive Isotopes, 1998.
- [81] M. Moszyński, J. Zalipska, M. Balcerzyk, M. Kapusta, W. Mengesha, and J.D. Valentine. Intrinsic energy resolution of NaI(Tl). *Nuclear Instruments and Methods in Physics Research Section A: Accelerators, Spectrometers, Detectors and Associated Equipment*, 484(1-3):259–269, may 2002.
- [82] Hamamatsu. *Photomultiplier tubes: Basics and Applications (Edition 3a)*. 2007.
- [83] Saint-Gobain. NaI(Tl) and Polyscin® NaI(Tl) Sodium Iodide Scintillation Material.
- [84] Xing Rong, Yong Du, Michael Ljungberg, Erwann Rault, Stefaan Vandenberghe, and Eric C. Frey. Development and evaluation of an improved quantitative 90Y bremsstrahlung SPECT method. *Medical Physics*, 39(May):2346, 2012.
- [85] Roberto Accorsi and Scott D. Metzler. Analytic determination of the resolution-equivalent effective diameter of a pinhole collimator. *IEEE Transactions on Medical Imaging*, 23(6):750–763, 2004.
- [86] J H. Hubbell and Stephen M. Seltzer. Tables of X-Ray Mass Attenuation Coefficients and Mass Energy-Absorption Coefficients. 1995.
- [87] Stephen M. Seltzer. Calculation of Photon Mass Energy-Transfer and Mass Energy-Absorption Coefficients. *Radiation Research*, 136(2):147, nov 1993.
- [88] Kenneth Levenberg. A method for the solution of certain non-linear problems in least squares. *Quarterly of Applied Mathematics*, 2(2):164–168, jul 1944.
- [89] Donald W. Marquardt. An Algorithm for Least-Squares Estimation of Nonlinear Parameters. *Journal of the Society for Industrial and Applied Mathematics*, 11(2):431–441, jun 1963.
- [90] C. Maple. Geometric design and space planning using the marching squares and marching cube algorithms. In *International Conference on Geometric Modeling and Graphics, 2003. Proceedings*, pages 90–95. IEEE Comput. Soc, 2003.
- [91] Nicole M. Hijnen, Anke de Vries, Roy Blange, Dirk Burdinski, and Holger Gröll. Synthesis and in vivo evaluation of 201Tl(III)–DOTA complexes for applications in SPECT imaging. *Nuclear Medicine and Biology*, 38(4):585–592, may 2011.
- [92] Stefanie M. A. Willekens, Lieke Joosten, Otto C. Boerman, Alexander Balhuizen, Decio L. Eizirik, Martin Gotthardt, and Maarten Brom. Strain Differences Determine the Suitability of Animal Models for Noninvasive In Vivo Beta Cell Mass Determination with Radiolabeled Exendin. *Molecular Imaging and Biology*, 18(5):705–714, oct 2016.
- [93] Minh Phuong Nguyen, Wouter Ensing, Brendan Vastenhouw, Chris Kamphuis, Ruud Ramakers, Marlies C Goorden, and Freek J Beekman. System Modeling and Image Reconstruction for 3D Micron-resolution Autoradiography. *NSS-MIC*, 2017.

- 
- [94] Koichi Ogawa, Yasuo Harata, Takashi Ichihara, Atsushi Kubo, and Shozo Hashimoto. A Practical Method for Position-Dependent Compton-Scatter Correction in Single Photon Emission CT. *IEEE Transactions on Medical Imaging*, 10(3):408–412, 1991.
  - [95] T. C. Appleton. Autoradiography of soluble labelled compounds. *Journal of the Royal Microscopical Society*, 83(3):277–281, sep 1964.
  - [96] S Ullberg. The technique of whole body autoradiography : cryosectioning of large specimens. *Science Tools*, pages 2–29, 1977.
  - [97] Weizhao Zhao, T.Y. Young, and M.D. Ginsberg. Registration and three-dimensional reconstruction of autoradiographic images by the disparity analysis method. *IEEE Transactions on Medical Imaging*, 12(4):782–791, 1993.
  - [98] Boklye Kim, Jennifer L. Boes, Kirk A. Frey, and Charles R. Meyer. Mutual information for automated unwarping of rat brain autoradiographs. *NeuroImage*, 5(1):31–40, 1997.
  - [99] Anand Rangarajan, Haili Chui, Eric Mjolsness, Suguna Pappu, Lila Davachi, Patricia Goldman-Rakic, and James Duncan. A robust point-matching algorithm for autoradiograph alignment. *Medical Image Analysis*, 1(4):379–398, 1997.
  - [100] N Barthe, K Chatti, P Coulon, S Ma1. trejean, and B Basse-Cathalinat. Recent technologic developments on high-resolution beta imaging systems for quantitative autoradiography and double labeling applications. *Nuclear Instruments and Methods in Physics Research Section A: Accelerators, Spectrometers, Detectors and Associated Equipment*, 527(1-2):41–45, jul 2004.
  - [101] A. Karellas, H. Liu, C. Reinhardt, L.J. Harris, and A.B. Brill. Imaging of radionuclide emissions with a low-noise charge-coupled device. *IEEE Transactions on Nuclear Science*, 40(4):979–982, aug 1993.
  - [102] P. Laniece, Y. Charon, A. Cardona, L. Pinot, S. Maitrejean, R. Mastrippolito, B. Sandkamp, and L. Valentin. A new high resolution radioimager for the quantitative analysis of radiolabelled molecules in tissue section. *Journal of Neuroscience Methods*, 86(1):1–5, dec 1998.
  - [103] Jorge Cabello, Alexis Bailey, and Ian Kitchen. The performance of a CCD digital autoradiography imaging system. *Physics in Medicine & Biology*, 45:2011, 2000.
  - [104] E. Kokkinou, K. Wells, M. Petrou, and A. Bailey. Digital autoradiography imaging using direct irradiation of a CCD between 278–309 K. In *2002 IEEE Nuclear Science Symposium Conference Record*, volume 3, pages 1607–1611. IEEE, 2003.
  - [105] Q. Peng, S. E. Holland, W. S. Choong, T. F. Budinger, and W. W. Moses. Real-time quantitative ex vivo direct autoradiography with 10 $\mu$ m pixel resolution. In *2011 Annual International Conference of the IEEE Engineering in Medicine and Biology Society*, pages 6273–6276. IEEE, aug 2011.

- [106] M.C. Montesi. BETAview autoradiography system: laboratory tests and biological experiments. *Nuclear Instruments and Methods in Physics Research Section A: Accelerators, Spectrometers, Detectors and Associated Equipment*, 461(1-3):425–427, apr 2001.
- [107] G. Mettivier, M.C. Montesi, and P. Russo. Digital autoradiography with a Medipix2 hybrid silicon pixel detector. *IEEE Transactions on Nuclear Science*, 52(1):46–50, feb 2005.
- [108] P Russo, A Lauria, G Mettivier, M C Montesi, M Marotta, L Aloj, and S Lastoria. 18 F-FDG positron autoradiography with a particle counting silicon pixel detector. *Physics in Medicine and Biology*, 53(21):6227–6243, nov 2008.
- [109] Jorge Cabello, M Esposito, G Mettivier, P R Russo -A CCDdigital autoradiography system J Ott, J MacDonald, K Wells, and Al . Digital autoradiography using room temperature CCD and CMOS imaging technology. *Phys. Med. Biol*, 52:4993, 2007.
- [110] Truong Nguyen Pham, Christian Finck, Patrice Marchand, David Brasse, Frederic Boisson, and Patrice Laquerriere. 18F autoradiography using pixelated CMOS technology. *Proceedings - 2017 IEEE 15th International New Circuits and Systems Conference, NEWCAS 2017*, pages 41–44, 2017.
- [111] J. Ulrici, P. Fischer, P. Klein, G. Lutz, W. Neeser, R. Richter, L. Strüder, M. Trimpl, and N. Wermes. Imaging performance of a DEPFET pixel Bioscope system in Tritium autoradiography. *Nuclear Instruments and Methods in Physics Research Section A: Accelerators, Spectrometers, Detectors and Associated Equipment*, 547(2-3):424–436, aug 2005.
- [112] E. Bertolucci, M. Conti, G. Grossi, G. Madonna, E. Mancini, P. Russo, M. Caria, P. Randaccio, A. del Guerra, M. Gambaccini, R. Marchesini, M. Marziani, A. Taibi, R. Beccherle, M.G. Bisogni, U. Bottigli, M.E. Fantacci, V. Rosso, A. Stefanini, R. Tripiccion, and S.R. Amendolia. Autoradiography with silicon strip detectors. *Nuclear Instruments and Methods in Physics Research Section A: Accelerators, Spectrometers, Detectors and Associated Equipment*, 381(2-3):527–530, nov 1996.
- [113] J. E. Lees, J. F. Pearson, G. W. Fraser, J. M. Hales, and P. G. Richards. An mcp-based system for beta autoradiography. *IEEE Transactions on Nuclear Science*, 46(3 PART 2):636–638, 1999.
- [114] J.E. Lees, A. Murray, A.C. Perkins, and G.W. Fraser. Autoradiography of high-energy radionuclides using a microchannel plate detector. *IEEE Transactions on Nuclear Science*, 49(1):153–155, feb 2002.
- [115] A A Dooraghi, N T Vu, R W Silverman, R Farrell, K S Shah, J Wang, J R Heath, and A F Chatziioannou. Betabox: a beta particle imaging system based on a position sensitive avalanche photodiode. *Physics in Medicine and Biology*, 58(11):3739–3753, jun 2013.

- 
- [116] Ling-Jian Meng, Jia Wei Tan, Geng Fu, Xiao Han, Erik Pearson, Xiao Chuan Pan, and Chin-Tu Chen. An ultra-high resolution SPECT/CT system for 3-D autoradiography. *Journal of Nuclear Medicine*, 48(supplement 2):459P, 2007.
  - [117] Ruud Ramakers, Brendan Vastenhouw, and Freek Beekman. *Ultra-high resolution cardiac SPECT of frozen animals as an alternative to autoradiography*, volume 50. Society of Nuclear Medicine, may 2009.
  - [118] Minh Phuong Nguyen, Marlies C. Goorden, Chris Kamphuis, and Freek J. Beekman. Evaluation of pinhole collimator materials for micron-resolution ex vivo SPECT. *Physics in Medicine and Biology*, 64(10), 2019.
  - [119] Woutjan Branderhorst, Brendan Vastenhouw, Frans Van Der Have, Erwin L A Blezer, Wim K. Bleeker, and Freek J. Beekman. Targeted multi-pinhole SPECT. *European Journal of Nuclear Medicine and Molecular Imaging*, 38(3):552–561, 2011.
  - [120] Piper M. Treuting and Suzanne M. Dintzis. *Comparative anatomy and histology : a mouse and human atlas*. Academic, 2012.
  - [121] Chao Wu, Frans Van Der Have, Brendan Vastenhouw, Rudi A J O Dierckx, Anne M J Paans, and Freek J. Beekman. Absolute quantitative total-body small-animal SPECT with focusing pinholes. *European Journal of Nuclear Medicine and Molecular Imaging*, 37(11):2127–2135, 2010.
  - [122] Brian F. Hutton, H. Malcolm Hudson, and Freek J. Beekman. A clinical perspective of accelerated statistical reconstruction, 1997.
  - [123] Jinyi Qi and Richard M Leahy. Iterative reconstruction techniques in emission computed tomography. *Physics in medicine and biology*, 51:R541–R578, 2006.
  - [124] B. Feng, M. Chen, B. Bai, A. M. Smith, D. W. Austin, R. A. Mintzer, D. Osborne, and J. Gregor. Modeling of the point spread function by numerical calculations in single-pinhole and multipinhole spect reconstruction. *IEEE Transactions on Nuclear Science*, 57(1 PART 1):173–180, 2010.
  - [125] Z El Bitar, F Pino, C Candela, D Ros, J Pavía, F R Rannou, A Ruibal, and P Aguiar. The performance of a hybrid analytical-Monte Carlo system response matrix in pinhole SPECT reconstruction. *Phys. Med. Biol*, 59, 2014.
  - [126] Pablo Aguiar, Francisco Pino, Jesús Silva-Rodríguez, Javier Pavía, Doménec Ros, Álvaro Ruibal, and Ziad El Bitar. Analytical, experimental, and Monte Carlo system response matrix for pinhole SPECT reconstruction. *Medical Physics*, 41(3):032501, mar 2014.
  - [127] Zhonglin Liu, George A. Kastis, Gail D. Stevenson, Harrison H. Barrett, Lars R. Furenlid, Matthew A. Kupinski, Dennis D. Patton, and Donald W. Wilson. Quantitative Analysis of Acute Myocardial Infarct in Rat Hearts with Ischemia-Reperfusion Using a High-Resolution Stationary SPECT System. *Journal of Nuclear Medicine*, 43(7), 2002.

- [128] B. W. Miller, R. Van Holen, H. H. Barrett, and L. R. Furenlid. A System Calibration and Fast Iterative Reconstruction Method for Next-Generation SPECT Imagers. *IEEE Transactions on Nuclear Science*, 59(5):1990–1996, oct 2012.
- [129] Minh Phuong Nguyen, Ruud M. Ramakers, Chris Kamphuis, Sofia Koustoulidou, Marlies C. Goorden, and Freek J. Beekman. EXIRAD-3D: Fast automated three-dimensional autoradiography. *Nuclear Medicine and Biology*, 86-87:59–65, jul 2020.
- [130] Benjamin Auer, Navid Zeraatkar, Soumyanil Banerjee, Justin C. Goding, Lars R. Furenlid, and Michael A. King. Preliminary investigation of a Monte Carlo-based system matrix approach for quantitative clinical brain 123I SPECT imaging. In *2018 IEEE Nuclear Science Symposium and Medical Imaging Conference, NSS/MIC 2018 - Proceedings*, page 8824750. Institute of Electrical and Electronics Engineers Inc., nov 2018.
- [131] Z El Bitar, Virgile Bekaert, and David Brasse. Acceleration of fully 3D Monte Carlo based system matrix computation for image reconstruction in small animal SPECT. *IEEE Transactions on Nuclear Science*, 58(1 PART 1):121–132, feb 2011.
- [132] Se Young Chun, Minh Phuong Nguyen, Thanh Quoc Phan, Hanvit Kim, Jeffrey A. Fessler, and Yuni K. Dewaraja. Algorithms and Analyses for Joint Spectral Image Reconstruction in Y-90 Bremsstrahlung SPECT. *IEEE Transactions on Medical Imaging*, 39(5):1369–1379, 2020.
- [133] Yuni K. Dewaraja, Se Young Chun, Ravi N. Srinivasa, Ravi K. Kaza, Kyle C. Cuneo, Bill S. Majdalany, Paula M. Novelli, Michael Ljungberg, and Jeffrey A. Fessler. Improved quantitative 90Y bremsstrahlung SPECT/CT reconstruction with Monte Carlo scatter modeling:. *Medical Physics*, 44(12):6364–6376, dec 2017.
- [134] Mark Gieles, Hugo W a M de Jong, and Freek J Beekman. Monte Carlo simulations of pinhole imaging accelerated by kernel-based forced detection. *Physics in medicine and biology*, 47(11):1853–1867, 2002.
- [135] Jan De Beenhouwer and Steven Staelens. Fast GATE multi-pinhole SPECT simulations. In *IEEE Nuclear Science Symposium Conference Record*, pages 3634–3637, 2010.
- [136] A. Van Oosterom and J. Strackee. The Solid Angle of a Plane Triangle. *IEEE Transactions on Biomedical Engineering*, BME-30(2):125–126, 1983.
- [137] James E. Seabold. Procedure Guideline for Gallium Scintigraphy in Inflammation, 1997.
- [138] Shaunak Navalkisoor, AnnMarie Quigley, JohnR Buscombe, and Ewa Nowosinska. Is there a Role for Gallium-67 Citrate SPECT/CT, in Patients with Renal Impairment or Who are Renal Transplant Recipients, in Identifying and Localizing Suspected Infection? *World Journal of Nuclear Medicine*, 14(3):184, 2015.

- 
- [139] E. F. H. van Bommel, C. Siemes, S. J. van der Veer, S. H. Han, A. W. L. C. Huiskes, and T. R. Hendriks. Clinical value of gallium-67 SPECT scintigraphy in the diagnostic and therapeutic evaluation of retroperitoneal fibrosis: a prospective study. *Journal of Internal Medicine*, 262(2):224–234, aug 2007.
  - [140] Lale Kostakoglu, John P. Leonard, Ichiei Kuji, Morton Coleman, Shankar Vallabhajosula, and Stanley J. Goldsmith. Comparison of fluorine-18 fluorodeoxyglucose positron emission tomography and Ga-67 scintigraphy in evaluation of lymphoma. *Cancer*, 94(4):879–888, feb 2002.
  - [141] Junichi Taki. Cardiac Sarcoidosis Demonstrated by Tl-201 and Ga-67 SPECT Imaging, 1990.
  - [142] Shirou Ishii, Fumio Shishido, Masayuki Miyajima, Koutarou Sakuma, Takeshi Shighihara, and Ken Kikuchi. Whole-Body Gallium-67 Scintigraphic Findings in IgG4-Related Disease. *Clinical Nuclear Medicine*, 36(7):542–545, jul 2011.
  - [143] Szlávecz, G. Hesz, and B. Benyó. The use of multi-energy photon emitters in 3D SPECT reconstruction. *Biomedical Signal Processing and Control*, 47:413–423, jan 2019.
  - [144] Maryam Shirmohammad. Ga-67 Imaging with VECTor. Technical report, 2016.
  - [145] S.C. Moore, G. El Fakhri, M.-A. Park, and M.F. Kijewski. Quantitative Ga-67 SPECT imaging. In *2003 IEEE Nuclear Science Symposium. Conference Record (IEEE Cat. No.03CH37515)*, volume 4, pages 2898–2900. IEEE, 2003.
  - [146] Renaud Lhommel, Larry Van Elmbt, Pierre Goffette, Marc Van Den Eynde, François Jamar, Stanislas Pauwels, and Stephan Walrand. Feasibility of 90Y TOF PET-based dosimetry in liver metastasis therapy using SIR-Spheres. *European Journal of Nuclear Medicine and Molecular Imaging*, 2010.
  - [147] Andrew Kennedy. Radioembolization of hepatic tumors, 2014.
  - [148] W. Siman, J. K. Mikell, and S. C. Kappadath. Practical reconstruction protocol for quantitative 90Y bremsstrahlung SPECT/CT. *Medical Physics*, 43(9):5093–5103, sep 2016.
  - [149] Mattijs Elschot, Marnix G. E. H. Lam, Maurice A. A. J. van den Bosch, Max A. Viergever, and Hugo W. A. M. de Jong. Quantitative Monte Carlo-based 90Y SPECT reconstruction. *Journal of nuclear medicine : official publication, Society of Nuclear Medicine*, 54(9):1557–63, 2013.
  - [150] C. Wu, J. R. De Jong, H. A. Gratama Van Andel, F. Van Der Have, B. Vastenhouw, P. Laverman, O. C. Boerman, R. A.J.O. Dierckx, and F. J. Beekman. Quantitative multi-pinhole small-animal SPECT: Uniform versus non-uniform Chang attenuation correction. *Physics in Medicine and Biology*, 56(18):183–193, sep 2011.

- [151] Minh Phuong Nguyen, Marlies C Goorden, and Freek J Beekman. EXIRAD-HE: multi-pinhole high-resolution ex vivo imaging of high-energy isotopes. *Physics in Medicine & Biology*, 65(22):225029, sep 2020.
- [152] Douglas J. Rowland and Simon R. Cherry. Small-Animal Preclinical Nuclear Medicine Instrumentation and Methodology, may 2008.
- [153] Ken Herrmann, Magnus Dahlbom, David Nathanson, Liu Wei, Caius Radu, Arion Chatzioannou, and Johannes Czernin. Evaluation of the genesis4, a bench-top preclinical PET Scanner. *Journal of Nuclear Medicine*, 54(7):1162–1167, jul 2013.
- [154] Antonio J. Gonzalez, Albert Aguilar, Pablo Conde, Liczandro Hernandez, Filomeno Sanchez, Laura Moliner, Luis F. Vidal, Julio Barbera, Carlos Correcher, Cesar Molinos, Constantino Morera, Konrad Lankes, Sven Junge, Thomas Bruckbauer, and Jose M. Benlloch. Next generation of the Albira small animal PET based on high density SiPM arrays. In *2015 IEEE Nuclear Science Symposium and Medical Imaging Conference, NSS/MIC 2015*. Institute of Electrical and Electronics Engineers Inc., oct 2016.
- [155] K. Sato, M. Shidahara, H. Watabe, S. Watanuki, Y. Ishikawa, Y. Arakawa, Yh Nai, S. Furumoto, M. Tashiro, T. Shoji, K. Yanai, and K. Gonda. Performance evaluation of the small-animal PET scanner ClairvivoPET using NEMA NU 4-2008 Standards. *Physics in Medicine and Biology*, 61(2):696–711, dec 2016.
- [156] Srilalan Krishnamoorthy, Eric Blankemeyer, Pieter Mollet, Suleman Surti, Roel Van Holen, and Joel S. Karp. Performance evaluation of the MOLECUBES  $\beta$ -CUBE - A high spatial resolution and high sensitivity small animal PET scanner utilizing monolithic LYSO scintillation detectors. *Physics in Medicine and Biology*, 63(15), 2018.
- [157] Yongfeng Yang, Julien Bec, Jian Zhou, Mengxi Zhang, Martin S Judenhofer, Xiaowei Bai, Kun Di, Yibao Wu, Mercedes Rodriguez, Purushottam Dokhale, Kanai S Shah, Richard Farrell, Jinyi Qi, and Simon R Cherry. A high resolution prototype small-animal PET scanner dedicated to mouse brain imaging. *J Nucl Med*, 57(7):1130–1135, 2016.
- [158] M C M Rentmeester, F van der Have, and F J Beekman. Optimizing multi-pinhole SPECT geometries using an analytical model. *Physics in medicine and biology*, 52(9):2567–81, 2007.
- [159] Iina Laitinen, Päivi Marjamäki, Merja Haaparanta, Nina Savisto, V. Jukka O. Laine, Sanna L. Soini, Ian Wilson, Pia Leppänen, Seppo Ylä-Herttua, Anne Roivainen, and Juhani Knuuti. Non-specific binding of [18F]FDG to calcifications in atherosclerotic plaques: Experimental study of mouse and human arteries. *European Journal of Nuclear Medicine and Molecular Imaging*, 33(12):1461–1467, 2006.
- [160] Chang-Lae Lee, Hilla Wahnische, George A Sayre, Hyo-Min Cho, Hee-Joung Kim, Miguel Hernandez-Pampaloni, Randall A Hawkins, Shorouk F Dannoon, Henry F Vanbrocklin, Melissa Itsara, William A Weiss, Xiaodong Yang, Daphne A Haas-Kogan, Katherine K Matthay, and Youngho Seo. Radiation dose estimation using preclinical imaging with 124 I-metaiodobenzylguanidine (MIBG) PET. 2010.

- 
- [161] R Senekowitsch-Schmidtke, C Schuhmacher, K F Becker, T K Nikula, C Seidl, I Becker, M Miederer, C Apostolidis, C Adam, R Huber, E Kremmer, K Fischer, and M Schwaiger. Highly specific tumor binding of a  $^{213}\text{Bi}$ -labeled monoclonal antibody against mutant E-cadherin suggests its usefulness for locoregional alpha-radioimmunotherapy of diffuse-type gastric cancer. *Cancer research*, 61(7):2804–8, apr 2001.
- [162] Shiho Nomura, Satoshi Nozaki, Takashi Hamazaki, Taisuke Takeda, Eiichi Ninomiya, Satoshi Kudo, Emi Hayashinaka, Yasuhiro Wada, Tomoko Hiroki, Chie Fujisawa, Hiroko Kodama, Haruo Shintaku, and Yasuyoshi Watanabe. PET imaging analysis with  $^{64}\text{Cu}$  in disulfiram treatment for aberrant copper biodistribution in menkes disease mouse model. *Journal of Nuclear Medicine*, 55(5):845–851, may 2014.
- [163] Bernard M. Tjink, Lars R. Perk, Marianne Budde, Marijke Stigter-Van Walsum, Gerard W.M. Visser, Reina W. Kloet, Ludger M. Dinkelborg, C. René Leemans, Dario Neri, and Guus A.M.S. Van Dongen.  $^{124}\text{I}$ -L19-SIP for immuno-PET imaging of tumour vasculature and guidance of  $^{131}\text{I}$ -L19-SIP radioimmunotherapy. *European Journal of Nuclear Medicine and Molecular Imaging*, 36(8):1235–1244, 2009.
- [164] J. Valla, K. Chen, J. D. Berndt, F. Gonzalez-Lima, S. R. Cherry, D. Games, and E. M. Reiman. Effects of image resolution on autoradiographic measurements of posterior cingulate activity in PDAPP mice: Implications for functional brain imaging studies of transgenic mouse models of Alzheimer’s disease. *NeuroImage*, 2002.
- [165] Craig S Levin and Edward J Hoffman. Calculation of positron range and its effect on the fundamental limit of positron emission tomography system spatial resolution. Technical report, 1999.
- [166] J. Cal-González, J. L. Herraiz, S. España, P M G Corzo, J. J. Vaquero, M. Desco, and J. M. Udias. Positron range estimations with PeneloPET. *Physics in Medicine and Biology*, 58(15):5127–5152, aug 2013.



# Acknowledgments

This journey would not have been possible without the help of many people who, throughout the years, in one way or another, contributed to the completion of this thesis.

First of all, I would like to thank my promotor Prof.dr. Freek Beekman for his guidance and support during my PhD studies. His knowledge and high enthusiasm in the field helps to push limits and move the field forward. I appreciate his balance in providing supervision and giving me independence in research. He both suggested research directions and welcomed my new ideas. He provided deep scientific insight and practical perspectives to my researches. He also gave me access to the imaging systems at MILabs B.V. and supported collaborations which are vital for the studies in this thesis.

I would like to express my gratitude to my co-promotor Dr.ir. Marlies Goorden. She acted as my daily supervisor with whom I had regular meetings to discuss every aspect of my work. Her suggestions and critical questions help me a lot to move forward. When it comes to scientific publications, she gave detailed feedback and made corrections in my manuscripts. I usually read most of the tracked changes she made, and in this way, I have improved my scientific writing skill over the years.

I would like to extend my sincere thanks to other members of my PhD defence committee for their interest and time invested in my thesis: Prof.dr.ir. Harrie Weinans (TU Delft/ UMC Utrecht), Prof.dr. Vesna Sossi (The University of British Columbia), Prof.dr. Scott Metzler (University of Pennsylvania), Prof.dr. Erik Verburg (Erasmus MC), Dr. Julie Nonnekens (Erasmus MC), and Prof.dr. Pieter Dorenbos (TU Delft). It is my honour to have them on the committee.

I feel thankful to have worked with my colleagues in the section Biomedical Imaging at TU Delft. Beien and Jarno offered me a warm welcome on the first day I arrived in Delft by picking up my wife and me at the train station and guiding us to our rental apartment. In the days afterwards, they familiarised me with the topics in our group and introduced to me some of the important tools that I later used in my researches. After Jarno left, Beien was the most senior PhD candidate and then a postdoc researcher from whom I learned a lot. He also participated in organising useful and fun events for the PhD student community within my department. Yuan shared with me a great deal of experience in research and the publication process. It is good that we can prepare the steps for our defence at the same time and have defence dates close to each other. With Beien and Yuan, we shared the same office room and often talked on a broad range of topics, not limited to our works. We went to conferences together and enjoyed Chinese and Vietnamese food. With them, I always felt accompanied during my PhD. Monika helped to verify many parts of the computation workflow that I created. Rob helped whenever I had computer- or data-related issues and he revised the Dutch summary of this thesis as well. Jan suggested group activities such as getting more residents for the mini aquarium at our workplace or going for trail walks. We could have done much more if working from home had not become the norm. Arif and Valerio recently joined the group. I wish them success in their research projects. Special thanks to Trudy for tremendous organisational support from the first day until the last day

that I am in the group, which made my life as a PhD student much easier.

It also was a great pleasure to work with the group in MILabs B.V. in a fruitful collaboration. I would like to thank Wouter for helping me a lot at the beginning of my PhD study to learn about part of the software needed for my researches. He provided detailed documentation and answered all of my questions about the large number of terms and parameters used in the software so that I could quickly learn and apply them. Chris is the one I could turn to for many research-related questions and discussions. With his keen scientific eye, he often gave insightful comments and suggestions for my researches and publications. I also thank Ruud and Sophia for revising experimental protocols, preparing and performing experiments and providing part of the data that supports this thesis. I would like to thank David for an initial effort in visualising my experimental data, and Yutaro for providing the computer-aided designs of parts of the scanners and assisting me on many mechanical aspects. Also, many thanks to Brendan, Chao, and other persons in MILabs who created or contributed to the software as well as the realisation of the collimators used in this thesis.

Thanks to other people at the Reactor Institute Delft where our group is located, including Evert, Maarten, Giacomo, Weronika, Roy, Tianshuai, Hongde, and anyone I might have forgotten. We always had a great time in the midst of or after the work when together for coffee breaks, board games, potlucks, pub quizzes, dinners, movie nights, travels, and other events in the PhD community. Those will remain memorable to me.

I would like to thank my friends and all the amazing people I have in my life outside the office. Especially, I am really thankful to be a part of the Vietnamese Community in Delft (VCiD) - a strong community where all members support each other and spend time together whenever possible, which makes me and my family always feel at home. I am also grateful to many people I have met in the International Neighbour Group Delft, Dutch classes, badminton training and tournaments, swimming lessons, volleyball games, et cetera. Unfortunately, in recent time, we cannot often meet each other for these activities because of the COVID-19, but we will soon return to normalcy.

Last but not least, I would like to express my gratitude to all of my family members, who are always standing by me. I feel grateful for constant supports from our parents, brothers and sisters. I really appreciate our parents travelling to the Netherlands several times to help us since our son was born. I am sorry I cannot invite my father and father-in-law to the Netherlands this time to join my defence ceremony as I promised because of the travel limitations, but I am fortunate that they can also connect online. Special thanks to my wife Hana and my son Leo for their love and encouragement at all times. Hana, thanks for being with me since we were in high school and going together through many of our important milestones. Leo, thank you for coming and bringing a lot of joy into our lives. I am thankful to have both of you here with me to enjoy this moment. I am happy to see your smile every day - my source of strength to overcome all challenges.

*Minh Phuong Nguyen  
Delft, May 2021*

# Curriculum Vitae

## **Minh Phuong NGUYEN**

Born on 24 January, 1991 in Hai Phong, Vietnam

2020/10 - Present	MILabs B.V., the Netherlands Computational Scientist
2016/10 - Present	Delft University of Technology, the Netherlands PhD candidate in Section Biomedical Imaging
2014/09 - 2016/08	Ulsan National Institute of Science and Technology, South Korea Master of Science in Electrical Engineering, Worked in Biomedical Image Processing Lab.
2012/10 - 2013/04	Faculdade de Engenharia da Universidade do Porto, Portugal Erasmus Mundus Exchange Programme, Integrated Master in Bioengineering
2018/09 - 2013/08	Hanoi University of Science and Technology, Vietnam Bachelor's degree in Biomedical Engineering



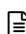
# List of Publications

## Peer-Reviewed Journal Article:

9. **Minh Phuong Nguyen**, Marlies C. Goorden, Ruud M. Ramakers, and Freek J. Beekman. Efficient Monte-Carlo based system modelling for image reconstruction in preclinical pinhole SPECT. *Physics in Medicine & Biology* (accepted).
8. **Minh Phuong Nguyen**, Marlies C. Goorden, and Freek J. Beekman. EXIRAD-HE: multi-pinhole high-resolution *ex vivo* imaging of high-energy isotopes. *Physics in Medicine & Biology* 65.22: 225029, 2020.
7. **Minh Phuong Nguyen**, Ruud M. Ramakers, Chris Kamphuis, Sofia Koustoulidou, Marlies C. Goorden, and Freek J. Beekman. EXIRAD-3D: Fast automated three-dimensional autoradiography. *Nuclear Medicine and Biology* 86: 59-65, 2020.
6. **Minh Phuong Nguyen**, Marlies C. Goorden, Chris Kamphuis, and Freek J. Beekman. Evaluation of pinhole collimator materials for micron-resolution *ex vivo* SPECT. *Physics in Medicine & Biology* 64.10: 105017, 2019.
5. Se Young Chun, **Minh Phuong Nguyen**, Thanh Quoc Phan, Hanvit Kim, Jeffrey A. Fessler, and Yuni K. Dewaraja. Algorithms and analyses for joint spectral image reconstruction in Y-90 bremsstrahlung SPECT. *IEEE Transactions on Medical Imaging* 39.5: 1369-1379, 2019.
4. **Minh Phuong Nguyen**, and Se Young Chun. Bounded self-weights estimation method for non-local means image denoising using minimax estimators. *IEEE Transactions on Image Processing* 26.4: 1637-1649, 2017.
3. Jae-Hyeok Lee, Sun-Yong Baek, YoungKyu Song, Sujeong Lim, Hansol Lee, **Minh Phuong Nguyen**, Eun-Joo Kim, Gi Yeong Huh, Se Young Chun, and HyungJoon Cho. The Neuromelanin-related  $T_2^*$  contrast in postmortem human substantia nigra with 7T MRI. *Scientific Reports* 6.1: 1-9, 2016.
2. Quang Doan Truong, **Minh Phuong Nguyen**, V. T. Hoang, H. T. Nguyen, D. T. Nguyen, Tien Dzung Nguyen, Viet Dung Nguyen. Feature extraction and Support Vector Machine based classification for false positive reduction in mammographic images. *Frontier and Future Development of Information Technology in Medicine and Education*, Springer, Dordrecht: 921-929, 2014.
1. **Minh Phuong Nguyen**, Quang Doan Truong, D. T. Nguyen, Tien Dzung Nguyen, and Viet Dung Nguyen. An alternative approach to reduce massive false positives in mammograms using block variance of local coefficients features and support vector machine. *Procedia computer science* 20: 399-405, 2013.

## Conference Abstract & Proceeding:

7. **Minh Phuong Nguyen**, Marlies C. Goorden, Chris Kamphuis, and Freek J. Beekman. Optimized acquisition energy window in  $^{89}\text{Zr}$  imaging with multi-pinhole PET. *IEEE Nuclear Science Symposium and Medical Imaging Conference (NSS/MIC)*, 2020.
6. **Minh Phuong Nguyen**, Marlies C. Goorden, and Freek J. Beekman. Multi-pinhole collimator for ex-vivo imaging of high-Energy isotopes. *IEEE Nuclear Science Symposium and Medical Imaging Conference (NSS/MIC)*, 2019.
5. **Minh Phuong Nguyen**, Wouter Ensing, Brendan Vastenhouw, Chris Kamphuis, Ruud Ramakers, Marlies C. Goorden, and Freek J. Beekman. System modeling and image reconstruction for 3D micron-resolution autoradiography. *IEEE Nuclear Science Symposium and Medical Imaging Conference (NSS/MIC)*, 2017.
4. Hanvit Kim, **Minh Phuong Nguyen**, and Se Young Chun. Cancelable ECG biometrics using GLRT and performance improvement using guided filter with irreversible guide signal. *39th Annual International Conference of the IEEE Engineering in Medicine and Biology Society (EMBC)*, 2017.
3. **Minh Phuong Nguyen**, and Se Young Chun. Center pixel weight estimation for non-local means filtering using local James-Stein estimator with bounded self-weights. *IEEE 13th International Symposium on Biomedical Imaging (ISBI)*, 2016.
2. **Minh Phuong Nguyen**, Hanvit Kim, Se Young Chun, Jeffrey A. Fessler, and Yuni K. Dewaraja. Joint spectral image reconstruction for Y-90 SPECT with multi-window acquisition. *IEEE Nuclear Science Symposium and Medical Imaging Conference (NSS/MIC)*, 2015.
1. **Minh Phuong Nguyen**, and Viet Dung Nguyen. Design an Exoskeleton Model for Upper Arm Rehabilitation Controlled by Surface Electromyography. *ICAIT*, 2013.

 Included in this thesis.

ISBN: 978-94-6423-317-9